

5-2010

LAYER-BY-LAYER ASSEMBLY OF  
{NANOCLAY-(SOL-GEL OXIDE)}<sub>N</sub> AND  
{NANOCLAY-(OXIDE NANOPARTICLE)}<sub>N</sub>  
MULTILAYERS: SYNTHESIS AND GROWTH  
MECHANISMS

Hao Chen

Clemson University, hchen@clemson.edu

Follow this and additional works at: [https://tigerprints.clemson.edu/all\\_dissertations](https://tigerprints.clemson.edu/all_dissertations)

 Part of the [Materials Science and Engineering Commons](#)

---

#### Recommended Citation

Chen, Hao, "LAYER-BY-LAYER ASSEMBLY OF {NANOCLAY-(SOL-GEL OXIDE)}<sub>N</sub> AND {NANOCLAY-(OXIDE NANOPARTICLE)}<sub>N</sub> MULTILAYERS: SYNTHESIS AND GROWTH MECHANISMS" (2010). *All Dissertations*. 549.  
[https://tigerprints.clemson.edu/all\\_dissertations/549](https://tigerprints.clemson.edu/all_dissertations/549)

This Dissertation is brought to you for free and open access by the Dissertations at TigerPrints. It has been accepted for inclusion in All Dissertations by an authorized administrator of TigerPrints. For more information, please contact [kokeefe@clemson.edu](mailto:kokeefe@clemson.edu).

LAYER-BY-LAYER ASSEMBLY  
OF {NANOCLAY-(SOL-GEL OXIDE)}<sub>N</sub> AND {NANOCLAY-(OXIDE  
NANOPARTICLE)}<sub>N</sub> MULTILAYERS:  
SYNTHESIS AND GROWTH MECHANISMS

---

A Dissertation  
Presented to  
the Graduate School of  
Clemson University

---

In Partial Fulfillment  
of the Requirements for the Degree  
Doctor of Philosophy  
Materials Science and Engineering

---

by  
Hao Chen  
May 2010

---

Accepted by:  
Dr. Jian Luo, Committee Chair  
Dr. Konstantin Kornev  
Dr. Igor Luzinov  
Dr. Kathleen Richardson

## ABSTRACT

Two new classes of all-inorganic nanostructured multilayers,  $\{\text{MMT}_x\text{-(sol-gel oxide)}\}_n$  and  $\{\text{MMT}_x\text{-(oxide nanoparticle)}\}_n$ , have been successfully synthesized for the first time. They were made by adapting a layer-by-layer (LbL) assembly method initially developed to synthesize polyelectrolyte-based multilayers. In most previous studies, this electrostatic-assisted LbL assembly method used polyelectrolytes/polymers as the “structural glue” to prepare multilayers. The synthesis of  $\{\text{MMT}_x\text{-(sol-gel ZrO}_2)\}_n$  multilayers demonstrates for the first time the feasibility of making sol-gel oxide “glued” all-inorganic multilayers, thereby introducing an innovative nanoscale fabrication concept. The synthesis of  $\{\text{MMT}_x\text{-(oxide nanoparticle)}\}_n$  multilayers further illustrates the versatility of LbL assembly technique by achieving a second new type of all-inorganic multilayers with a novel “plate-ball” architecture. The feasibility of synthesizing other types of multilayer structures, including  $\{\text{MMT}_x\text{-(ionic liquid)}\}_n$ ,  $\{\text{(carbon nanotube)-(sol-gel ZrO}_2)\}_n$ , and  $\{\text{polymer-(sol-gel ZrO}_2)\}_n$ , were also explored.

Systematical investigations of the growth kinetics of  $\{\text{MMT}_x\text{-(sol-gel ZrO}_2)\}_n$  multilayers reveal unique underlying mechanisms for electrostatic-assisted growth of sol-gel films and LbL assembly. The growth of the MMT and sol-gel ZrO<sub>2</sub> layers is strongly coupled. For fresh aqueous ZrO<sub>2</sub> precursors, the growth rates of sol-gel ZrO<sub>2</sub> layers on MMT surfaces as functions of time and precursor concentration do not follow the standard mass transfer or interfacial reaction controlled kinetic models. Furthermore, the growth of the sol-gel oxide layers on MMT surfaces is self-limited to a maximum thickness of ~50-60 nm. These observations suggest a surface-mediated growth of sol-gel

`oxide layers on MMT surfaces, one that is likely controlled by electrostatic interactions. These new findings significantly advance the general understanding of the LbL electrostatic assembly process. For the aged precursors, the growth mechanism differs; the growth of sol-gel oxide layers is controlled by hydrodynamics and follows the Landau-Levich model. For as-deposited multilayers, isothermal annealing at  $\sim 400$  °C dehydrates them and removes the residue acetate groups without damaging the MMT nanoplatelets and the ordered layer structures. Nanomechanical measurements show that the elastic modulus of the multilayers can be intentionally tuned by changing the multilayer design and that significant porosity is present in the multilayers even after annealing. In addition, free-standing multilayers are successfully made via using sacrificial substrates, and the newly developed methodology for  $\{\text{MMT}_x\text{-(sol-gel oxide)}\}_n$  can be extended, using other metal oxides, e.g.,  $\text{SnO}_2$ , as the inorganic “glue.” Potential applications of these new nanostructured multilayers are discussed.

## ACKNOWLEDGMENTS

I would like to express my sincere gratitude to my research advisor, Dr. Jian Luo, for his support and guidance. He is so kind and patient, and always finds time to help me: a discussion of the research, an answer for scientific questions, and even suggestions for English writing. I wish I could contribute more as to take less his time and energy.

Thanks to my research committee, Dr. Konstantin G. Kornev, Dr. Igor Luzinov, and Dr. Kathleen Richardson, for their advices and helps.

Thanks to our group members, Jimmy Shi, Archana Kayyar, Meshinchi Asl Kaveh.

Special thanks to my fiancée, Jie Feng. She always says right things and cheers me up, making the hard time less difficult.

## TABLE OF CONTENTS

	Page
TITLE PAGE.....	i
ABSTRACT.....	ii
ACKNOWLEDGMENTS .....	iv
LIST OF TABLES.....	vii
LIST OF FIGURES .....	viii
CHAPTER	
I.    INTRODUCTION .....	1
II.   LITERATURE REVIEW .....	4
1. Layer-by-Layer Self Assembly.....	4
2. Clay Materials.....	10
3. Colloid Chemistry.....	16
4. Sol-Gel Chemistry .....	22
5. Dip Coating Processing.....	26
III.  SYNTHESIS OF OXIDE FILMS.....	28
1. Introduction.....	28
2. Experiments .....	30
3. Results and Discussions.....	32
IV.  A FEASIBILITY STUDY OF SYNTHESIS OF NANOCCLAY-ZIRCONIA MULTILAYERS .....	36
1. Introduction.....	36
2. Experimental .....	38
3. Results and Discussion .....	41
4. Conclusions.....	51
5. Issues and Further Studies .....	52

Table of Contents (Continued)

V.	GROWTH MECHANISMS OF NANOCCLAY-ZIRCONIA MULTILAYERS	54
	1. Introduction.....	54
	2. Experimental.....	56
	3. Results and Discussion.....	60
	4. Conclusions.....	87
VI.	SYNTHESIS OF NANOCCLAY-NANOPARTICLE MULTILAYERS	89
	1. Introduction.....	89
	2. Experimental.....	90
	3. Results and Discussions.....	92
VII.	AN EXPLORATORY STUDY OF SYNTHESIS OF OTHER TYPES MULTILAYERS	97
	1. MMT-SnO <sub>2</sub> Multilayers.....	97
	2. MMT-ZnO Multilayers.....	99
	3. MMT-CeO <sub>2</sub> Multilayers.....	102
	4. MMT-Ionic Liquid Multilayers.....	107
	5. Polymer-Oxide Multilayers and Carbon Nanotube-Zirconia Multilayers	109
VIII.	A DISCUSSION OF POTENTIAL APPLICATIONS.....	113
	1. High-Temperature Filtering Membranes.....	113
	2. Micro-Cantilevers.....	115
	3. Interface-Enhanced Fast Ionic Conductors.....	116
	4. Photonic Clays.....	118
	5. Protective Coatings.....	119
IX.	SUMMARY.....	121
	APPENDICES.....	125
	A: SYNTHESIS OF CERIA FILMS.....	126
	B: OPTIMIZATION EXPERIMENTS.....	129
	C: EFFECTS OF PH ON THE GROWTH OF NANOCCLAY-NANOPARTICLE MULTILAYERS.....	138
	REFERENCES.....	142

## LIST OF TABLES

Table	Page
Table 1. Classification of clay minerals.....	11
Table 2. Cation exchange capacity of clay minerals (meq/100g).....	14
Table 3. The swelling behavior of montmorillonite in water. ....	14
Table 4. Point of zero charge of several oxides. ....	17
Table 5. EDXS compositional analysis. Each data point is an average of three measurements. The measured excess amounts of Si and O are from Si/SiO <sub>2</sub> substrates (artifacts) due to spread of electron beams and do not represent actual film composition. ....	46
Table 6. The measured hardness and elastic modulus of clay-oxide multilayers prepared using 0.40 wt.% clay concentration. The nano mechanical tests were conducted in LSU by Z. Wei and G. Zhang using our specimens. ....	87
Table 7. Nanoclay exfoliation procedures from literatures.....	133



## LIST OF FIGURES

Figure	Page
Figure 1. Layer-by-layer self assembly of polyelectrolyte multilayers using poly (styrenesulfonate) (PSS) polyanions and poly (allylamine) (PAH) polycations. ....	4
Figure 2. (a) Polycations fold and pair with nanoclays <sup>9</sup> . (b) A molecular structure of the bonding between PVA and MMT <sup>10</sup> . (c) An enlarged six-membered ring formed between PVA and MMT. Al, purple; O, red; H, light gray; Si, dark gray; C, green. ....	10
Figure 3. The montmorillonite structure <sup>79</sup> .....	12
Figure 4. Water chemisorptions on an oxide surface <sup>83</sup> .....	16
Figure 5. (a) EDL models, Helmholtz, Gouy-Chapman, and Stern (from left to right), and the corresponding electrical potential ( $\phi$ ) plots for negatively charged surfaces <sup>85</sup> . (b) EDL of Stern model for a negatively charged metal surface, showing the inner Helmholtz (IHP), Stern layer, the outer Helmholtz (OHP), and the diffuse layers <sup>86</sup> .....	18
Figure 6. A schematic illustration of the origin of the electrostatic double-layer interactions <sup>86</sup> .....	20
Figure 7. A schematic of the potential energy vs. the particle distance, following the DLVO theory <sup>88</sup> .....	22
Figure 8. A typical “charge-pH” diagram <sup>90</sup> .....	24
Figure 9. Schematic illustration of sol-gel dip coating <sup>91</sup> .....	27
Figure 10. Schematics of a common SILAR dip coating procedure.....	29
Figure 11. The cross-sectional SEM images of zirconia films made using Method B (with one rinsing step) and following parameters: dipping speed = (a) 20 mm/min or (b) 10 mm/min, holding time = 10 sec, and number of deposition cycles = 10. As a comparison, a cross-sectional SEM image made using Method A (without rinsing steps; 20 mm/min dipping speed; 10 sec holding; 20 deposition cycles) is shown in (c). All specimens were annealed at 600 °C for 2 hours.....	32

List of Figures (Continued)

Figure 12. In-plane views of (a) our annealed and (b) as-deposited zirconia films made by Method B. .... 33

Figure 13. (a) Cross-sectional and (b) in-plane views of a representative as-deposited zirconia film made by a sol-gel dip coating method (Method C; 30 deposition cycles). (c) The thickness of as-deposited zirconia films vs. the number of deposition cycles. .... 34

Figure 14. A targeted multilayer structure to synthesize in this study using a new LBL assembling technique via making use of the intrinsic negative surface changes and unique party shape of nanoclays. In principle, the thickness and chemical composition of each nanometer-thick oxide layer can be tuned individually, offering versatility in engineering these nanostructured films with a wide range of potential applications to be explored in future studies. .... 37

Figure 15. Surface (a) and cross-sectional (b) images of as-deposited nanoclay-polymer [(PEI/PSS/PEI)-(nanoclay/PEI)<sub>8</sub>] films. .... 42

Figure 16. (a) Surface and (b) cross-sectional SEM images of as-deposited hydrated nanoclay-zirconia multilayers made via zirconium chloride cationic solution..... 43

Figure 17. (a) Surface and (b) cross-sectional SEM images of as-deposited hydrated nanoclay-zirconia multilayers made by zirconium acetate cationic solutions. .... 44

Figure 18. (a) and (b) cross-sectional and (c) surface SEM images of annealed nanoclay-zirconia films made by zirconium acetate precursor solutions (using 25 deposition cycles)..... 45

Figure 19. A representative EDXS spectrum for an annealed film..... 46

Figure 20. XRD patterns of (a) annealed and (b) as-deposited films (20 layers) made by zirconium acetate cationic solutions. The two XRD experiments are carried out with the same conditions (scan rate and slit size) and the patterns are shown in the same intensity scale. The insets are additional scans at low angles with a smaller slit (shown in different intensity scales). .... 49

List of Figures (Continued)

- Figure 21. Thickness versus number of deposition cycles for as-deposited (a) and annealed (b) films made by zirconium acetate precursor solutions. In (a), it is assumed that open circles represent measurement artifacts (as-deposited films where the part of layered films peeled off during cleaving of the specimens). Errors bars represent the data range. Lines represent the best linear fits. .... 51
- Figure 22. (a) The relationship between the multilayer thickness and number of deposition cycles for specimens prepared by using 0.15 M precursor solutions, 10 minutes holding in the precursor, and other fixed parameters specified in the text. Representative cross-sectional and in-plane SEM images of the multilayers prepared by (b, e) 10, (c, f) 20, and (d, g) 30 deposition cycles, respectively..... 61
- Figure 23. Cross-sectional SEM images of  $\{\text{MMT}-(\text{sol-gel ZrO}_2)\}_{30}$  multilayer synthesized with holding time in air for 45 seconds and 10 minutes. ... 62
- Figure 24. Cross-sectional SEM images of  $\{\text{MMT}-(\text{sol-gel ZrO}_2)\}_{30}$  multilayer for holding 10 minutes and 45 seconds in precursor solutions. Numbers in the bottom row represented sampling positions along the immersion direction, and were calculated dividing the total length of the corresponding multilayers..... 63
- Figure 25. An SEM image of a piece of free-standing, air-dried  $\{\text{MMT}-(\text{sol-gel ZrO}_2)\}_{30}$  multilayer. Inset is an optical photograph of a large piece of freestanding multilayer. .... 64
- Figure 26. (a) The relationship between the film thickness and precursor solution concentration. The holding times in the precursor solutions are labeled. The dashed line and the symbol “X” indicate that the films become non-uniform at high concentrations with prolonged holding time due to the gelation of the solution. As a comparison, the two solid cycles represent the measured thickness for films made by dipping only in MMT suspension (labeled as “Only MMT”) or only in zirconium acetate hydroxide solution (near the origin point, labeled as “No MMT”, holding time = 45 seconds). (b) The relationship between the estimated net thickness for the sol-gel layers grown during 45-second holdings in precursor solutions and the precursor solution concentration. (c) Representative cross-sectional SEM images. The precursor solution concentrations are labeled; holding time = 45 seconds. .... 67

List of Figures (Continued)

Figure 27. (a) The multilayer thickness versus holding time for two different precursor solution concentrations (0.15 M and 0.03 M). (b) a double logarithmical plot of the estimated net thickness of sol-gel layer grown on the MMT surface per cycle versus holding time. (c) Representative cross-sectional SEM images (0.15 M zirconium acetate hydroxide solutions; the holding times are labeled) ..... 70

Figure 28. A representative cross-sectional SEM image for a film made after dipping a substrate in a MMT suspension and rinsing water (twice each cycle) for 30 deposition cycles (i.e., without dipping in a zirconium acetate hydroxide solution). ..... 73

Figure 29. Cross-sectional SEM images of films made via dipping substrates in 0.3 M zirconium acetate hydroxide solutions for 30 deposition cycles with (a) 45 seconds and (b) 10 minutes holding time in the solutions, respectively. 76

Figure 30. The multilayer thickness versus precursor solution aging time at 60 °C for holding time of 45 (Curve I) and (Curve II) 0 seconds, respectively. Curve III represents the net thickness of hydrodynamic deposited sol-gel layers (estimated by subtracting the thickness of MMT layer from Curve II). (b) Representative cross-sectional SEM images of selected multilayers (corresponding to Curve I)..... 80

Figure 31. (a) FTIR spectra of an as-deposited  $\{\text{MMT}-(\text{sol-gel ZrO}_2)\}_{30}$  multilayer and multilayers annealed at different temperatures. All specimens were made using 0.15 M precursor solution and a holding time of 45 seconds. (b) Cross-sectional SEM images of selected annealed multilayers. .... 82

Figure 32. XRD patterns of as-deposited and annealed  $\{\text{MMT}_x-(\text{sol-gel ZrO}_2)\}_{30}$  multilayers. Annealing temperatures are labeled..... 85

Figure 33. Three proposed nanostructures with an increased complexity. .... 90

Figure 34. Cross-sectional and in-plane SEM images of (a) and (b)  $\{\text{MMT-TiO}_2\}_n$  and (c) and (d)  $\{\text{MMT-CeO}_2\}_n$  multilayers. .... 92

Figure 35. (a) Cross-sectional and (b) in-plane SEM images of  $\{\text{MMT}-((\text{CeO}_2-\text{TiO}_2)_2-\text{CeO}_2)\}_n$  multilayers. .... 93

Figure 36. Cross-sectional and in-plane SEM images of (a) and (b): as-deposited and (c) and (d): annealed  $\{(\text{CeO}_2-\text{TiO}_2)_2-\text{CeO}_2-(\text{MMT-ZrO}_2)_2-\text{MMT}\}_n$  multilayers..... 95

List of Figures (Continued)

Figure 37. (a) An optical micrograph and (b) a cross-sectional SEM image of MMT-SnO <sub>2</sub> multilayers. ....	98
Figure 38. An EDS spectrum of a MMT-SnO <sub>2</sub> multilayer. The inset is a table of the apparent (measured) elemental composition. ....	99
Figure 39. (a) An optical micrograph and (b) in-plane and (c) cross-sectional SEM images of a MMT-zinc oxide multilayer. ....	101
Figure 40. An EDS spectrum of MMT-ZnO multilayer. The inset is a table of measured elemental composition. ....	102
Figure 41. Optical micrographs and in-plane and cross-sectional SEM images of MMT-CeO <sub>2</sub> multilayers made using cerium chloride (a, c, e) or cerium nitrate (b, d, f) precursor solutions. ....	105
Figure 42. EDS spectra of as-deposited MMT-cerium oxide multilayers made using (a) cerium chloride and (b) cerium nitrate precursor solutions. The insets are tables of measured elemental compositions. ....	106
Figure 43. (a) In-plane and (b) cross sectional SEM images of MMT-ionic liquid multilayers. ....	108
Figure 44. (a) In-plane and (b) cross-sectional SEM images, and (c) an EDS spectrum of polymer-oxide multilayers. ....	111
Figure 45. An optical micrograph of a SWCNT-zirconia multilayer. ....	112
Figure 46. A conceptual illustration for the multilayers used as filtering membranes with tortuous paths. ....	115
Figure 47. Schematic of micro-cantilevers made of freestanding MMT-zirconia multilayers. ....	115
Figure 48. Photonic clays: a new class of chemical sensors made of spin-coated porous clay-TiO <sub>2</sub> multilayers and the proposed photonic sensor matrix. ....	119
Figure 49. Generic layered 3D nanostructures of nanoclay-nanoparticle based multilayers. ....	124

List of Figures (Continued)

Figure 50. Cross sectional SEM images of ceria films made using (a)  $Ce(NO_3)_3 \cdot 6H_2O$  and  $NH_4OH$  precursors and (b) Arcot's method..... 127

Figure 51. Cross-sectional SEM images of ceria films made with (a)  $Ce(NO_3)_3 \cdot 6H_2O$  and  $NaOH$  precursor solutions, and (b) the recipe adapted from Tolstoy *et al.*'s<sup>214</sup> ..... 128

Figure 52. Optical micrographs of substrates cleaned by (a) method *a*, (b) method *b*, (c) method *c*, (d) method *d*, and (e) method *e*. ..... 132

Figure 53. (a-c) Optical micrographs of pre-cleaned silicon substrates, which were dipped into the MMT suspension exfoliated by method I-III respectively. .... 136

Figure 55. Cross-sectional SEM images of  $\{MMT-CeO_2\}_n$  multilayers synthesized with different pH values of  $CeO_2$  suspensions..... 138

Figure 56. Cross-sectional SEM images of  $\{MMT-CeO_2\}_n$  multilayers made with  $pH_{CeO_2} = pH_{MMT} = 1.3$  (left image) or  $pH_{CeO_2} = pH_{MMT} = 4.3$  (right image)... 140

Figure 57. A schematic of the MMT adsorption on positive nanoparticles with MMT edges positively charged. .... 141

## CHAPTER ONE

### INTRODUCTION

The Langmuir-Blodgett technique was once the major technique to synthesize ultrathin organic films or multilayers<sup>1</sup>. However, this technique requires expensive equipment and long fabrication time. In 1990s, a simpler and more cost-effective layer-by-layer (LbL), electrostatic-assisted self-assembly method, was developed by Decher *et al.* to synthesize polyelectrolyte multilayers<sup>2</sup>. This LbL self-assembly forms multilayer thin films through electrostatic interactions, via alternative adsorption of positively and negatively charged species from solutions. Since then, a wide variety of multilayers have been synthesized with this versatile LbL technique using various building units, where polyelectrolytes/polymers are usually used to “glue” the structures<sup>2-8</sup>. In particular, various nanoclay-polymer multilayers have been synthesized<sup>9</sup>, and these organic-inorganic hybrid multilayers exhibit excellent mechanical and other properties<sup>10</sup>.

On the other hand, all-inorganic multilayers are attractive for applications at high temperature, and they usually exhibit better rigidity and chemical stability than polymer-bearing multilayers. However, before this dissertation study, only a few types of all-inorganic multilayers had been made, and they were mainly made via LbL assembly of oppositely charged nanoparticles<sup>11, 12</sup>.

In this dissertation study, an entirely new class of all-inorganic multilayers,  $\{\text{MMT}_x\text{-(sol-gel ZrO}_2)\}_n$ , has been synthesized for the first time to the author's knowledge. On one hand, permanent negative surface charges of the montmorillonite

(MMT) nanosheets enable electrostatic assisted assembly; furthermore, its unique 2-D nanosheet shape ( $\sim 1$  nm in thickness and  $\sim 100$ - $1000$  nm in the lateral dimension<sup>13, 14</sup>) provides planar surfaces for the growth of the sol-gel films, and it ensures the structural integrity of the resultant multilayer. On the other hand, sol-gel  $\text{ZrO}_2$  is used to “glue” multilayers to further enhance the structure integrity.

The synthesis of  $\{\text{MMT}_x\text{-(sol-gel ZrO}_2)\}_n$  multilayers is described and discussed in Chapter 4 and Chapter 5, after documenting in Chapter 3 a brief study of synthesis of sol-gel  $\text{ZrO}_2$  films as a preliminary study. It is further demonstrated (in Chapter 7) that this method can be extended to make  $\{\text{nanoclay-(sol-gel oxide)}\}_n$  multilayers with other metal oxides (e.g.,  $\text{SnO}_2$ ). These studies have demonstrated feasibility of using sol-gel oxides, instead of polyelectrolytes/polymers, as the “glue” to make multilayers. This represents an innovative concept in nanoscale fabrication.

Furthermore, a class of  $\{\text{nanoclay-(oxide nanoparticle)}\}_n$  multilayers, with a novel “plate-ball” architecture, has been synthesized (again for the first time). Several derivative and more complex multilayer structures have also been made. These studies are documented in Chapter 6. Finally, we also explore the feasibility to synthesize several other types of multilayer structures, including nanoclay-ionic liquid, polymer-oxide multilayers, and carbon nanotube-oxide multilayers. This exploration is documented in Chapter 7.

These all-inorganic  $\{\text{nanoclay-(sol-gel oxide)}\}_n$  and  $\{\text{nanoclay-(oxide nanoparticle)}\}_n$  multilayers offer a platform to do more quantitative studies of growth kinetics and electrostatic assisted assembly mechanisms. In particular, the growth



mechanisms of  $\{\text{MMT}_x\text{-(sol-gel ZrO}_2)\}_n$  multilayers have been investigated in great details to understand the coupling between the growth of MMT and sol-gel  $\text{ZrO}_2$  layers in a LbL process, the kinetics of the sol-gel  $\text{ZrO}_2$  deposition on MMT surfaces, and the possible effects of electrostatic interactions. This mechanism study is documented and discussed in Chapter 5.

Chapter 8 discusses potential applications of  $\{\text{nanoclay-(sol-gel oxide)}\}_n$  and  $\{\text{nanoclay-(oxide nanoparticle)}\}_n$  multilayers as high-temperature filtering membranes, micro-cantilevers, interface-based fast ion conductor, sensors, and protective coatings, based on their all-inorganic building units and distinct structures.

Chapter 2 is a review of literature in the relevant fields, including LbL assembly, the structure and chemistry of clays, colloidal theories, sol-gel chemistry, and dip coating basics. Finally, the conclusions are made in Chapter 9.

CHAPTER TWO  
LITERATURE REVIEW

**1. Layer-by-Layer Self Assembly**

Decher *et al.* developed a layer-by-layer (LbL) self-assembly technique in 1990s to synthesize polyelectrolyte multilayer films<sup>2</sup>. This technique fabricates nanostructured multilayers via sequential deposition of oppositely charged species onto a surface through electrostatic attractions<sup>15-23</sup>. A typical synthesis procedure is schematically shown in Figure 1.

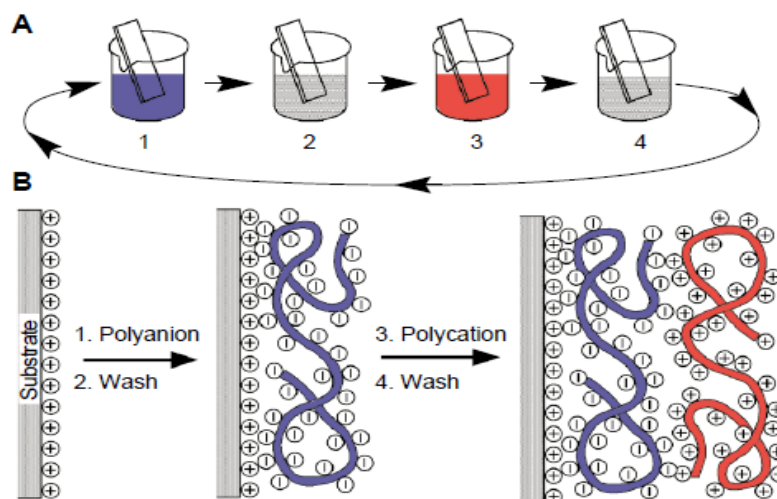


**Figure 1.** Layer-by-layer self assembly of polyelectrolyte multilayers using poly (styrenesulfonate) (PSS) polyanions and poly (allylamine) (PAH) polycations<sup>2</sup>.

A polyelectrolyte multilayer can be prepared by repeating the following four steps (Figure 1). First, a positively charged substrate is dipped into a polyanion (e.g., poly (styrenesulfonate) or PSS) solution. Second, the substrate is rinsed in water, after which

one monolayer of polyanions remained adsorbed on the substrate because of electrostatic attractions. Third, the substrate is dipped into a polycation (e.g., poly (allylamine) or PAH) solution. Fourth, the substrate is rinsed in water again to remove loosely adsorbed polycations. The above four steps are repeated for  $n$  times to deposit a  $\{\text{PSS-PAH}\}_n$  multilayer as an LbL assembly.

Following Decher's work, a wide range of organic and hybrid organic-inorganic films with a broad spectrum of mechanical, electrical, and biological functionalities<sup>15-23</sup> were developed, using building units such as polyelectrolytes, nanoparticles, dyes<sup>24</sup>, proteins<sup>25</sup>, and enzymes. These LbL methods have a number of advantages, including high versatility for film composition, ease of preparation, low cost, precise control of layer thickness<sup>26</sup>, and self-healing<sup>27,28</sup>. These LbL assembled multilayers have a broad range of applications<sup>15-23</sup> and several examples are given as follows: thin and defect-free  $\{\text{PSS-PAH}\}_n$  multilayers are used as membranes to separate gases or remove small impurity ions and molecules<sup>29</sup>.  $\{\text{PAA-PAH}\}_n$  multilayers (where PAA = poly (acrylic acid)) are used to functionalize the interior of porous membranes for gas analysis, selective molecule adsorption and catalytic applications<sup>29</sup>.  $\{\text{PDADMA -PSS}\}_n$  multilayers (where PDADMA = poly(diallyl dimethyl ammonium)) are used as cell scaffold materials due to their good mechanical properties<sup>30</sup>.  $\{\text{PEI-PAA}\}_n$  multilayers (where PEI = polyethylene imine) are used as self-cleaning coatings due to their ultrahydrophobicity<sup>22</sup>.

### ***1.1 Nanoclay-Polymer Multilayers***

In early 1990s, Kleinfeld and Ferguson synthesized  $\{\text{laponite-PDDA}\}_n$ , which was perhaps the first nanoclay-polymer multilayer<sup>27, 31</sup>. Since then, various types of nanoclay-polymer multilayers have been made. Many of such multilayers utilize exfoliated montmorillonite (MMT), in which isomorphous substitution causes net negatively charged surfaces<sup>32</sup>, enabling electrostatic assembly. Furthermore, the high aspect ratio of exfoliated MMT of  $\sim 1$  nm in thickness and 100-1000 nm in lateral dimension<sup>33</sup> provides a planar surface for the deposition and growth of oppositely charged units. Recently, this class of polymer-nanoclay multilayers has attracted great attention<sup>9, 10, 15, 25, 27, 31, 34-37</sup>. In particular, Kotov's group prepared  $\{\text{PDDA/MMT}\}_n$  multilayers to mimic natural brick-and-mortar structure in natural nacre<sup>38, 39</sup>. The multilayers exhibited good mechanical properties. For example, a 2.4- $\mu\text{m}$ -thick multilayer ( $n = 100$ ) had a Young modulus of 10 GPa. Kotov's group also prepared a  $\{\text{PVA/MMT}\}_n$  multilayer with non-polyelectrolyte polymers; after treating with glutaraldehyde (for cross-linking), this multilayer exhibited an even higher Young modulus of 106 GPa, which was close to those of steels<sup>10</sup>. Their studies demonstrated that nanocomposites can possess the promised superior mechanical (and perhaps other) properties with controlled nanoscale fabrication<sup>40-46</sup>. Nanoparticles (e.g., magnetic  $\text{Fe}_3\text{O}_4$ <sup>47</sup>) and biomaterials (e.g., L-3,4-dihydroxyphenylalanine- lysine- polyethylene glycol (DOPA-Lys-PEG)<sup>25</sup>) may also be incorporated into such nanoclay-polymer multilayers. These nanoclay-polymer based multilayers have a wide range of potential applications,

such as gas membranes<sup>34</sup>, diffusion barriers<sup>21</sup>, mechanically protective coatings<sup>9,10</sup>, sensor materials<sup>48,49</sup>, anti-corrosion coatings<sup>50</sup>, and microcantilevers<sup>51</sup>.

### ***1.2 All-Inorganic Multilayers***

To date, a majority of the electrostatically assembled films consist of either all or partial polyelectrolyte layers that serve as the “electrostatic glue” for structural integrity. On the other hand, all-inorganic multilayers are attractive for applications in high-temperature environments, and they usually exhibit better rigidity and chemical stability than polymer-bearing multilayers. Only a few types of multilayers with primarily inorganic building units, typically nanoparticles, have been synthesized. In 1966, Iler *et al.* at DuPont developed probably the first electrostatically assembled multilayers using SiO<sub>2</sub> and boehmite fibrils<sup>52</sup>, although this work did not receive much attention at that time. In 2006, Lee *et al.* at MIT re-examined the possibility of making “all-nanoparticle” multilayer films through LbL electrostatic assembly using TiO<sub>2</sub> and SiO<sub>2</sub> nanoparticles<sup>11,12</sup>, and they controlled the multilayer growth with deposition cycles and the pH of suspensions. In 2008, they further made multilayers of oppositely charged SiO<sub>2</sub> nanoparticles with altered surface charges via surface modification<sup>53</sup>. In the same year, another synthesis of multilayers of MnO<sub>2</sub> nanosheets and layered double hydroxides was reported<sup>54</sup>. In 2009, another MIT group synthesized all carbon nanotube multilayers<sup>55</sup> and carbon nanotube/Au nanoparticle thin films<sup>56</sup>, both involving surface modification to alter surface charges. Other examples include multilayers of coated Au/Ag nanoparticles<sup>57,58</sup> and modified CdS/TiO<sub>2</sub> nanoparticles, and polyelectrolyte-glued multilayers of

$\{\text{TiO}_2\text{-Ti}_{1-\delta}\text{O}_2\}_n$ <sup>59</sup>,  $\{\text{Ag-Ti}_{1-\delta}\text{O}_2\}_n$ <sup>60</sup>, and  $\{\text{clay-Fe}_3\text{O}_4\}_n$ <sup>47, 61</sup>. All of these primarily inorganic multilayers were based on inorganic nanoparticles, including nanotubes and nanosheets, and many of them employed surface modifications using organic species to enable electrostatic assembly.

### ***1.3 Fundamental Studies of LbL Assembly Mechanisms***

Extensive prior studies have been conducted to investigate how various experimental parameters affect the growth, structure, and properties of synthesized polyelectrolyte based multilayers. The nature of the polyelectrolyte, ionic strength and pH of the solution are among the key experimental parameters. First, it was demonstrated that the type of the polyelectrolyte critically affect bonding energy and equilibration time of interacting polymers<sup>62</sup>, but polyelectrolyte concentrations has little effect on the multilayer growth<sup>18</sup>. Second, use of a high ionic strength will generally increase thicknesses, densities, and surface roughness of the multilayers<sup>18</sup>. Third, the pH of a solution has complex influences on multilayer synthesis, as it changes both the ionic strength of the solution and the charges of polymer chains<sup>63, 64</sup>. Finally, changes in these key parameter can affect the structural stability<sup>65</sup>, optically properties<sup>66</sup>, and wettability<sup>67</sup> of the resultant multilayers.

It should be noted that polyelectrolyte associations during a LbL assembly are fundamentally ion exchange processes, where polycation-anion and polyanion-cation associations are replaced by polycation-polyanion associations<sup>20, 68</sup>. Thermodynamically, the association of polycation-polyanion is driven largely by entropy (as a result of the

release of counter-ions and hydration water molecules from a dissolution of the polyelectrolyte chains)<sup>68</sup>. Haynie *et al.*<sup>69</sup> investigated the formation of {PSS/PAH}<sub>n</sub> using a wide range of ionic strength via isothermal titration calorimetry, and they have drawn a similar conclusion that the LbL assembly process is entropy-driven nature.

Usually, LbL assembly happens through electrostatic interactions. However, other kinds of physicochemical interactions, such as hydrogen bonding, covalent attachment, biological recognition, hydrophobic interactions, ionic charge transfer and metal-ligand interactions<sup>20, 70</sup>, can also play significant roles at specific conditions. For example, hydrogen bonding interactions are the driving forces for the growth of polyelectrolyte multilayers made of neutral poly(vinylpyrrolidone) (PVV), poly(vinyl alcohol) (PVA), poly(acrylamide) (PAAm), and poly(ethylene oxide) (PEO)<sup>71</sup>. In nanoclay-polymer multilayers, MMT surfaces can absorb polymers by electrostatic attractions or hydrogen bonding (Figure 2). Tang attributed the good cohesion between PDDA and MMT to the pinning of each segment of the polymer chains by a strong ionic bonding (Figure 2a)<sup>37</sup>. Podsiadlo suggested both the hydrogen bonding and the six-atom ring formed between PVA and Al (of montmorillonite) contributed to the good mechanical properties (Figure 2b and c).

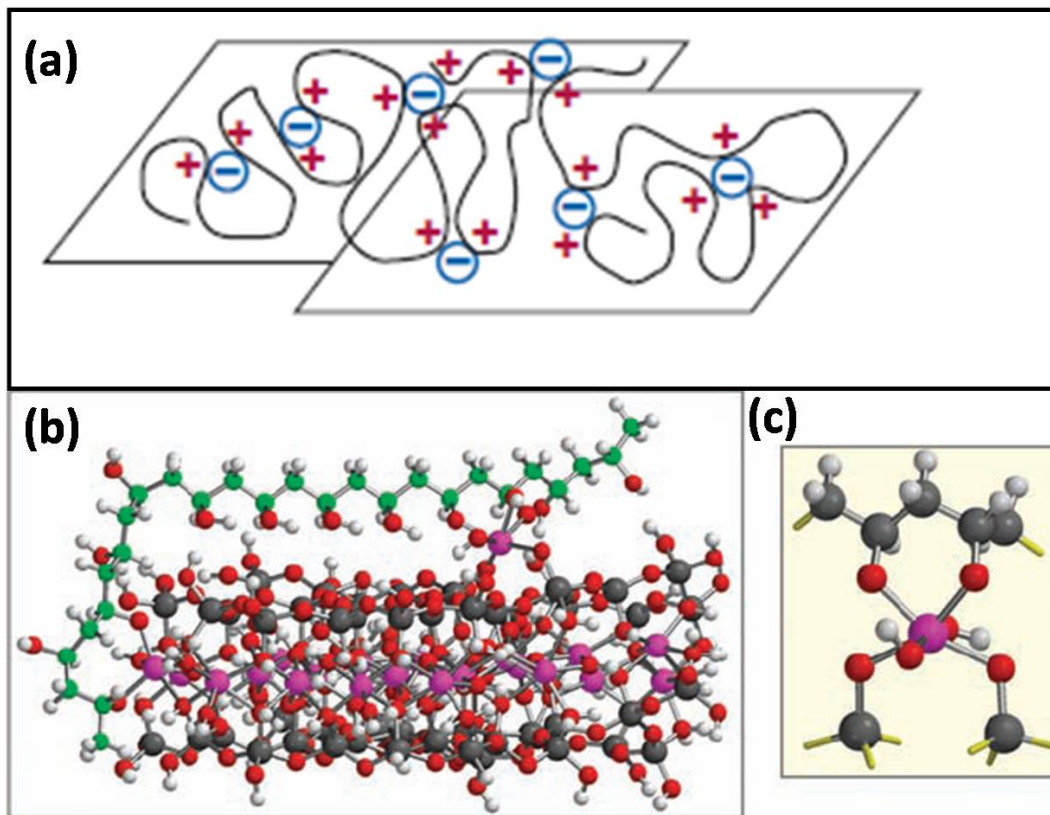


**Figure 2.** (a) Polycations fold and pair with nanoclays <sup>9</sup>. (b) A molecular structure of the bonding between PVA and MMT <sup>10</sup>. (c) An enlarged six-membered ring formed between PVA and MMT. Al, purple; O, red; H, light gray; Si, dark gray; C, green.

## 2. Clay Materials

### 2.1 Clay structure

Clay minerals are categorized as amorphous and crystalline groups, as shown in Table 1. For crystalline groups, a repeatable unit is composed of  $m$  layers of silica tetrahedrons ( $\text{SiO}_4^{4-}$ ) and  $n$  layers of octahedrons. Each tetrahedron shares three O atoms with the neighbor units to form a hexagonal network, and the basic structural unit of the tetrahedral layer is  $\text{Si}_2\text{O}_5^{2-}$ . Apical O atoms from the silica tetrahedral layer, hydroxyls (in



the center of a hexagonal unit) and metal (e.g., Al, Mg) cations form octahedrons in the octahedral layer. There are two types of octahedral layers, dioctahedral or trioctahedral, with different occupation ratios of the octahedron centers. If  $\text{Al}^{3+}$  is the only metal embedded in the octahedron center, two-thirds of the octahedron centers will be occupied for a charge balance. This structure is called as dioctahedral. If every two  $\text{Al}^{3+}$  cations in the dioctahedral layer are replaced by three  $\text{Mg}^{2+}$  cations, all octahedron centers will be occupied; this structure is called as trioctahedral.

**Table 1.** Classification of clay minerals <sup>72</sup>

<p>I. Amorphous</p> <p style="padding-left: 40px;">Allophane group</p>
<p>II. Crystalline</p> <p style="padding-left: 40px;">A. Two-layer types (sheet structures composed of one layer of silica tetrahedrons and one layer of alumina octahedrons): kaolinite, nacrite, halloysite, <i>etc.</i></p> <p style="padding-left: 40px;">B. Three-layer types (sheet structures composed of two layers of silica tetrahedrons and one central dioctahedral or trioctahedral layer): montmorillonite, sauconite, vermiculite, nontronite, saponite, hectorite, illite <i>etc.</i></p> <p style="padding-left: 40px;">C. Regular mixed-layer types (an ordered stacking of alternative layers of different types): chlorite, <i>etc.</i></p>

D. Chain-structure types (hornblende-like chains of silica tetrahedrons linked together by octahedral groups of oxygen and hydroxyls containing Al and Mg atoms): attapulgite, sepiolite, palygorskite, *etc.*

Montmorillonite (MMT) is three-layer type crystalline clay (Table 1), and its structure is shown in Figure 3. The chemical formula of the unit is  $\text{Si}_8\text{Al}_4\text{O}_{20}(\text{OH})_4$ . One feature of the MMT structure is that three-layer units have permanent negative surface charges; these charges not only promote the electrostatic self-assembly process, but also render a high lateral bond strength within the constructed multilayers or their precursors<sup>15</sup>. The surface charges are resulted from isomorphous substitution (e.g., substitution of  $\text{Si}^{4+}$  by  $\text{Al}^{3+}$  in tetrahedron units), and they are balanced by exchangeable cations between units.

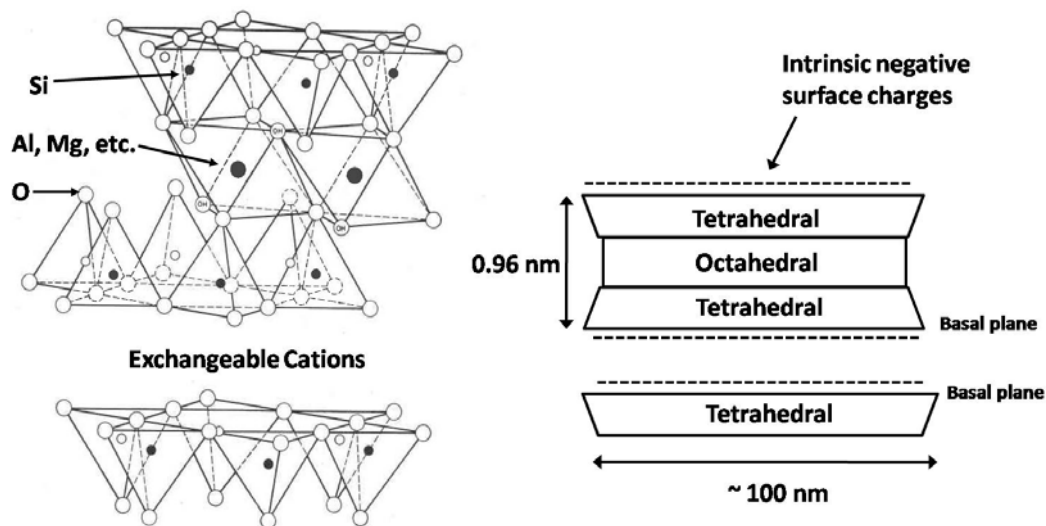


**Figure 3.** The montmorillonite structure<sup>73</sup>.

The three-layer unit in MMT has a high aspect ratio. The unit thickness is  $\sim 1$  nm, while the lateral size of clay platelets is from  $\sim 100$  nm to  $\sim 1\text{-}2$   $\mu\text{m}$ <sup>13,14</sup>. This high aspect ratio of platy nanoclays provides an ideal planar surface for the growth of other materials and self-assemblies of nanomaterials. For three-layer type clays, tetrahedral layers can distort in lateral directions and dioctahedral layers can be stretched and thinned.

## ***2.2 Cation exchange***

Clay materials are able to exchange cations with the cations in a solution. The cation exchange capacity (CEC) measures in a unit of milliequivalents per 100 g (meq/100g). Representative CEC values of clay materials are listed in Table 2. Typically, three-layer type clays (smectite and vermiculite) have higher CEC. The actual CEC value depends on the particle size, as well as the grinding methods or heat treatments that have been used.

Exchangeable cations of three-layer type clays are mostly located on surfaces of basal layers, which neutralize negative charges caused by isomorphous substitutions. A small number of exchangeable cations are at edges of clay platelets, which neutralize negative charges caused by broken bonds. For example, surface exchangeable cations account for 80 % total CEC of smectite, and edge exchangeable cations account for the rest 20%<sup>72</sup>.

**Table 2.** Cation exchange capacity of clay minerals (meq/100g) <sup>72</sup>.

Kaolinite	3-15
Halloysite 2H <sub>2</sub> O	5-10
Halloysite 4H <sub>2</sub> O	40-50
Smectite	80-150
Illite	10-40
Vermiculite	100-150
Chlorite	10-40
Sepiolite-attapulgit-palygorskite	3-15

The easiness and the ratio of exchangeable cations that can be replaced are affected by many factors: the concentration of replacing cations in the solution, the population of exchange positions, the type of anions in the replacing solution, the nature of clay materials and cations, and the heat treatment history of clay materials <sup>72</sup>. In general, cations with higher valence charges and larger ion size can replace others more easily, and they are harder to be replaced. Empirically, exchangeable cations can be replaced in the following order: Na<sup>+</sup> <sup>74</sup> (Na<sup>+</sup> is easiest to be replaced).

### ***2.3 Swelling in aqueous suspensions***

MMT swells when it is dispersed in an aqueous solution or exposed to a moisture environment. Norrish *et al.* divided the swelling into three stages <sup>75</sup> (**Error! Not a valid bookmark self-reference.**). In the first stage, water molecules penetrate inside clays and

hydrolyze interlayer cations. The released hydration energy (e.g., 114 kcal per g for Na<sup>+</sup> hydration) may overcome the electrostatic attractive force between layers, increasing the interlayer spacing to ~ 2 nm. In the second stage, an electrical double layer forms, resulting an interlayer repulsion and increasing the interlayer spacing further to ~ 3- 10 nm. In the third stage, the interlayer spacing further increases and it is only limited by the volume of water that is supplied.

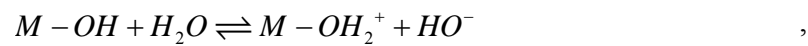
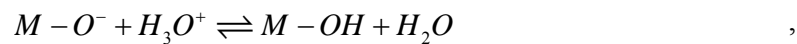
**Table 3.** The swelling behavior of montmorillonite in water <sup>76</sup>.

Region or stage	State of clay-water system	X-ray diffraction pattern	Water content (g g <sup>-1</sup> )	Swelling pressure (dyne cm <sup>-2</sup> )	Nature of interlayer forces	
					Repulsive	Attractive
1	Solid, crystalline	Sharp	0- ~ 0.7	~ 4 × 10 <sup>9</sup>	Cation hydration	Electrostatic
2	Paste-gel	Very diffuse maxima	0.7- ~ 20	10 <sup>7</sup> -10 <sup>5</sup>	Diffuse double layer interaction	Frictional, edge-to-face bonds
3	Gel-sol	Only central scatter	>20	<10 <sup>5</sup>	Diffuse double layer interaction and thermal motion	Edge-to-face and edge-to-edge bonds

### 3. Colloid Chemistry

#### 3.1 Point of zero charge

Oxide surfaces usually have hydroxyl groups ( $M-OH$ ) due to chemisorptions of water molecules, as shown in Figure 4. These surface groups can be ionized via acid-base chemical reactions:



which produce charged surface groups,  $M-O^-$  or  $M-OH_2^+$ . The certain pH value, at which the oxide surface is neutral, is defined as the “point of zero charge” (PZC). If the actual  $pH > PZC$ , then the oxide surface is negatively charged; if the actual  $pH < PZC$ , then the oxide surface is positively charged.

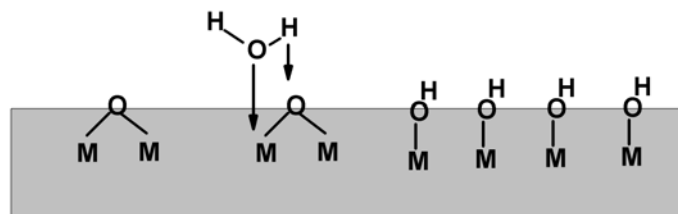


**Figure 4.** Water chemisorptions on an oxide surface <sup>77</sup>.

PZC values are affected by several factors, which include the chemistry and structure of the oxide, particle morphology, and heat treatment and physicochemical histories <sup>77</sup>. In general, oxides with cations of small size and high valence charges have low PZC values (as shown in Table 4), because surface groups become acidity.

**Table 4.** Point of zero charge of several oxides<sup>77, 78</sup>.

<b>z</b>	<b>Oxide</b>	<b>PCN</b>
+II	MgO	≈ 12.5
	ZnO	9-10
+III	α-Fe <sub>2</sub> O <sub>3</sub>	5.5-9
	α-Al <sub>2</sub> O <sub>3</sub>	6.5-10
+IV	TiO <sub>2</sub>	3.5-6.5
	SiO <sub>2</sub>	2-4
+V	Sb <sub>2</sub> O <sub>5</sub>	≈ 0.5
+VI	WO <sub>3</sub>	≈ 0.4

### 3.2 Electrical double layer

A charged oxide surface attracts counter ions in suspensions through electrostatic interactions. An electrical double layer (EDL), which is composed of surface charges and counter ions, forms. Historically, the Helmholtz model, the Gouy-Chapman model, and the Stern model were used to explain the formation of an EDL. The Gouy-Chapman model (Figure 5) considers the effects of both electrostatic interactions and thermal motions of ions. In this model, concentrations of local cations or anions are given by:

$$c_i = c_i^0 \cdot e^{-W_i/k_B T} \quad (1),$$

where  $c_i^0$  is the bulk concentration of ion  $i$ ,  $W_i$  is the electric work to move ion  $i$ ,  $k_B$  is the Boltzmann constant, and  $T$  is temperature. Then, the local charge density of monovalent salt is given by:

$$\rho_e = e(c^+ - c^-) = c_0 e \cdot \left( e^{-\frac{e\psi(x,y,z)}{k_B T}} - e^{\frac{e\psi(x,y,z)}{k_B T}} \right) \quad (2).$$

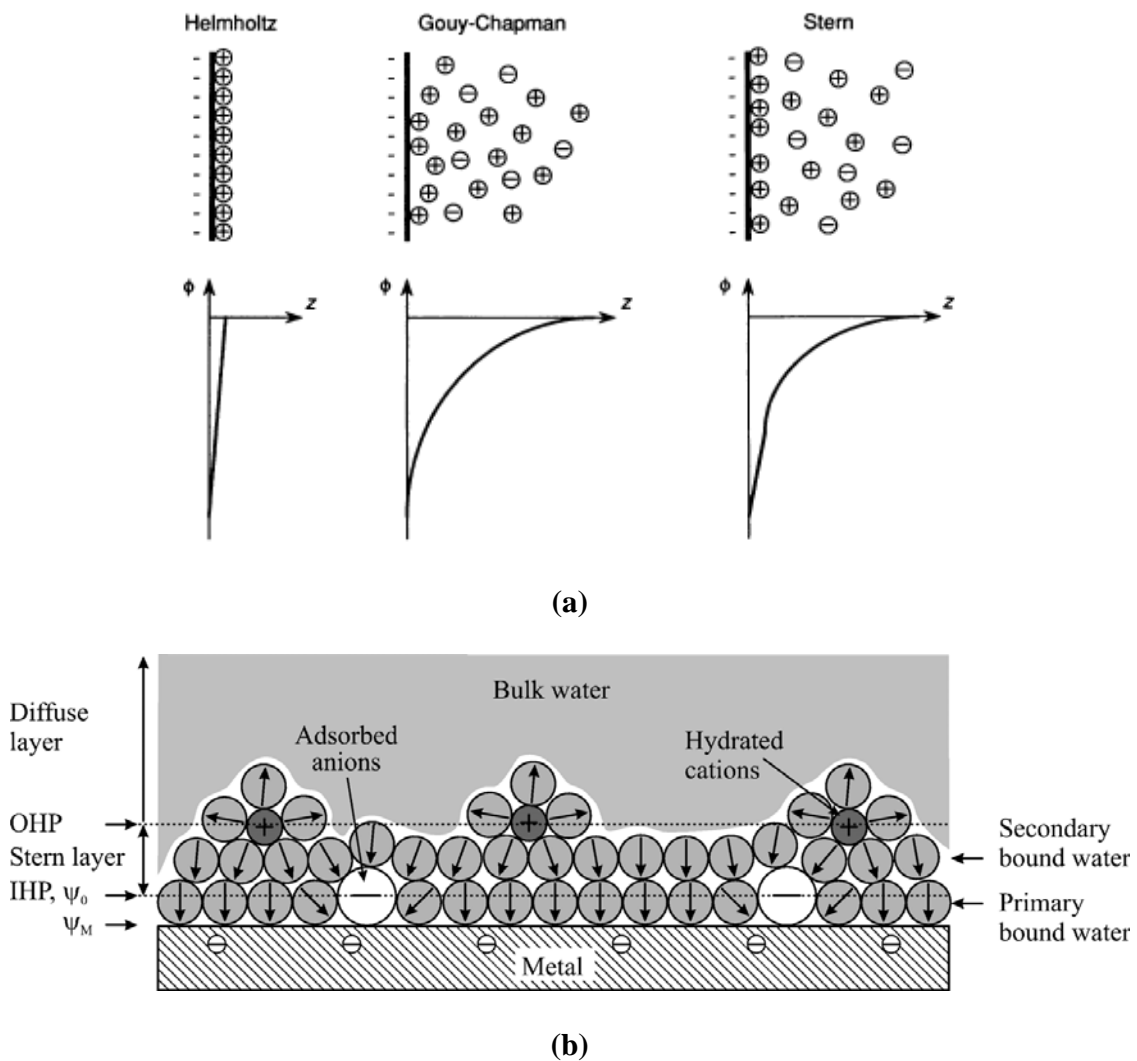


**Figure 5.** (a) EDL models, Helmholtz, Gouy-Chapman, and Stern (from left to right), and the corresponding electrical potential ( $\phi$ ) plots for negatively charged surfaces <sup>79</sup>. (b)



EDL of Stern model for a negatively charged metal surface, showing the inner Helmholtz (IHP), Stern layer, the outer Helmholtz (OHP), and the diffuse layers<sup>80</sup>.

Poisson equation ( $\nabla^2\psi = -\frac{\rho}{\varepsilon}$ ) is used to calculate the electrical potential near a charged planar surface, and the potential is solved as

$$\psi = \psi_0 \cdot e^{-\kappa x} \quad (3),$$

where  $\psi_0$  is the surface potential and

$$\kappa = \sqrt{\frac{2c_0e^2}{\varepsilon\varepsilon_0k_B T}} \quad (4).$$

The electrical potential decreases exponentially from the surface, and the decay length ( $\lambda_D = \kappa^{-1}$ ; Debye length) is related to the ionic strength and the solution dielectric constant.

Stern further combined Helmholtz and Gouy-Chapman models, dividing the double layer into one layer of immobile ions (Stern layer), which are directly adsorbed on the surface, and one layer of mobile ions (diffuse layer), as shown in Figure 5 (b). The Stern layer has chemically and physically bonded cations, anions, and water molecules, which form a “surface complex”<sup>81</sup>. In the Stern layer, the electrical potential drops linearly, and the potential at the outer boundary is called as zeta potential ( $\psi_\zeta$ ), which is directly related to the electrokinetic properties.

### 3.3 Stability of colloids

Derjaguin, Landau, Verwey, and Overbeek (DLVO) theory explains the stability of colloids from interactions between the attractive van der Waals force and the repulsive electrostatic double-layer force<sup>80</sup>. The van der Waals force includes three types of intermolecule forces: Keesom force, Debye force, and London dispersion force. Keesom force describes the interactions between freely rotating permanent dipoles. Debye force describes the interactions between permanent and induced dipoles. London dispersion, which is usually the major component of van der Waals force, describes the interactions between non-polar molecules using a quantum mechanical perturbation theory.

The electrostatic double-layer force arises as the two EDLs overlap. This is illustrated in Figure 6. If surface potentials of charged surfaces are held constant, then the potential gradient and the surface charge density ( $\sigma = -\epsilon\epsilon_0 \frac{d\psi}{d\xi} \Big|_{\xi=0}$ ) decrease when two surfaces become closer. Consequently, the total Gibbs free energy increases, resulting in a repulsion between two EDLs<sup>80</sup>.

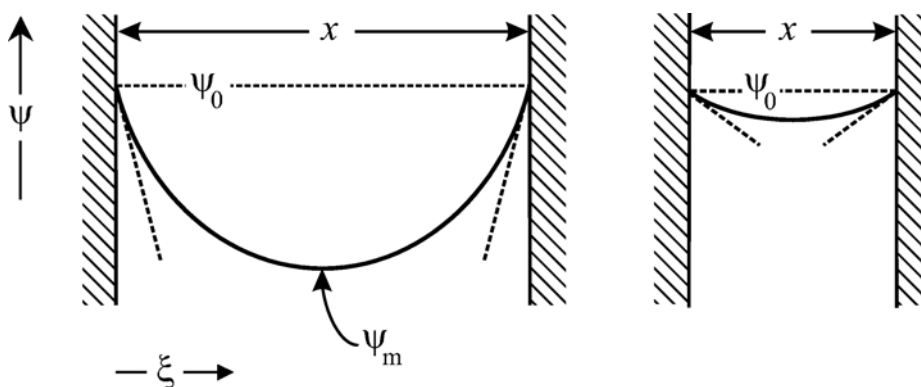


**Figure 6.** A schematic illustration of the origin of the electrostatic double-layer interactions<sup>80</sup>.

When both the van der Waals force and the electrostatic double-layer force are considered, the energy per unit area between two infinitely extended solids with a distance  $x$  is expressed as:

$$w(x) = 64c_0k_B T \lambda_D \cdot \tanh^2\left(\frac{e\psi_0}{4k_B T}\right) \cdot e^{-x/\lambda_D} - \frac{A_H}{12\pi x^2} \quad (5)^{80},$$

where  $c_0$  is the electrolyte concentration,  $\lambda_D$  is the Debye length of the EDL, and  $A_H$  is the Hamaker constant. A typical potential energy vs. the distance between two charged surfaces is plotted in Figure 7. At a short distance, the strong van der Waals attraction results in a “primary minimum” in Figure 7, and colloid particles coagulate. The coagulation may be broken if colloid particles absorb enough energy to overcome the energy barrier (“ $V_{MAX}$ ” in Figure 7). At a larger distance, a secondary energy minimum can arise as a balance of the attractive van der Waals force and repulsive electrostatic force, stabilizing a colloidal.

Experimentally, the stability of a colloid is affected by the ionic strength and the pH value. Increasing electrolyte concentrations or using high valence charge electrolyte ions will decrease the Debye length and the repulsive electrical double layer force, causing aggregations. Changing the pH of a suspension will change the surface charges and the surface potential of the colloid particles, and colloid particles aggregate as pH is close to isoelectric point ( $\approx$  PZC). In addition, applying a organic coating as a steric barrier can increase the stability of colloids<sup>82</sup>.

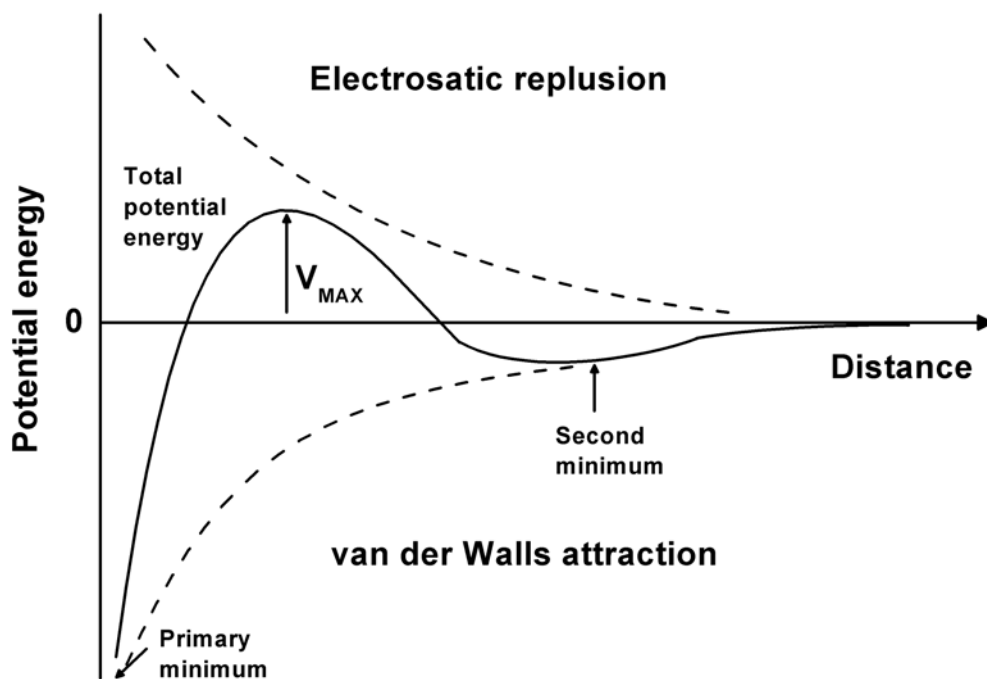


**Figure 7.** A schematic of the potential energy vs. the particle distance, following the DLVO theory<sup>82</sup>.

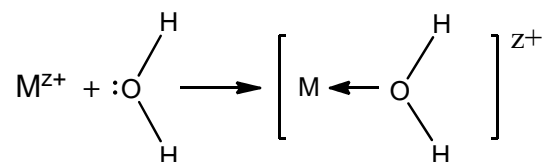
#### 4. Sol-Gel Chemistry

Inorganic salts can be used as sol-gel precursors to prepare oxide ceramics and glass. Because of the versatility of reaction products and reaction paths, hydrolysis and condensation reactions of inorganic salts are generally complex. Partial charge model<sup>82-84</sup> using a electronegativity equalization concept is a convenient tool to understand such reactions. If a hydrolysis/condensation reaction happens, the charge will transfer from one atom to the other until electronegativities equal. Consequently, atoms will have partial positive ( $\delta^+$ ) or negative ( $\delta^-$ ) charges. The electronegativity ( $\chi$ ) is assumed to

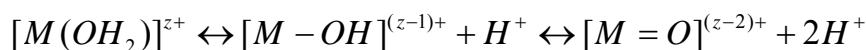
change linearly with the partial charge:  $\chi_i = \chi_i^0 + \eta_i \delta_i$ , where  $\chi_i^0$  is the electronegativity of atom  $i$  and  $\eta_i = k\sqrt{\chi_i^0}$ .

#### 4.1 Hydrolysis

When metal cations ( $M^{z+}$ ) and anions ( $X^{z-}$ ) of inorganic salts (MX) disassociate in an aqueous solution,  $M^{z+}$  cations attract water molecules to form  $[M(OH_2)_N]^{z+}$  as



where  $N$  is the coordination number. During this solvation process, polar water molecules form partially covalent bonds with  $M^{z+}$ , and charges transfer from the water to the metal. As a result, hydrogen atoms have positive partial charges, and the water molecules, as a whole, become acidic. With an increasing magnitude of electron transfers, the hydrated cations react as



Thus, the three possible ligands are aquo (M-(OH<sub>2</sub>)), hydroxo (M-OH), and oxo (M=O).

The actual hydrolysis products,  $[MO_NH_{2N-h}]^{(z-h)+}$ , usually can have more than one type of ligands and form multiple types of complex structures. Consequently, for a different hydrolysis molar ratio ( $h$ ), aquo-ion ( $h = 0$ ), oxy-ion ( $h = 2N$ ), aquo-hydroxo ( $h < N$ ), oxo-hydroxo ( $h > N$ ), or hydroxo ( $h = N$ ) complexes can be resulted<sup>82</sup>. A “charge-pH” diagram summaries observations of hydrolyzed inorganic precursors as a function of the formal charge  $z$  of the cation and the pH of aqueous solutions. An example is shown in

Figure 8, where three domains of aquo ( $[M(OH_2)_N]^{z+}$ ), hydroxo ( $[MO_NH_{2N-h}]^{(z-h)+}$ ), and oxo ( $[MO_N]^{(2N-z)-}$ ) are marked. For a formal charge  $z = 4$ , cations can have many types of hydrolyzed complexes, such as aquo-hydroxo, hydroxo, oxo-hydroxo, or oxo ions, over a wide range of pH.

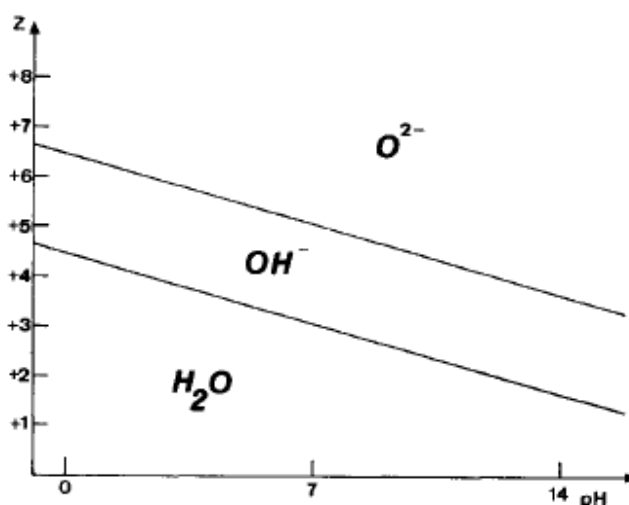
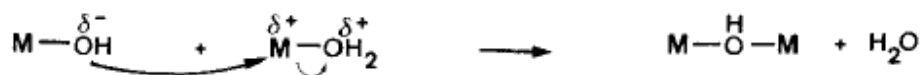


**Figure 8.** A typical “charge-pH” diagram <sup>84</sup>.

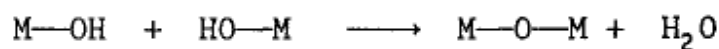
Ligands of hydrolyzed complexes function differently in condensation reactions. Oxo ligands ( $M=O$ ) of oxo-ions ( $[MO_N]^{(2N-z)-}$ ) are good nucleophiles and poor leaving groups, because the partial charge of  $O$  is strongly negative ( $\delta(O) \ll 0$ ) and the partial charge of  $M$  is slightly positive. Aquo ligands ( $M-(OH_2)$ ) of aquo-ions ( $[M(OH_2)_N]^{z+}$ ) are leaving groups, because the partial charge of  $M$  is strongly positive ( $\delta(M) \gg 0$ ) and the partial charge of water is slightly positive ( $\delta(H_2O) > 0$ ). Hydroxo ligands ( $M-OH$ ) of hydrolyzed complexes ( $[MO_NH_{2N-h}]^{(z-h)+}$ ) can be both nucleophiles and leaving groups.

## 4.2 Condensation

Condensation reactions can happen via ololation with hydroxo-aquo precursors ( $[M(OH)_h(OH_2)_{N-h}]^{(z-h)+}$ ) or via oxolation with oxo-hydroxo precursors ( $[MO_h(OH)_{N-h}]^{(N+h-z)-}$ ). In ololation processes, nucleophilic hydroxo ligands (M-OH) substitute leaving groups, aquo ligands (M-(OH<sub>2</sub>)), forming hydroxo bridges (M-OH-M; “ol”). An example of ololation reaction is



In oxolation processes, nucleophilic hydroxo ligands (M-OH) substitute leaving groups, hydroxo ligands (M-OH) or aquo ligands (M-(OH<sub>2</sub>)), forming oxo bridges (M-O-M). An example of oxolation reaction is



Charged hydroxo-aquo precursors,  $[M(OH)_h(OH_2)_{N-h}]^{(z-h)+}$  with  $z-h \geq 1$ , can form polycations, but they cannot condense infinitely to form a solid phase. It is because the nucleophilic strength of hydroxo ligands decreases ( $\delta(OH)$  changes from negative to neutral or positive) during the condensation process. However, zero charged hydroxo-aquo precursors,  $[M(OH)_h(OH_2)_{N-h}]^{(z-h)+}$  with  $z = h$ , can condense infinitely via ololation to form a solid phase (either a gel or a precipitate<sup>84</sup>). For oxo-hydroxo precursors ( $[MO_h(OH)_{N-h}]^{(N+h-z)-}$ ), even they are neutral ( $N+h-z=0$ ), condensations via oxolation may still be limited. This is due to the loss of the nucleophilic strength of hydroxo ligands during the condensation process.

## 5. Dip Coating Processing

Dip coating is used for the LbL self-assembly and the sol-gel film synthesis. Films form during the withdrawal step. Figure 9 schematically illustrates a dip coating process for a sol-gel film deposition. When a substrate is withdrawn from a liquid bath, a film of liquid is hydrodynamically entrained and moves upward. At the stagnation point ( $S$ ), the position where a balance among the viscous drag, the liquid-vapor surface tension ( $\gamma_{LV}$ ), and the gravity force is achieved, the upward moving liquid splits, as shown in Figure 9. The thickness of the entrained solution (the inner layer) can be calculated by the Landau-Levich-Derjaguin equation<sup>85</sup>:

$$h_0 = 0.94(\eta U_0)^{2/3} / \gamma_{LV}^{1/6} (\rho g)^{1/2} \quad (6),$$

where  $\eta$  is the viscosity,  $U_0$  is the withdrawal speed, and  $\rho$  is the solution density. The entrained solution thins along the withdrawal direction, and the profile of this liquid film is affected by evaporation. For a planar substrate, the evaporation rate is

$$E(x) = -D_v a x^{-1/2} \quad (7)^{86},$$

where  $D_v$  is the diffusion coefficient of the vapor,  $a$  is a constant, and  $x$  is the distance from the drying point (“ $x = 0$ ” in Figure 9). Accordingly, the liquid film has a parabolic shape<sup>86</sup>

$$h(x) \sim x^{1/2} \quad (8),$$



and it has a wedge shape if evaporation rate is a constant. Close to the drying point, the capillary pressure ( $P_c = -2\gamma_{LV} \cos(\theta) / r_p$ ) is large as interfacial curvatures are significant, drying the liquid film to a gel.

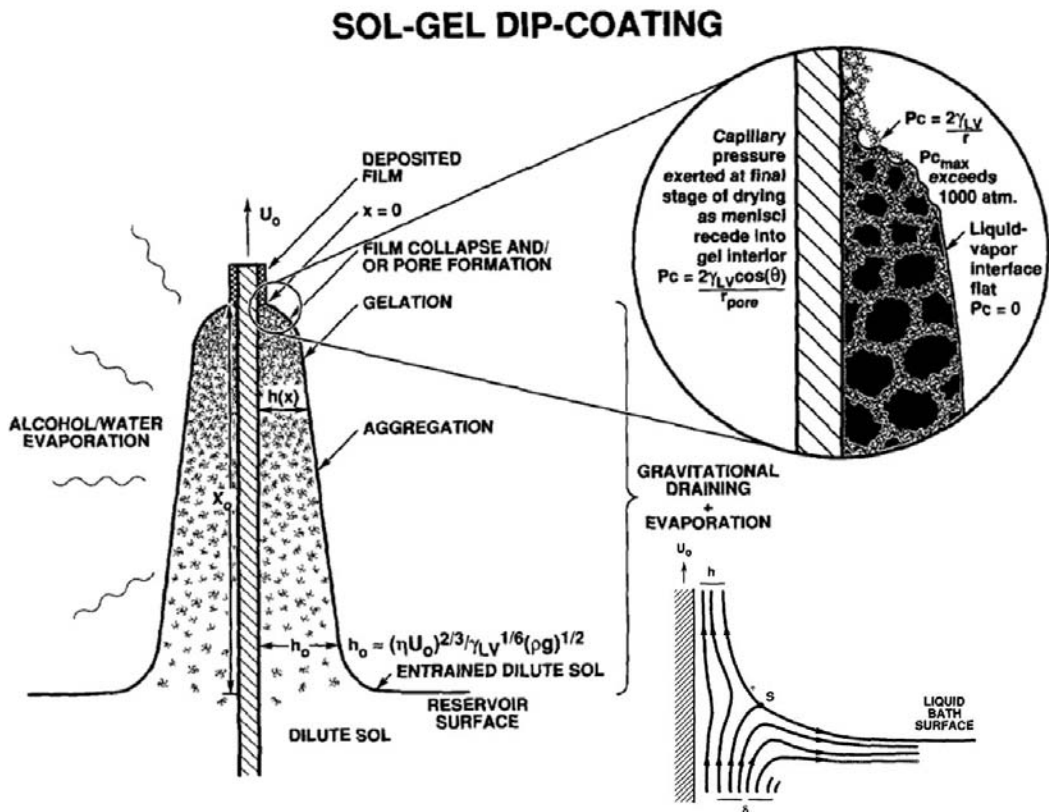


**Figure 9.** Schematic illustration of sol-gel dip coating<sup>85</sup>.

## CHAPTER THREE

### SYNTHESIS OF OXIDE FILMS

#### 1. Introduction

Synthesis of oxide films by aqueous solutions is a cost-effective alternative technique to physical or chemical vapor phase deposition methods<sup>87, 88</sup>. These solution-based film deposition techniques are low-temperature processes, and they only require simple equipment<sup>87, 88</sup>. Four solution-based film deposition methods, chemical bath deposition, liquid phase deposition, electroless deposition with catalyst, and successive ionic layer adsorption and reaction (SILAR)<sup>87, 88</sup>, are commonly used.

Nicolau *et al.*<sup>89</sup> developed the SILAR process in the middle 1980's as a liquid-phase counterpart to the gas-phase atomic layer epitaxy/deposition (ALE/ALD). The conventional SILAR process is schematically depicted in Figure 10. In this method, each deposition cycle consists of four steps. First, a substrate is immersed into a cationic solution, where metal cations are adsorbed. Second, the substrate is rinsed in a solvent (usually deionized water) to remove loosely adsorbed cations. Third, the substrate is immersed into an anionic solution where a monolayer of desired materials will form from a reaction. Fourth, the substrate is rinsed again to remove extra anions. These four steps are repeated to grow films layer by layer. This deposition process can be easily controlled by a computer.

The SILAR technique has been used to synthesize sulfide films (e.g., CdS, ZnS, CuS, In<sub>2</sub>S<sub>3</sub>, PbS, Ag<sub>2</sub>S, MoS<sub>2</sub>, Ni<sub>2</sub>S, As<sub>2</sub>S<sub>3</sub>), selenide films (e.g., Bi<sub>2</sub>Se<sub>3</sub>) and oxide films (e.g., ZnO, CeO<sub>2</sub>)<sup>90</sup>. Notably, this technique has been used for making ultrathin (e.g., 1-

10 nm) gate dielectric oxide films<sup>91,92</sup> and combined with a hydrothermal annealing process for low-temperature synthesis of nanocrystalline oxide films<sup>93</sup>. The conventional SILAR shows low growth rate<sup>(87,88)</sup>. To obtain submicron-meter-thick films, thousands of dipping cycles are required, which will impose great challenges in controlling the film uniformity and defect formation. Various modifications of the SILAR method have been reported to increase the deposition rates. For example, Mitra *et al.* prepared ZnO films with a non-rinsing procedure, and they achieved a film growth rate of 25 nm per cycle. Gao *et al.* applied the ultrasonic rinsing to prepare ZnO films and obtained film growth rate of ~ 4 nm per cycle<sup>90</sup>.

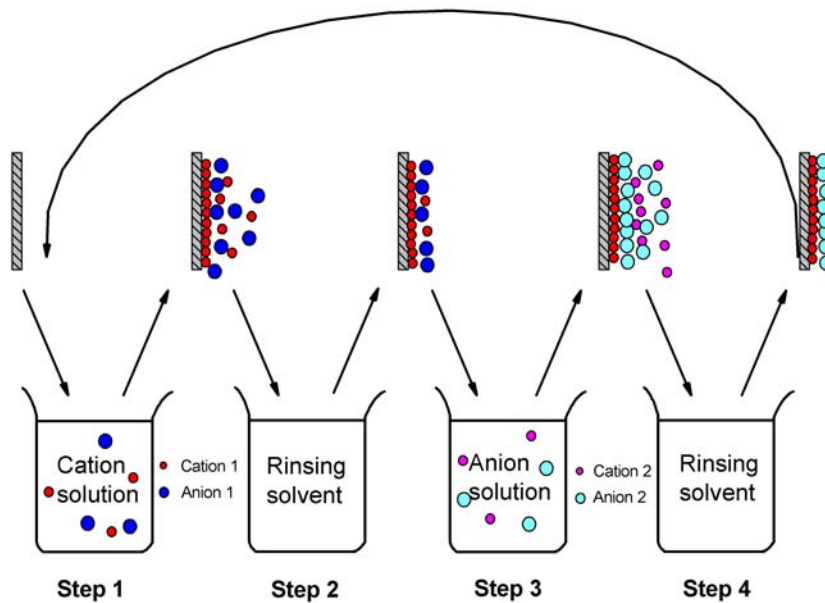


**Figure 10.** Schematics of a common SILAR dip coating procedure.

In a recent MS thesis research project completed in our group, Arcot developed a modified SILAR method to increase the growth rates of oxide films<sup>90</sup>. In his procedure, rinsing steps are omitted. Arcot have showed that this method is promising for making thicker and uniform oxide films. For example, Y<sub>2</sub>O<sub>3</sub> (10%) doped ZrO<sub>2</sub> films were prepared with a growth rate of ~ 8.8 nm/cycle. We refer this as Method A.

In this dissertation research, we further investigated two methods to synthesize zirconia (ZrO<sub>2</sub>) films, in order to find the most appropriate method to deposit the ZrO<sub>2</sub> films in ZrO<sub>2</sub>-clay multilayers. One is a modification of the common SILAR method, where only one rinsing step is applied (after immersion in the anionic precursor solution). This method is referred as Method B. The other is a sol-gel dip coating method, which is referred as Method C. Our study showed that Method C achieved the best results, and it was therefore integrated into the optimized procedures to make ZrO<sub>2</sub>-clay multilayers as described in Chapter 5.

We also investigated methods to synthesize ceria (CeO<sub>2</sub>) films and obtained fair results. Results are reported in Appendix A, and this part of work is not described in great details because the subsequent effort in making CeO<sub>2</sub>-clay multilayers is largely unsuccessful.

## **2. Experiments**

Silicon substrates were cleaned by an alkali cleaning procedure. They were etched in a 0.1 M NaOH solution for 20 minutes, neutralized in a 1 M HCl solution for 5

minutes, ultrasonically cleaned in distilled water for 20 minutes, and dried in air for around 20 minutes.

A computer controlled NIMA DC-*multi* dip coater with an 8-beaker carousel was used to synthesize oxide films. In our modified SILAR method (Method B), the substrate was alternatively immersed into a cationic solution (0.1 M Zirconium chloride), an anionic solution (1N NH<sub>4</sub>OH), and deionized water. Zirconium chloride solutions were prepared by dissolving 2.416 g zirconyl (IV) chloride octahydrate ( $ZrOCl_2 \cdot 8H_2O$ ) in 75 ml deionized water. The dipping speeds (up or down; 1 to 60 mm/min), holding times (in solutions and air), immersing and withdrawing positions (10-65mm), and number of cycles are the control parameters.

In the sol-gel dip coating (Method C), substrates were dipped in a 0.3 M zirconium acetate solution and deionized water repeatedly. Zirconium acetate solutions were prepared by dissolving 5 g zirconium acetate hydroxide ( $Zr(OH)_x(OAc)_y, x + y = 4$ ) in 75 ml deionized water. Dip coating parameters were: dipping speed (up or down) = 20 mm per minute, holding time (in solutions and air) = 45 seconds, and deposition cycles = 10-30. The dipping process was also conducted via using the NIMA DC-*multi* dip coater.

The as-deposited amorphous and hydrated films were thermally annealed to obtain pure oxide films. The morphology, composition and crystalline of oxide films were characterized by field-emission scanning electron microscopy (FE-SEM), in conjunction with an energy dispersive X-ray (EDX) analyzer, and X-ray diffraction (XRD).

### 3. Results and Discussions

Figure 11 (a) shows a representative cross-sectional image of a  $\text{ZrO}_2$  film prepared using Method B with the following parameters: dipping speed = 20 mm per minute, holding time = 10 seconds, annealing temperature = 600 °C, annealing time = 2 hours, and deposition cycles = 10. This  $\text{ZrO}_2$  film was ~ 50-nm thick. Correspondingly, the growth rate was calculated to be 5 nm per cycle. The film uniformity and growth rate did not change significantly when the dipping speed was decreased from 20 to 10 mm per minute (Figure 11 (b)) or when the holding time was changed from 10 to 45 seconds.

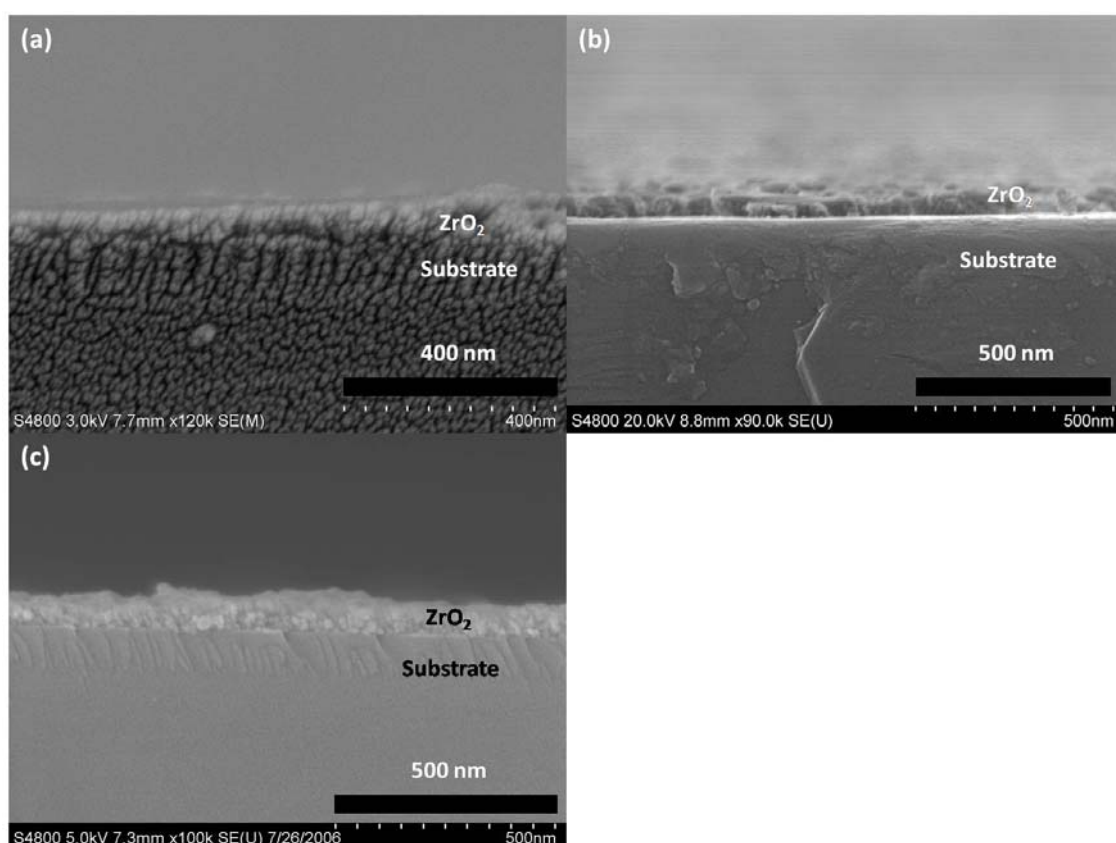


**Figure 11.** The cross-sectional SEM images of zirconia films made using Method B (with one rinsing step) and following parameters: dipping speed = (a) 20 mm/min or (b)

10 mm/min, holding time = 10 sec, and number of deposition cycles = 10. As a comparison, a cross-sectional SEM image made using Method A (without rinsing steps; 20 mm/min dipping speed; 10 sec holding; 20 deposition cycles) is shown in (c). All specimens were annealed at 600 °C for 2 hours.

We compared the zirconia films synthesized by Method B (Figure 11 (a) and (b)) with those synthesized by Method A (i.e., Acrot's method with no rinsing steps<sup>90</sup>, (Figure 11 (c)). Method B (our modified method with one rinsing per deposition cycle) did not achieve better results than Method A; the film quality appears to be similar in cross-sectional SEM images. Furthermore, annealed zirconia films made by Method B showed submicron-meter-scale pores and cracks from the in-plane views (Figure 12(a)). Small pores (with diameters of ~ 50 nm) were also found in as-deposited films made by Method B (Figure 12(b)), and it is likely that they grew during annealing. Thus, Method B is not ideal.

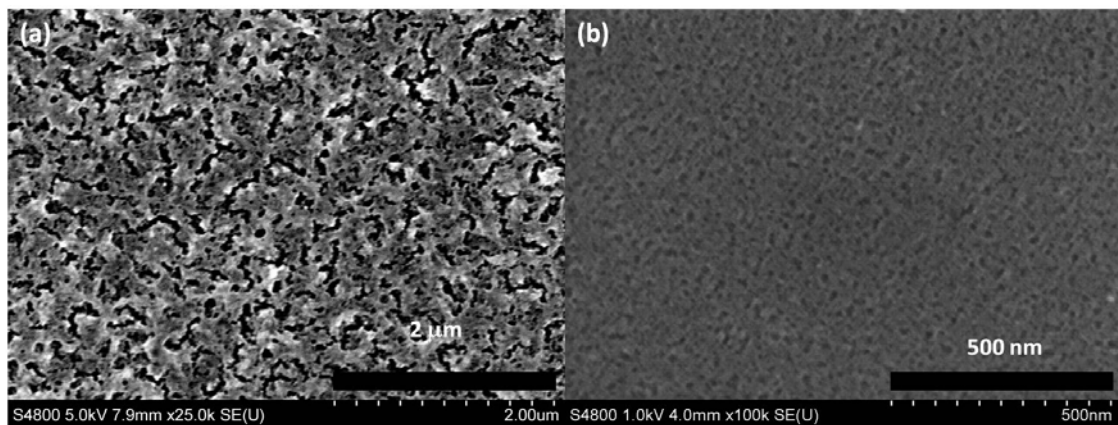
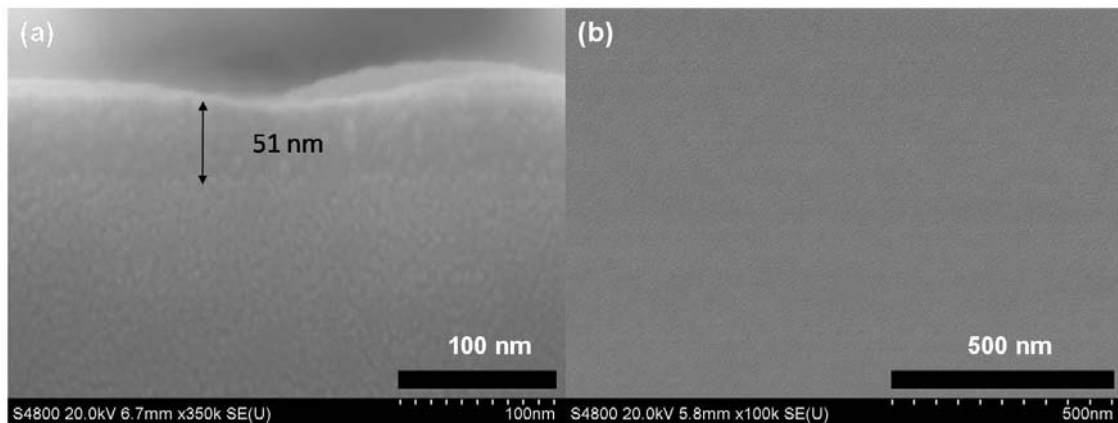


**Figure 12.** In-plane views of (a) our annealed and (b) as-deposited zirconia films made by Method B.



(c)

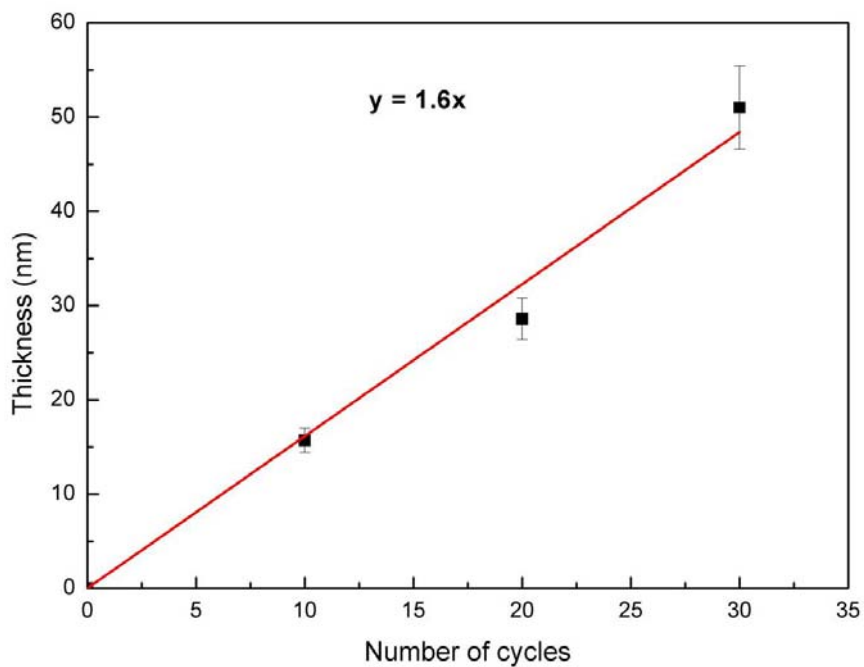


**Figure 13.** (a) Cross-sectional and (b) in-plane views of a representative as-deposited zirconia film made by a sol-gel dip coating method (Method C; 30 deposition cycles). (c) The thickness of as-deposited zirconia films vs. the number of deposition cycles.



Furthermore, we prepared as-deposited zirconia films using a sol-gel dip coating method (Method C) described above. The deposited films were uniform and pore-free, as shown by both cross-sectional and in-plane SEM images in Figure 13. The film grew linearly. The estimated growth rate was about  $\sim 1.6$  nm per cycle, as shown in Figure 13 (c). The value is similar to the reported size of zirconium polycations ( $\sim 2$  nm<sup>94</sup>). This result suggested that about one monolayer of zirconia polycations was deposited on the substrate per deposition cycle. This monolayer growth rate is similar to a typical SILAR process. This recipe for the preparation of zirconia films was incorporated into our optimized method for synthesis of ZrO<sub>2</sub>-clay multilayers in Chapter 5, and the results reported in Chapter 5 further showed that the growth rate was significantly increased when we deposited the sol-gel films on the surfaces of clays.

CHAPTER FOUR  
A FEASIBILITY STUDY OF SYNTHESIS OF NANOCCLAY-ZIRCONIA  
MULTILAYERS

Adapted from:  
H. Chen, G. Zhang, K. Richardson, and J. Luo  
“Synthesis of Nanostructured Nanoclay-Zirconia Multilayers: a Feasibility Study”  
*Journal of Nanomaterials*, **2008**, 749508 (2008)

### **1. Introduction**

The last decade has seen tremendous developments in the “wet” colloid chemical synthesis of nanosized or nanostructured materials, which was inspired by “biomineralization and hierarchically organized self-assembly”<sup>15</sup>. This wet synthesis technique utilizes alternating layer-by-layer deposition process, which is enhanced by electrostatic assembling or surface mediated adsorption and reaction. It has several major advantages, such as relative ease of preparation, low cost, and high versatility. Through this technique, a variety of nanostructured materials with much improved properties or enhanced functionalities have been developed, including inorganic<sup>95, 96</sup> or hybrid organic-inorganic<sup>10</sup> films. In particular, inspired by the special mortar-brick micro/nano structure of nacre and its superior mechanical properties, hybrid multilayers consisting of alternating organic polymer and inorganic nanoclay layers have been made by a layer-by-layer (LBL) deposition/assembly method<sup>9, 97</sup>. This method was modified from a more general method for making polyelectrolyte multilayers where substrates are alternately dipped into polycation and polyanion solutions to form polyelectrolyte thin films<sup>17</sup>.

A key underlying mechanism in the wet chemical construction of nanomaterials is the solution-based self-assembly aided by electrostatic attraction force between oppositely charged components (e.g., ions, polyions). The use of platy shaped clay nanoplatelets with intrinsic, permanent negative surface charges in constructing nanostructured multilayers is an innovation to extend the capabilities of the conventional ion/polyion aided self-assembly techniques. To date, hybrid inorganic clay and organic polymer (including biopolymer and protein) nanostructured multilayers have been developed<sup>37</sup>, but progress in making inorganic nanoclay-based nanocomposites or multilayers has not been reported. Due to the inherent thermal and chemical instability of organic polymers, hybrid organic and inorganic multilayers have limitations in many specialized applications, such as high-temperature environments. Therefore, we conducted the research to develop inorganic oxide-clay nanostructured multilayers.

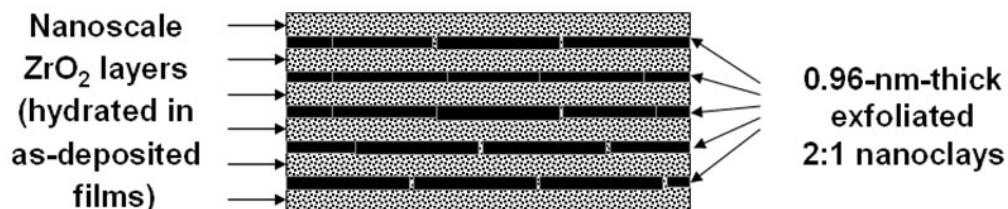


**Figure 14.** A targeted multilayer structure to synthesize in this study using a new LBL assembling technique via making use of the intrinsic negative surface charges and unique platy shape of nanoclays. In principle, the thickness and chemical composition of each nanometer-thick oxide layer can be tuned individually, offering versatility in engineering these nanostructured films with a wide range of potential applications to be explored in future studies.

This chapter describes our first feasibility study of making hydrated inorganic oxide-clay nanostructured multilayers. The goal of this study is to develop a purely inorganic, perfectly nanostructured nanoclay-oxide multilayers (Figure 14).

## **2. Experimental**

### **2.1 Materials**

Epi-polished silicon wafers with thermally oxidized surface layers (Si/SiO<sub>2</sub>) were purchased and cut into pieces of 1×2 cm<sup>2</sup> to be used as substrate. The Si/SiO<sub>2</sub> wafers were ultrasonically cleaned in 0.1 M NaOH solution for 20 minutes, immersed into piranha solution (3 vol. of 95-98 wt. % H<sub>2</sub>SO<sub>4</sub> : 1 vol. of 30 wt. % H<sub>2</sub>O<sub>2</sub>) for 20 minutes, rinsed with deionized water 4 times and dried in air. A Na-montmorillonite (MMT) clay (Cloisite® Na<sup>+</sup>) was purchased from Southern Clay Products (Gonzales, TX). The 0.15 wt. % clay solution (pH = 7.24) was prepared by stirring clays with magnet in deionized water at 1000 rpm speed for 20 minutes and then ultrasonicated for 20 minutes to achieve complete dispersion and exfoliation. All other chemicals were purchased from Sigma (Sigma-Aldrich, St. Louis, MO). Two different zirconium cationic precursor solutions were examined, including 0.1 M zirconium chloride (pH = 1.32) prepared from zirconium (IV) oxychloride octahydrate and zirconium acetate (pH = 4.14) prepared from zirconium (IV) acetate hydroxide. Sodium poly(styrenesulfonate) (PSS) and poly(ethyleneimine) (PEI) were dissolved in deionized water at concentrations of 1.5 mg/ml.

## ***2.2 Wet chemical synthesis and annealing***

Two steps were involved in the synthesis of the oxide-clay multilayers: (1) wet chemical construction of multilayer precursors, and (2) dehydration and thermal annealing at elevated temperatures. This preliminary study particularly focused on demonstrating the feasibility of the first step which is more critical for developing the targeted clay-oxide multilayers. Thus the dehydration and thermal annealing conditions were pre-selected as a rule of thumb to be 600°C in air for 2 hours under 1 atmospheric pressure, since most montmorillonites can keep its crystal structure (i.e., no dehydroxylation) at temperatures of 600-650°C. However, the control parameters of thermal annealing or hydrothermal treatment (i.e., the second step of synthesis) will be optimized in future study.

A computer-controlled programmable Nima dip coater (Nima Technology Ltd., Coventry, England) was used to synthesis nanostructured multilayers. To verify the layer-by-layer deposition method, nanoclay-polymer films were prepared following the recipe in Lvov's work<sup>36</sup>. The Si/SiO<sub>2</sub> substrates were pretreated by dipping into PSS, PEI, and PSS solutions each for 20 minutes. The pretreated substrates were then dipped into a clay solution for 20 minutes, rinsing with water for 2 minutes, dipping into a PEI solution for 20 minutes, and rinsing again with water for 2 minutes to complete one complete deposition cycle. This four-step deposition cycle was repeated 8 times to make nanoclay-polymer multilayers [(PEI/PSS/PEI)-(MMT/PEI)<sub>8</sub>]. Both the dipping and the withdrawing speeds were controlled at 20 mm per minute.

To prepare nanoclay-oxide multilayers, the pre-cleaned silicon substrates were dipped into a zirconium cationic precursor solution (zirconium chloride or zirconium acetate) and the exfoliated nanoclay suspension alternately without inter-dipping rinsing. The deposition cycle was repeated 15 to 30 times to prepare the as-deposited multilayers. Both the dipping and withdrawing speeds were controlled at 20 mm per minute. The holding time was kept 45 seconds in air, the zirconium cationic precursor solution, and clay suspension. The as-deposited films were annealed isothermally to 600°C for 2 hours at constant heating and cooling rates of 5°C per minute.

### ***2.3 Characterization***

Both as-deposited (i.e., air-dried specimens) and annealed films were characterized by a field-emission scanning electron microscope (FE-SEM, Hitachi S4800) equipped with energy dispersive X-ray spectroscopy (EDXS) analyzer. SEM specimens were coated with Pt/Au for increased conductivity. In addition, a variable-pressure SEM (Hitachi, S3500) was employed to examine specimens without coatings. Both in-plane and cross-sectional images were taken. Cross-sectional specimens were made by carefully cleaving Si wafers, while protecting the surface of films with soft filter papers. Film thickness was measured on multiple points on specimens using cross-sectional SEM images. EDXS was performed directly on the selected spots of the films to analyze both qualitatively and quantitatively the elemental composition of the multilayers.

X-ray diffraction (XRD) using a Scintag diffractometer (Cu- $K_{\alpha}$  radiation,  $\lambda = 1.5418 \text{ \AA}$ , operating at 40 kV and 35 A) was carried out on both as-deposited films and annealed specimens. In addition, the bare Si/SiO<sub>2</sub> substrate was also scanned by XRD to examine any potential influence of the substrate on the observed diffraction patterns of the ultrathin multilayers.

### **3. Results and Discussion**

#### ***3.1 Clay-polymer multilayers***

The surface and cross-sectional SEM images of the as-deposited nanoclay-polymer [(PEI/PSS/PEI)-(MMT/PEI)<sub>8</sub>] multilayers are shown in Figure 15. Some unevenly-piled MMT platelets can be seen in Figure 15a. The cross-sectional SEM image (Figure 15b) shows layered nacre-like structure similar to that observed in the films developed by Tang et al.<sup>9</sup>. The measured thickness is  $40 \pm 9 \text{ nm}$ , including 10 nm thick precursor polymer film<sup>36</sup>. Thus the thickness of a single MMT/PEI layer formed through a complete deposition cycle is approximately  $\sim 3.75 \text{ nm}$ , which is consistent with the previously reported value of 3.3 nm per deposition cycle<sup>36</sup>. It was postulated that the highly-branched polycation PEI works as ‘electrostatic glue’<sup>36</sup> to assemble clay platelets. In conclusion, polymer-nanoclay multilayers were reproduced in our laboratory with similar nanostructure. This verified our equipment and procedures and enabled further exploration of synthesizing the new nanoclay-oxide multilayers.

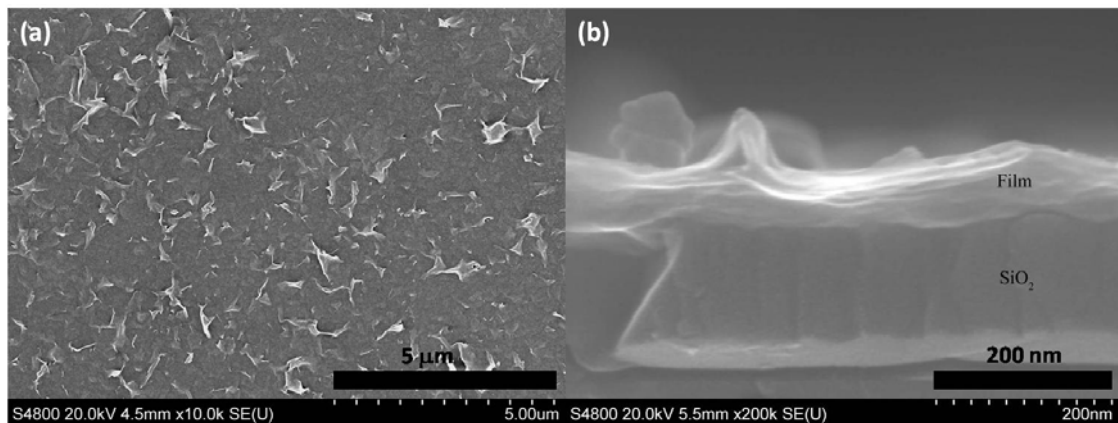


**Figure 15.** Surface (a) and cross-sectional (b) images of as-deposited nanoclay-polymer [(PEI/PSS/PEI)-(nanoclay/PEI)<sub>8</sub>] films.

### 3.2. Clay-zirconia multilayers

The SEM images of as-deposited multilayer films prepared by zirconium chloride and zirconium acetate cationic precursor solutions are shown in Figure 16 and Figure 17, respectively. The as-deposited films were dried in air, thus either nanoclays or hydrated zirconium cations are not completely dehydrated. Both films appear to be reasonably uniform and crack-free. Furthermore, they both exhibit clear layered structures in cross-sectional SEM images (Figure 16 (b) and Figure 17(b)).



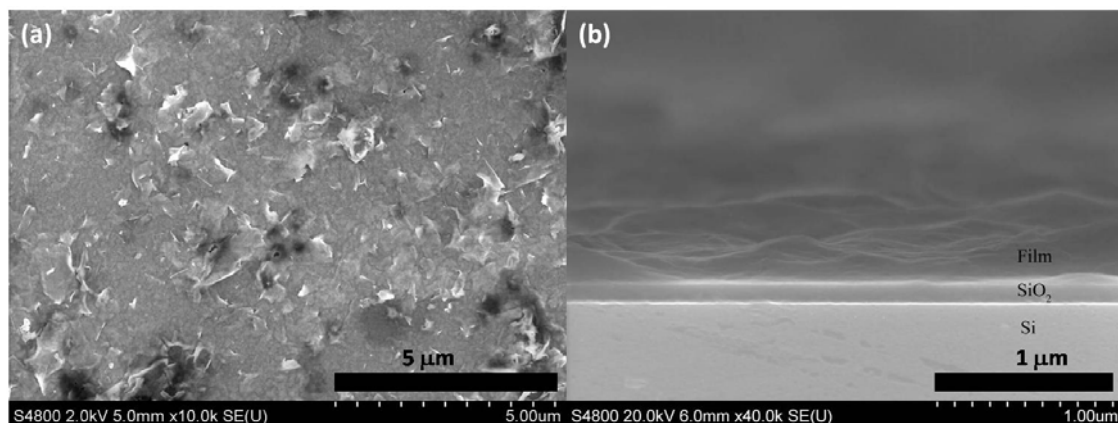


**Figure 16.** (a) Surface and (b) cross-sectional SEM images of as-deposited hydrated nanoclay-zirconia multilayers made via zirconium chloride cationic solution.

Evidently, the films made by zirconium acetate cationic precursor solutions have significantly smoother surface and more regular (parallel) layered structures (Figure 16 vs. Figure 17). The clay nanoplatelets are better oriented in the films prepared by zirconium acetate cationic solutions than those prepared by zirconium chloride precursor solutions. Peel-up edges and overlapping of clay platelets are frequently seen in the zirconium chloride prepared films (Figure 16a). For films prepared by zirconium chloride precursor solutions, the layered structures are less close-packed with occasional open voids (Figure 16b). The nanoclay/hydroxide multilayers prepared using zirconium acetate precursor solutions (Figure 17) also appear to have lower surface roughness than those polymer-nanoclay multilayers prepared in this (Figure 15) and prior<sup>36</sup> studies. Based on these results, zirconium acetate cationic precursor solutions are used exclusively to make multilayers in further studies.

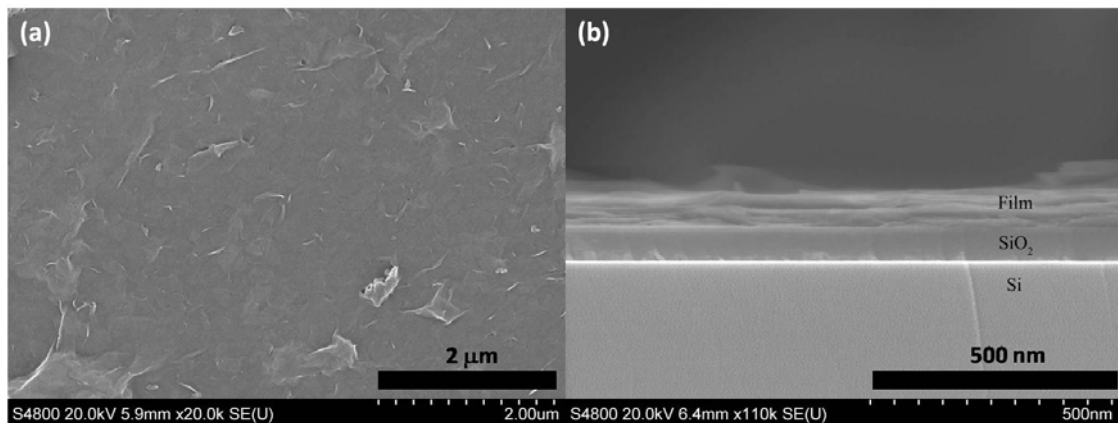


**Figure 17.** (a) Surface and (b) cross-sectional SEM images of as-deposited hydrated nanoclay-zirconia multilayers made by zirconium acetate cationic solutions.

Surface and cross-sectional SEM images of annealed films are shown in Figure 18. The annealed films appear to be denser and more uniform while some indications of layering structures can still be seen in the cross-sectional SEM images (Figure 18 (a) and 5(b)). It should be noted that the observed cross-sectional surfaces were influenced by the actual (somewhat random) cleaving process and hence the layered structure is not always clearly visible. The surfaces of annealed films (Figure 18 (c)) are also smoother than those of as-deposited films (Figure 17 (a)); yet, some nanoclay platelets can still be seen (Figure 18 (c)).

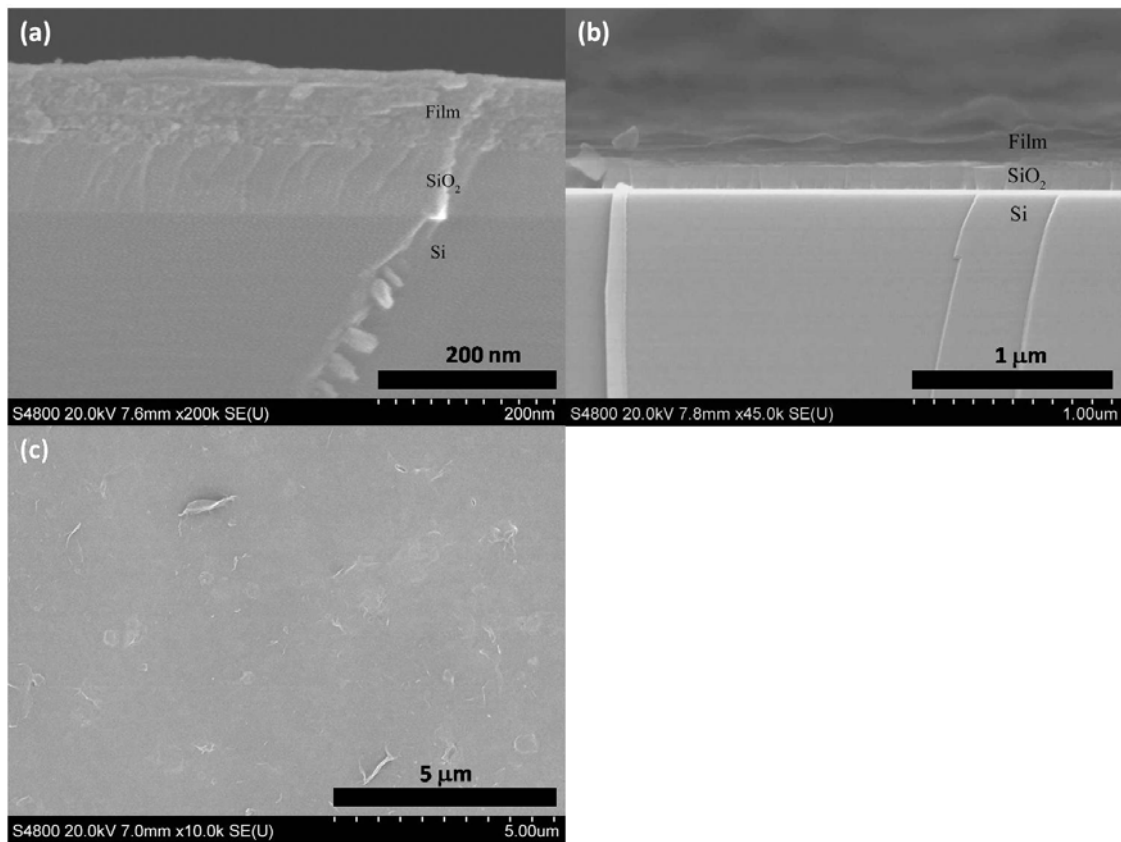


**Figure 18.** (a) and (b) cross-sectional and (c) surface SEM images of annealed nanoclay-zirconia films made by zirconium acetate precursor solutions (using 25 deposition cycles).

EDXS analysis of as-deposited and annealed films found Al, Si, Zr but no other metal impurities. A representative EDXS spectrum is shown in Figure 19. Quantitative elemental analysis was attempted with results shown in Table 5. We believe that the excess amounts of Si and O measured by EDXS are from the Si/SiO<sub>2</sub> substrates. Since the films are very thin (~ 100 nm) and the interaction distance for an electron beam in a non-metallic material is usually about 1 μm, the beam must be smeared. Although the

quantitative compositional measurements are probably not accurate due to the beam spreading effect, it can be concluded that these films consist of oxides (or hydroxides) of Al, Si and Zr without significant impurities of other elements.

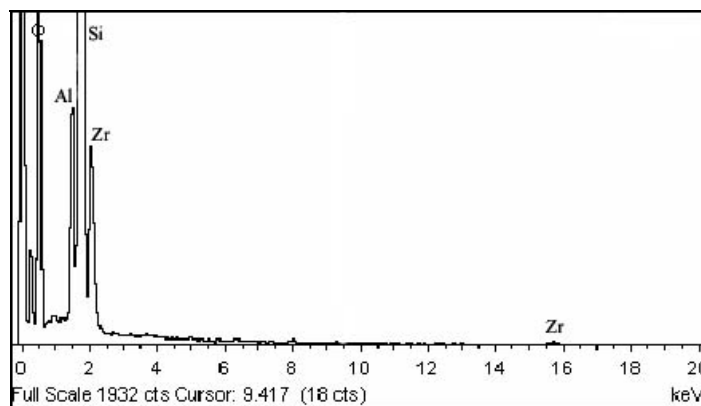


**Figure 19.** A representative EDXS spectrum for an annealed film.

**Table 5.** EDXS compositional analysis. Each data point is an average of three measurements. The measured excess amounts of Si and O are from Si/SiO<sub>2</sub> substrates (artifacts) due to spread of electron beams and do not represent actual film composition.

Element	Atomic %	
	As-deposited	Annealed
O	61.7	35.3
Al	3.6	1.2
Si	30.6	59.9
Zr	4	3.6

XRD patterns of as-deposited and annealed multilayers are shown in Figure 20, in which  $d$ -spacings are labeled for all peaks. As-deposited films appear to be largely amorphous, but a series of low angle peaks were observed. The 1.2 nm peak should result from hydrated clays. The presence of this peak indicates that some multiple layers of clay nanoplatelets are absorbed in dipping (unflavored). The 5.7 nm peak represents the periodic thickness formed by each deposition cycle for the multilayers without annealing. The origin of the 2.3 nm peak is currently unclear and worth further investigation. It is noteworthy that the 1.2 nm peak is the sharpest of all peaks (Figure 20 (a)). Given the low crystallinity of clay minerals, all other broad peaks suggest that the as-deposited multilayers possess much less ordered atomic structure or crystallinity, which should be expected. Nevertheless, a good layered nanostructure is clearly present in the as-deposited film with a periodic thickness of  $\sim 5.7$  nm (Figure 20), indicating the success of the LBL deposition.

For annealed specimens (Figure 20 (b)), only two peaks are observed. A broad, weak peak at 1.6 nm is probably caused by the (002) reflection of the periodic thickness of 3.2 nm (see §3.3). The shape of the peak also indicates that the periodicity of the layers is not perfect, which is probably caused by the crystallization process during annealing. The low angle scan did not find the (001) reflection at 3.2 nm, and the reason is unclear at present. The second peak at  $d = 0.3$  nm matches  $\text{ZrO}_2$  (111) reflection, indicating the formation of nanocrystalline  $\text{ZrO}_2$ . The mean grain size of the nanocrystalline  $\text{ZrO}_2$  was estimated to be  $\sim 9.7$  nm based on the peak width. Given that periodic thickness in the annealed film is approximately 3.2 nm (See §3.3), the  $\text{ZrO}_2$

crystallite size of 9.7 nm indicates that the growth of nanocrystals may start to break the parallel multilayer structure (by colliding into nanoclay platelets which should act as barrier between two adjacent of oxide layers), which is consistent with weak/absence of low-angle reflections from the annealed multilayer structures. Nonetheless, the existence of some layered structures is evident by cross-sectional SEM (Figure 18 (b) and (c)), but the layered structures are probably less regular, presumably due to the growth of ZrO<sub>2</sub> nano crystals. It is noted that a bump due to Si/SiO<sub>2</sub> substrates were sometimes observed around 30° (the intensity of which varies with the specific experimental conditions)<sup>98</sup>,<sup>99</sup> and this is also seen in the XRD pattern of the as-deposited specimen (with lower intensity, although these two measurements were made with the exactly the same conditions). Thus, we cannot exclude the possibility that this peak is an artifact from the substrate.

It is generally expected that montmorillonites are chemically stable for annealing at 600 °C<sup>100</sup>. More annealing experiments will be conducted to investigate how nanoclays react with Zr complexes during high temperatures, which will help form high temperature endurable nanoclay-oxide multilayers.

It is worth emphasizing that the annealed films still remained certain layered structure after cutting and no significant cracking or delaminating was observed (Figure 18), in spite of up to 50% linear shrinkage occurred during annealing, as discussed later (§3.4).

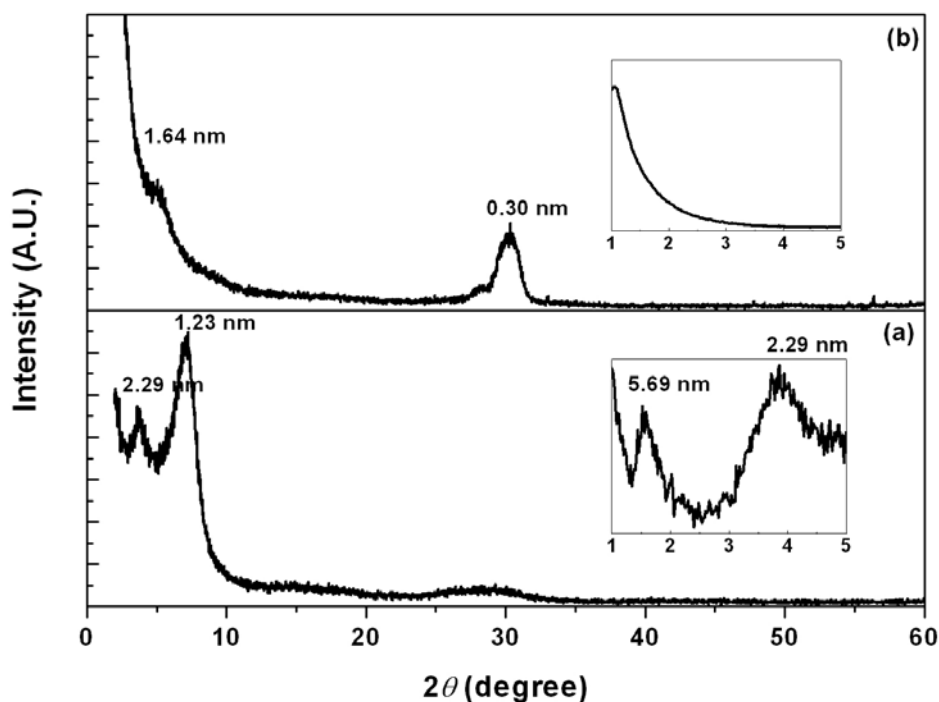
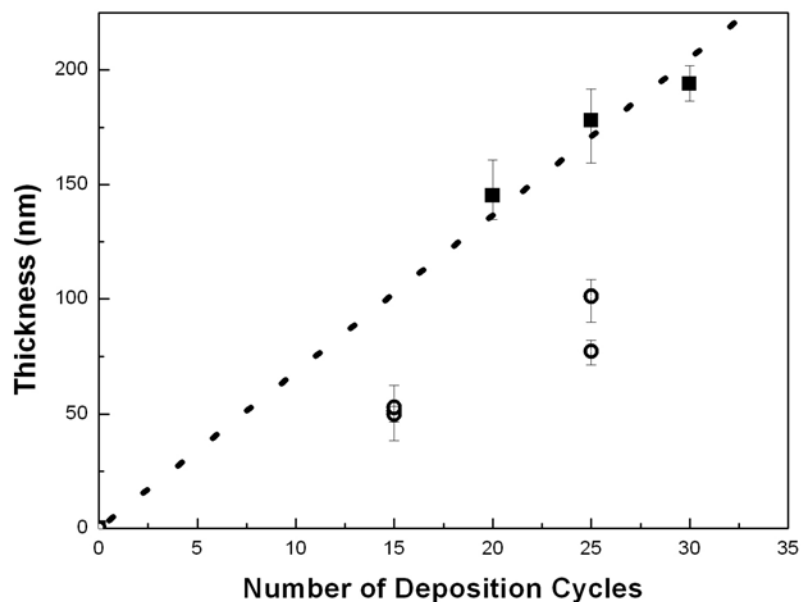


**Figure 20.** XRD patterns of (a) annealed and (b) as-deposited films (20 layers) made by zirconium acetate cationic solutions. The two XRD experiments are carried out with the same conditions (scan rate and slit size) and the patterns are shown in the same intensity scale. The insets are additional scans at low angles with a smaller slit (shown in different intensity scales).

### 3.3 Film growth rate through LBL deposition

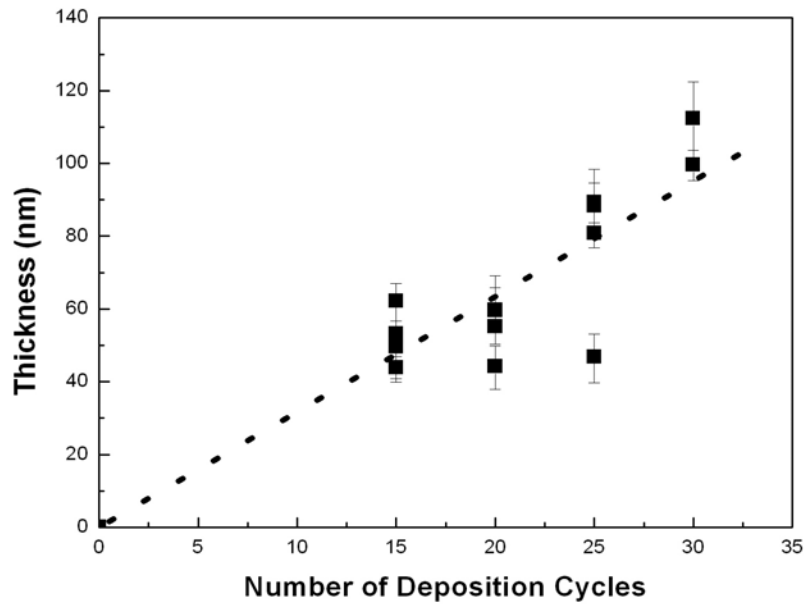
The thickness versus number of deposition cycles of as-deposited and annealed films prepared by zirconium acetate cationic precursor solutions are shown in Figure 21 (a) and (b), respectively. As-deposited multilayers are expected to exhibit low cohesion between layers, part of the multilayers may fall off during fracture; we suspect that this is responsible for the measured abnormal (lower) thickness values for the three data in

Figure 21(a) (represented by open circles). If these data are excluded, the measured film thickness for both as-deposited and annealed films increase monotonically with the number of the cycles. The growth rates of as-deposited and annealed specimens are  $\sim 6.8$  nm per cycle and  $\sim 3.2$  nm per cycle, respectively. In other words, linear shrinkage in film thickness is  $\sim 50\%$  upon annealing at  $600^\circ\text{C}$  for 2 hours, which is about the same as previously observed for pure  $\text{ZrO}_2$  films<sup>98,99</sup>. This shrinkage also indicates dehydration and sintering have occurred during annealing. The multilayer period was measured as  $\sim 5.7$  nm by XRD (Figure 20; §3.3), which should be more accurate than the SEM measurement; the agreement between XRD and SEM measurements (5.7 nm vs. 6.8 nm) is rather satisfactory, given the difficulties in obtaining accurate nanometer range measurements under SEM.



(a)





(b)

**Figure 21.** Thickness versus number of deposition cycles for as-deposited (a) and annealed (b) films made by zirconium acetate precursor solutions. In (a), it is assumed that open circles represent measurement artifacts (as-deposited films where the part of layered films peeled off during cleaving of the specimens). Errors bars represent the data range. Lines represent the best linear fits.

#### 4. Conclusions

A novel layer-by-layer deposition method has been developed for manufacturing nanoclay-zirconia multilayers by sequentially dipping a substrate in an exfoliated nanoclay suspension and a zirconia cationic precursor solution followed by annealing at 600°C. Nanoscale layer-by-layer growth is evident by the measured film growth rate per deposition cycle as well as direct observation in cross-sectional SEM and X-ray diffraction patterns. It is found that zirconium acetate is a better cationic precursor

solution for growing more uniform films. The growth rate of as-deposited specimens is  $\sim 5.7$  nm per cycle; the growth rate can be further tuned by changing the deposition parameters. Denser dehydrated films form after annealing at  $600^{\circ}\text{C}$  for two hours in air and film thickness shrinks by  $\sim 50\%$ ; yet, the annealed films remain uniform and crack-free, and exhibit some nanoscale layering (although less clearly observable under SEM). In summary, the feasibility of the new LBL deposition technique has been clearly demonstrated, but the post-deposition dehydration and annealing should be further optimized.

## **5. Issues and Further Studies**

While the above preliminary results are promising, the combined XRD, SEM and EDXS characterization indicates that the multilayers made in this study are not yet perfect (with deviations from the targeted nanostructure shown in Figure 14). First, the 1.2 nm peak in XRD patterns (Figure 20 (b)) indicates that nanoclays are not completely exfoliated into single 2:1 layers and multiple layers of clay nanoplatelets are deposited within the films. This can be further improved by fine tuning the clay suspension chemistry and dipping process. Second, while as-deposited films exhibit fairly good layered structure, the thermally annealed films appear to possess relatively poor periodicity, as evident by both SEM and XRD. Annealing at  $600^{\circ}\text{C}$  for 2 hours in air was the only dehydration process that has been tested so far (since this study focused more on the feasibility of the LBL deposition). Further optimization of the annealing procedure will be conducted to identify an optimal conditions based on a trade-off between

dehydration and the structure integrity. Hydrothermal annealing<sup>93</sup> may be an alternative method to dehydrate/crystallize the oxides while maintaining the stability of clays and multilayered structure.

Nonetheless, this study has clearly demonstrated the basic feasibility of this new LBL technique for making this new class of nanostructured nanoclay-oxide multilayers and further research should be conducted to tune thickness and composition of each individual oxide layers (including materials other than  $ZrO_2$ ) by changing the deposition parameters and precursor solutions, which will offer tremendous versatility for making a variety of nanostructured films with diverse functionalities and applications.

## CHAPTER FIVE

### GROWTH MECHANISMS OF NANOCLAY-ZIRCONIA MULTILAYERS

Adapted from:

H. Chen, G. Zhang, Z. Wei, M. Cooke, and J. Luo

“Layer-by-Layer Assembly of Sol-Gel Oxide “Glued” Montmorillonite-Zirconia Multilayers”

*Journal of Materials Chemistry*, in press

#### 1. Introduction

The previous chapter describes a preliminary study that proved the basic feasibility of synthesis of a new type of all-inorganic  $\{\text{MMT}_x\text{-(sol-gel ZrO}_2)\}_n$  multilayers by combining the LbL electrostatic assembly technique with a surface sol-gel method<sup>98,99</sup>. A Processing optimization study has then been conducted to achieve much improved layered structures and to demonstrate the capability to finely tune the periodic, nanoscale layer thickness. The details of this optimization study are documented in Appendix B.

This chapter describes and discusses a systematical study of the film growth kinetics controlling the sol-gel  $\text{ZrO}_2$  layer deposition on the MMT surfaces, which elucidates the important role of electrostatic attraction in film growth. Specific findings include:

- 1) the growth rates of the sol-gel  $\text{ZrO}_2$  layers are significantly enhanced on the MMT surface;

- 2) the intermediate-stage growth rates of the sol-gel ZrO<sub>2</sub> layers on the MMT surface are greater than those estimated by either mass transfer or interfacial reaction controlled kinetic models; and
- 3) the growth of sol-gel ZrO<sub>2</sub> layers on the MMT surface is self-limited to a maximum thickness.

These observations are attributed to the surface controlled sol-gel growth that is likely influenced or controlled by electrostatic attractions.

Although the mechanisms of the electrostatic assembly are important and have been extensively investigated<sup>4, 15-23, 37, 101-103</sup>, quantitative studies are generally difficult. This is largely caused by the use of polyelectrolytes in the synthesis of those LbL films, which results in so-called “fuzzy multilayers”<sup>101</sup>. Thus, this study of the film growth kinetics, via synthesizing the {MMT<sub>x</sub>-(sol-gel ZrO<sub>2</sub>)}<sub>n</sub> multilayers, provides a different perspective to the quantitative understanding of the film growth kinetics. The findings improve our understanding of the LbL assembly process in its general sense.

The results reported in this chapter have paved the way towards the further development of generic LbL methods to synthesize new, all-inorganic {nanosheet-(sol-gel oxide)}<sub>n</sub> and {nanoparticle-(sol-gel oxide)}<sub>n</sub> multilayers with potential applications such as high-temperature gas membranes and sensors, among others. Specifically, the LbL assembly of nanostructured multilayers using sol-gel oxides, instead of polyelectrolytes, as “glues” in the structure, represents an innovative concept of nanoscale fabrication.

## 2. Experimental

Surface polished p-type single-crystal silicon wafers (MEMC Electronic Materials, Inc., St. Peters, MO) were used as substrates for LbL deposition. The wafer surface has a layer of thermally oxidized SiO<sub>2</sub> of 100 nm in thickness, which serves as an inert diffusion barrier. A sodium montmorillonite (MMT) clay, Cloisite® Na<sup>+</sup>, with a cation exchange capacity of 92 meq per 100 g was purchased from Southern Clay Products, Inc. (Gonzales, TX). A zirconium (IV) acetate hydroxide ((CH<sub>3</sub>COO)<sub>x</sub>Zr(OH)<sub>y</sub>,  $x + y = 4$ ; 40 wt.% zirconium or  $x \approx 1.5$ ) powder was purchased from Sigma-Aldrich, Inc. (St. Louis, MO). The MMT and zirconium acetate hydroxide were the two major constituents used for multilayer synthesis.

Small pieces of silicon wafers (with an approximate size of  $1 \times 2 \text{ cm}^2$ ) were ultrasonically cleaned in 0.1 M NaOH solutions for 20 minutes, immersed into piranha solutions (3 vol. of 95-98 wt.% H<sub>2</sub>SO<sub>4</sub> : 1 vol. of 30 wt.% H<sub>2</sub>O<sub>2</sub>) for 20 minutes, then rinsed with deionized water four times and dried in air. Different from our prior preliminary work,<sup>104</sup> this study adopted an improved method to prepare nominally 0.5 wt.% exfoliated clay suspensions by following the recipe of Podsiadlo *et al.*<sup>10</sup>, in which the sodium MMT suspensions were first vigorously stirred for a week and then settled for 24 hours (to allow the coarser particles and impurities to settle) before supernatants were collected for subsequent LbL assembly. (The systematic investigations of cleaning procedures and exfoliation methods were reported in Appendix B.) This adoption for better exfoliated clay suspensions, along with the optimization of the sol-gel recipes and dipping processes, significantly improved the ordering of the layered structure and the

integrity of the resultant  $\{\text{MMT}_x\text{-(sol-gel ZrO}_2)\}_n$  multilayers. Aqueous sol-gel  $\text{ZrO}_2$  precursors were prepared by dissolving zirconium acetate hydroxide into deionized water along with 20 minutes ultrasonication. Then, the sol-gel  $\text{ZrO}_2$  precursor (which is interchangeably referred as “zirconium acetate hydroxide solution”, although the precursor is likely an aqueous polymeric “sol”) and the exfoliated MMT suspension were used for subsequent LbL electrostatic assembly.

A computer-controlled programmable dip coater (Nima Technology Ltd., Coventry, UK) was used to perform the LbL deposition. After an extensive parametric study, we selected an optimized synthesis protocol, which consists of four dipping steps: a pre-cleaned substrate was dipped into a precursor solution, a MMT suspension, and then deionized water twice. These four steps make up one deposition cycle. Most specimens were prepared with 30 deposition cycles, resulting in  $\{\text{MMT}\text{-(sol-gel ZrO}_2)\}_{30}$  multilayers. The substrate dipping and withdrawing speeds were kept at a fixed value of 20 mm per minute. The substrate was allowed to hold in air stagnatically between two adjacent dipping in the precursor solution and MMT suspension. This holding time was usually 45 seconds in air. Holding was also used in the precursor solution, MMT suspension, and deionized water. Holding durations of 45 seconds and 1 minute in the MMT suspension and water, respectively, were adopted, but the holding time in the precursor solution was varied from 0 to 10 minutes. Additionally, the precursor concentration varied from 0.03 to 0.4 M. For brevity, specimens were usually referred according to the precursor concentration and holding time in zirconium acetate hydroxide solution; other dipping parameters were usually kept unchanged (unless otherwise

specified) in this study. After completing the desired deposition cycles, all specimens were air dried and then characterized using the methods described below. Selected specimens were further annealed isothermally to preset temperatures (ranging from 200 to 600 °C) for 2 hours in air with a box furnace, using constant heating and cooling rates of 5 °C per minute.

The effect of precursor solution aging on the growth of sol-gel ZrO<sub>2</sub> layers was also examined. Fresh zirconium acetate hydroxide solutions with a concentration of 0.15 M were selected for ageing, with durations varying from 0 and 21 hours at 60 °C. Aged precursor solutions were then used for LbL assembly of multilayers by following the procedures described above.

Freestanding multilayers were prepared by adopting the procedure used by Mamedov and Kotov for making polyelectrolyte-nanoclay multilayers<sup>105</sup>. It involves a one-time extra step where the pre-cleaned substrate was first dipped into a 7.5 wt. % cellulose acetate solution, before the subsequent dips in other solutions and suspensions. To obtain freestanding films, the air-dried specimens were immersed in acetone to dissolve the cellulose acetate layer, allowing the separation between the desired multilayer and the substrate. As such, freestanding multilayers were obtained.

As-deposited (i.e., air-dried) and annealed multilayers were characterized by a field-emission scanning electron microscope (FE-SEM, Hitachi S4800). To examine the layered structure and measure the film thickness, cross-sectional surfaces of the specimens were obtained by cleaving the single crystal silicon substrates along the [100]

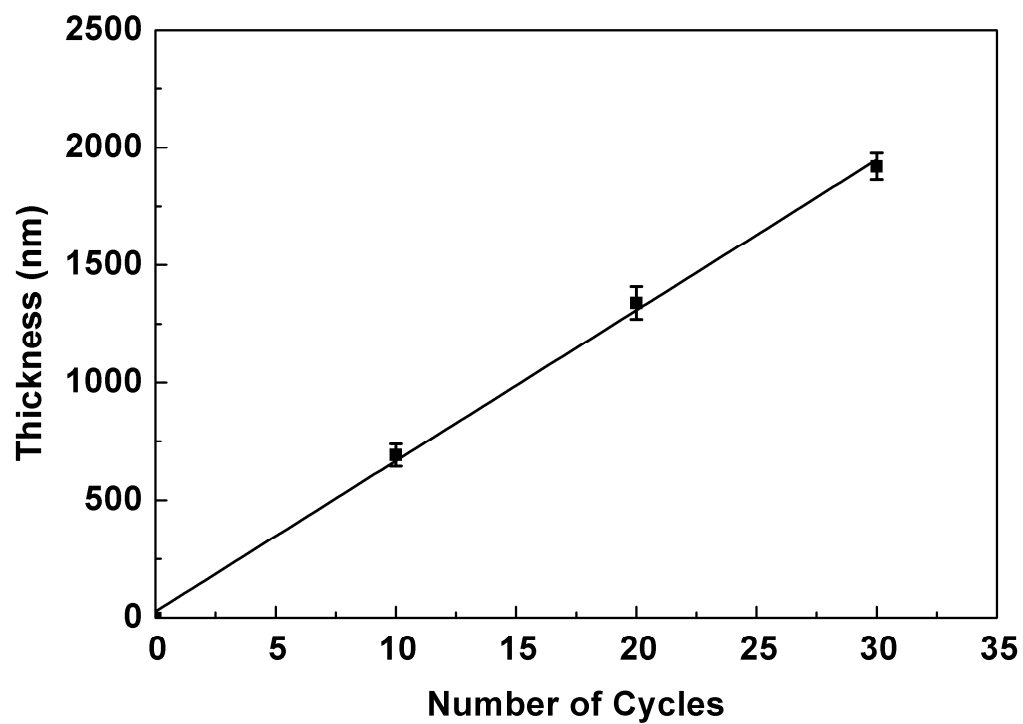


direction. Examined surfaces were all platinum-coated by a Hummer 6.2 sputtering system (Anatech, Union City, CA). Film thickness was measured at multiple locations and then averaged over at least five measurements. All thickness measurements were made in the specimens' central, horizontal cross-section surface, so that valid comparisons can be made to probe the growth kinetics of the sol-gel layers and the multilayer films. The error bars of thickness in all figures represent  $\pm 1.0$  standard deviation of these multiple measurements. The specimens were also characterized by X-ray diffraction (XRD), using a Scintag XDS 2000 diffractometer (Cupertino, CA) with a Cu- $K\alpha$  radiation ( $\lambda = 1.5418 \text{ \AA}$ ) and Fourier transform infrared spectrometer (FTIR, Thermo-Nicolet Magna 550, Madison, WI). The absorbance infrared spectra were obtained from 400 to 4000  $\text{cm}^{-1}$  with a resolution of 2  $\text{cm}^{-1}$ .

The hardness and elastic modulus of the specimens were determined by nanoindentation experiments using an MTS Nano Indenter XP (MTS Nano Instruments, Inc., Oak Ridge, Tennessee), under both the regular and dynamic contact module (DCM) modes. All indentation tests followed the ISO 14577 method (ISO, 2002) under the load control mode and used diamond Berkovich indenter tips. The well recognized Oliver and Pharr<sup>106, 107</sup> method was used to derive the hardness and Young's modulus from each indentation. To eliminate the effect of substrate, multiple indentations were made on each sample with varied maximum indentation loads. The Tuck et al.<sup>108</sup> and Wei et al.<sup>109</sup> methods were adopted to extract the true hardness and elastic modulus of the thin films, respectively. Further details on the nanoindentation testing can be found in Wei et al.<sup>109</sup>.

### 3. Results and Discussion

#### 3.1. Overview of Multilayer Characteristics and Linear LbL Growth



(a)

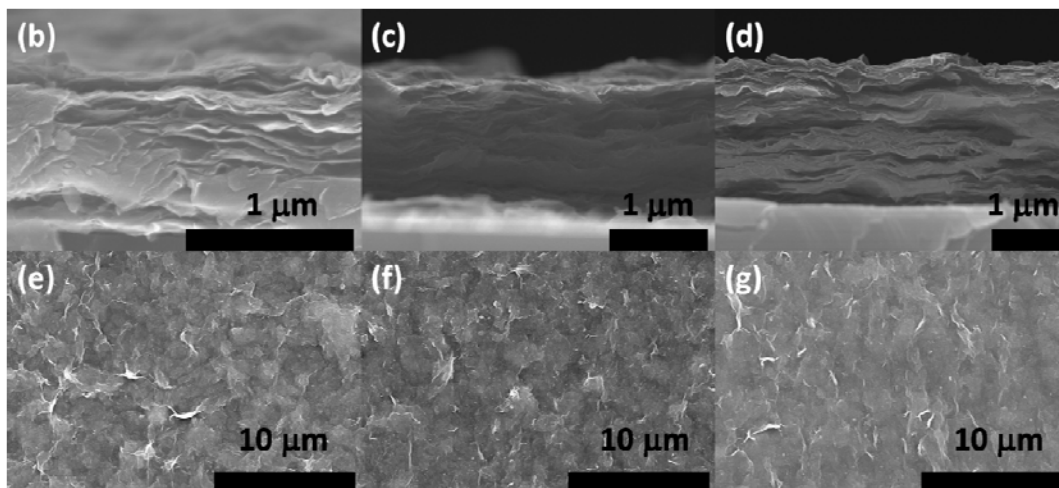


**Figure 22.** (a) The relationship between the multilayer thickness and number of deposition cycles for specimens prepared by using 0.15 M precursor solutions, 10 minutes holding in the precursor, and other fixed parameters specified in the text. Representative cross-sectional and in-plane SEM images of the multilayers prepared by (b, e) 10, (c, f) 20, and (d, g) 30 deposition cycles, respectively.

The characteristics of the  $\{\text{MMT}_x\text{-(sol-gel ZrO}_2\text{)}\}_n$  multilayers with different deposition cycles were presented first. Figure 22(a) shows that a linear relationship exists between the film thickness and the number of deposition cycles for the multilayers prepared under a set of selected control parameters. After 30 deposition cycles, the thickness reaches  $\sim 1950$  nm; yet the layered structure and linear relationship are well maintained (Figure 22). Under this particular synthesis condition (i.e., 10 minutes holding in a 0.15 M precursor solution, and other parameters specified above), the growth rate, defined as the thickness increment per deposition cycle, is calculated to be  $\sim 64$  nm per deposition cycle. Representative cross-sectional and in-plane SEM images are shown in Figure 22(b-g).

The much improved layered and periodic structure, film integrity, and linear growth behavior (as compared with those in our preliminary work<sup>104</sup>) are clearly evident in Figure 22. These improvements are attributed to the use of better exfoliated MMT suspensions and a set of optimized dipping parameters, as described previously in the “Experimental” section. For example, in one set of the optimization experiments, after the holding time in air was varied from 45 seconds to 10 minutes, the thickness of a  $\{\text{MMT-(sol-gel ZrO}_2\text{)}\}_{30}$  multilayer increased only slightly from  $\sim 1920$  nm to  $\sim 1950$

nm, and essentially identical layer structure were obtained (Figure 23). This demonstrates that a holding time of 45 seconds in air is long enough to dry the sol-gel ZrO<sub>2</sub> layers before the next dip in the MMT suspension. As such, in this study, all specimens were held in air for a fixed time of 45 seconds between two consecutive dips. The following three parameters, the precursor concentration, holding time in the precursor solution, and aging time, are varied to probe the growth kinetics of sol-gel layers on MMT surfaces; other parameters are generally fixed after optimization.

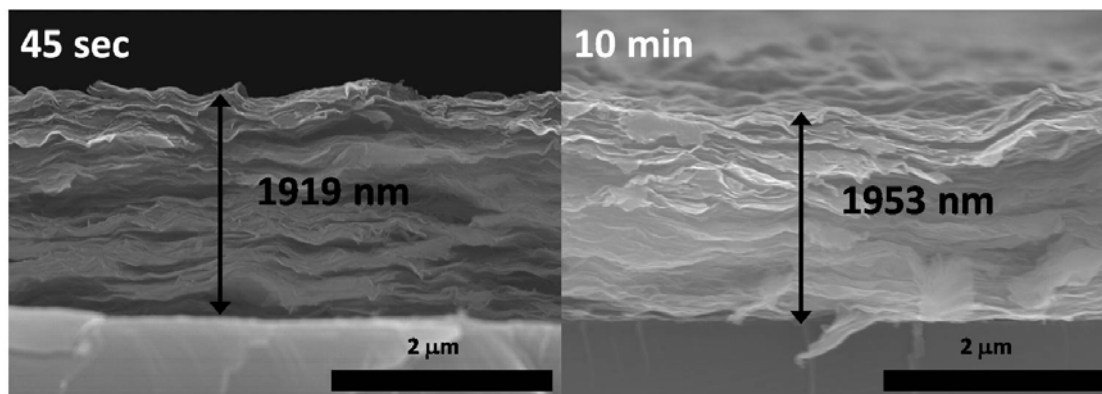


**Figure 23.** Cross-sectional SEM images of {MMT-(sol-gel ZrO<sub>2</sub>)}<sub>30</sub> multilayer synthesized with holding time in air for 45 seconds and 10 minutes.

The film thickness of all specimens is uniform along a horizontal direction, given that the dipping direction is vertical, as reflected by the small error bars in all plots. On the other hand, thickness gradients exist along the vertical direction. Such gradients are less than ~ 10% for specimens that were dipped into the precursor solution for 10 minutes (Figure 24). However, the thickness gradients along the vertical direction can become significant (Figure 24) when the holding time in the precursor is comparable with the

total time for both the dipping and withdrawing processes (i.e., ~ 1 minute each at the current moving speed of 2 cm per minute). This is presumably due to the growth of sol-gel layers during both the dipping and withdrawing processes in the precursor solution, in addition to stagnatic holding in the precursor solution. Because the lower part of the substrate has longer time of immersion than the upper part, a thickness gradient develops along the vertical direction. This effect can be beneficially used to make multilayers with controlled gradients of thickness, but this is beyond the scope of this study.

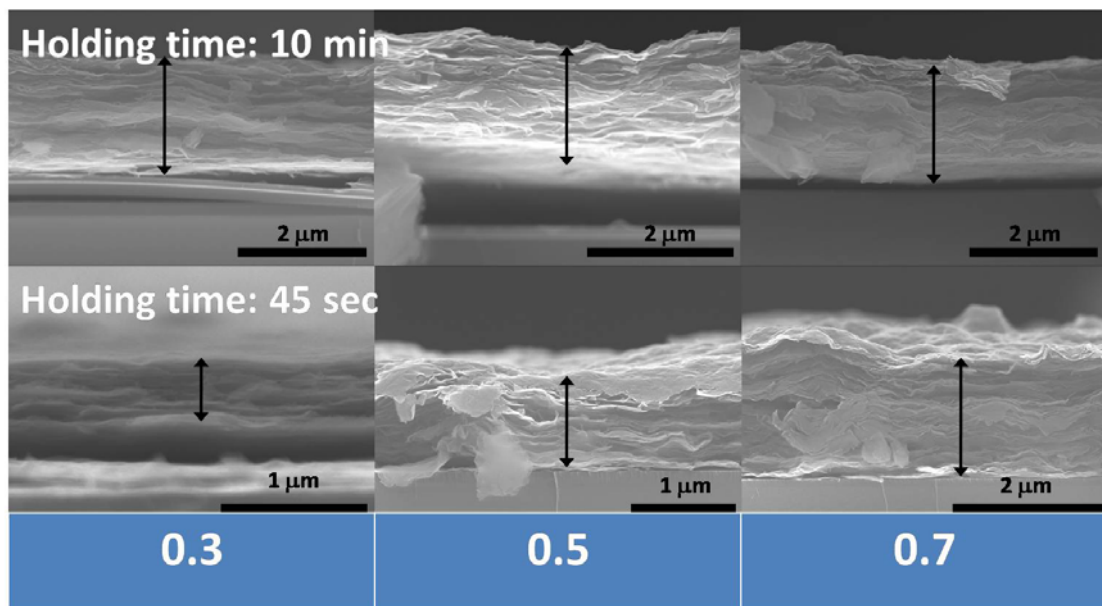


**Figure 24.** Cross-sectional SEM images of  $\{\text{MMT}-(\text{sol-gel ZrO}_2)\}_{30}$  multilayer for holding 10 minutes and 45 seconds in precursor solutions. Numbers in the bottom row represented sampling positions along the immersion direction, and were calculated dividing the total length of the corresponding multilayers.

Free-standing films with planar dimensions greater than 0.5 cm were made via the sacrificial substrate technique described before. Representative SEM and optical images

of a freestanding film are shown in Figure 25. These images indicate that these multilayers exhibit good structural integrity. Although these multilayers were only air-dried, the interfacial bonding between MMT clays and sol-gel ZrO<sub>2</sub> layers is sufficiently strong to permit peeling of the film off the substrate. It is feasible to make larger freestanding multilayers.

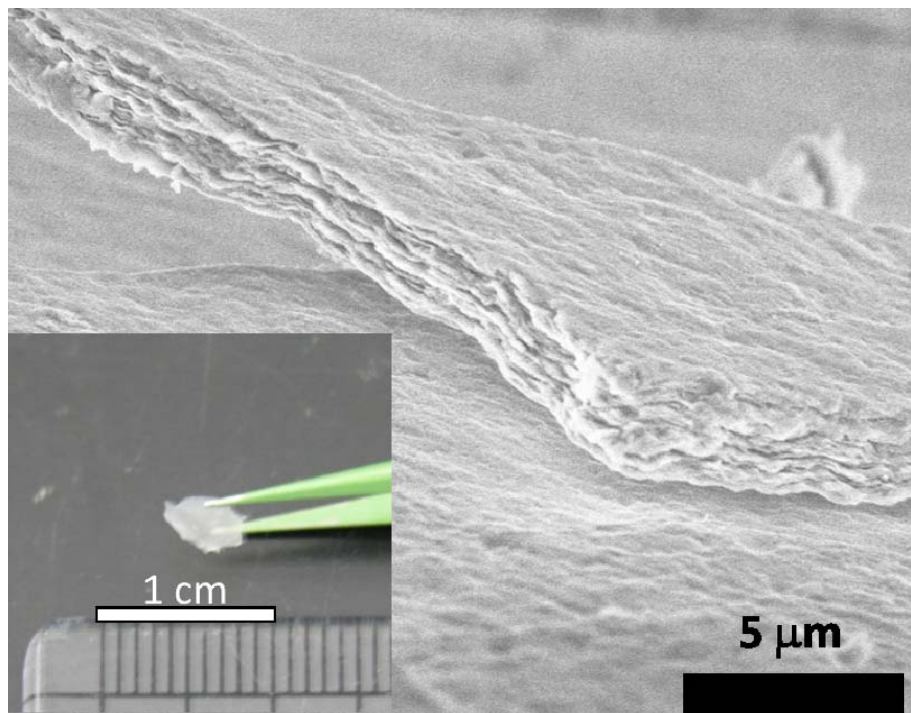


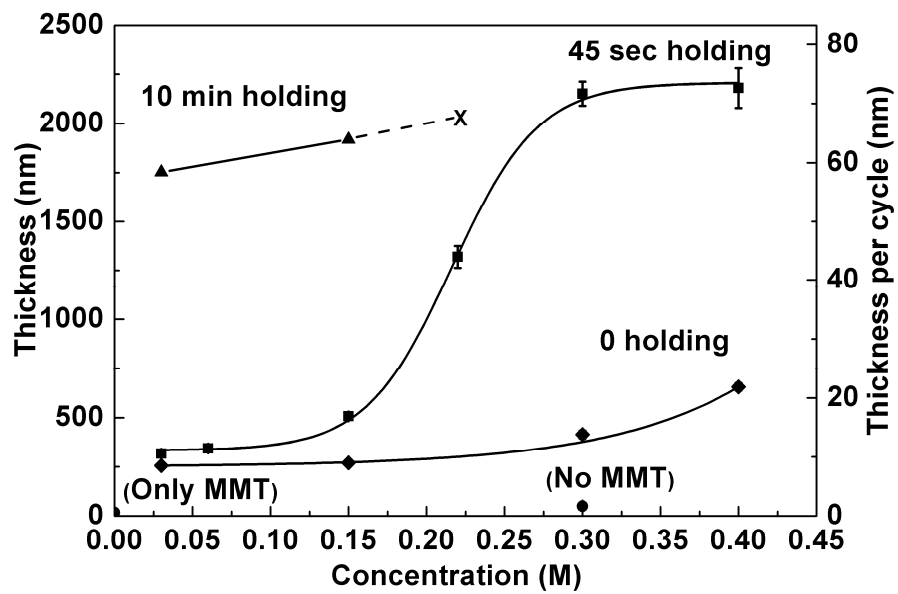
**Figure 25.** An SEM image of a piece of free-standing, air-dried {MMT-(sol-gel ZrO<sub>2</sub>)}<sub>30</sub> multilayer. Inset is an optical photograph of a large piece of freestanding multilayer.

### ***3.2. Growth of Non-Aged Sol-Gel Layers: Effect of Precursor Concentration***

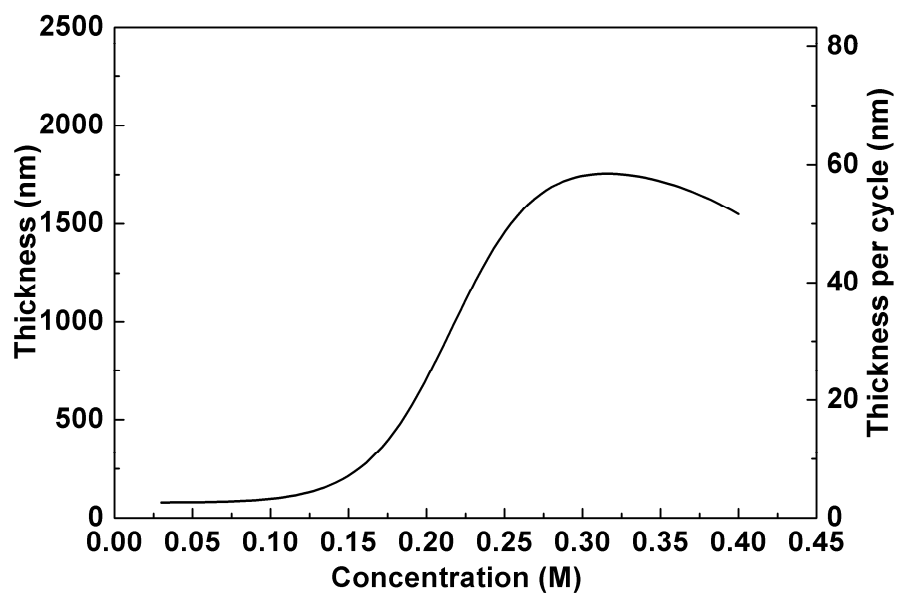
In the first set of systematic experiments designed to investigate the mechanism of growing sol-gel ZrO<sub>2</sub> layers on MMT surfaces, {MMT-(sol-gel ZrO<sub>2</sub>)}<sub>30</sub> specimens were

synthesized using freshly prepared precursor solutions with varied concentrations of 0.03-0.4 M and three specific holding times (i.e., 0, 45 seconds, and 10 minutes). The film thickness vs. the precursor concentration curves are shown in Figure 26 (a). The curve for a holding time of 45 seconds exhibits a characteristic S-shape. In this curve, the film thickness is almost constant ( $\sim 15$  nm per deposition cycle) at low precursor solution concentrations ( $\leq 0.06$  M), but increases rapidly in the concentration range of 0.15-0.30 M, and then finally reaches a saturation level of  $\sim 70$  nm per deposition cycle. The cross-sectional SEM images of selected specimens are shown in Figure 26 (c). Again, the layered structure is clearly observable. With zero holding time in the precursor solution, the film thickness increases only slightly with increasing the precursor concentration, indicating minor and slow deposition of the sol-gel layer during the dipping/withdrawing stage. For a longer holding time of 10 minutes, the film growth rate (per deposition cycle) approaches the saturation level quickly, and the multilayers are no longer uniform at the high zirconium concentrations ( $\geq 0.3$  M) due to the gelatin of the precursor solution.

In Figure 26 (b), the difference between the film thicknesses obtained by 45 seconds and 0 holding times is plotted against the precursor solution concentration to estimate the net thickness of the sol-gel  $\text{ZrO}_2$  layer that grows during the 45 seconds stagnant holding in the precursor solution. This curve, shown in Figure 26 (b), does not follow the classical mass transfer (diffusion) or interfacial reaction controlled kinetics model, which would both suggest a linear dependence of the sol-gel layer thickness on concentration, using the first order of approximations<sup>110</sup>.

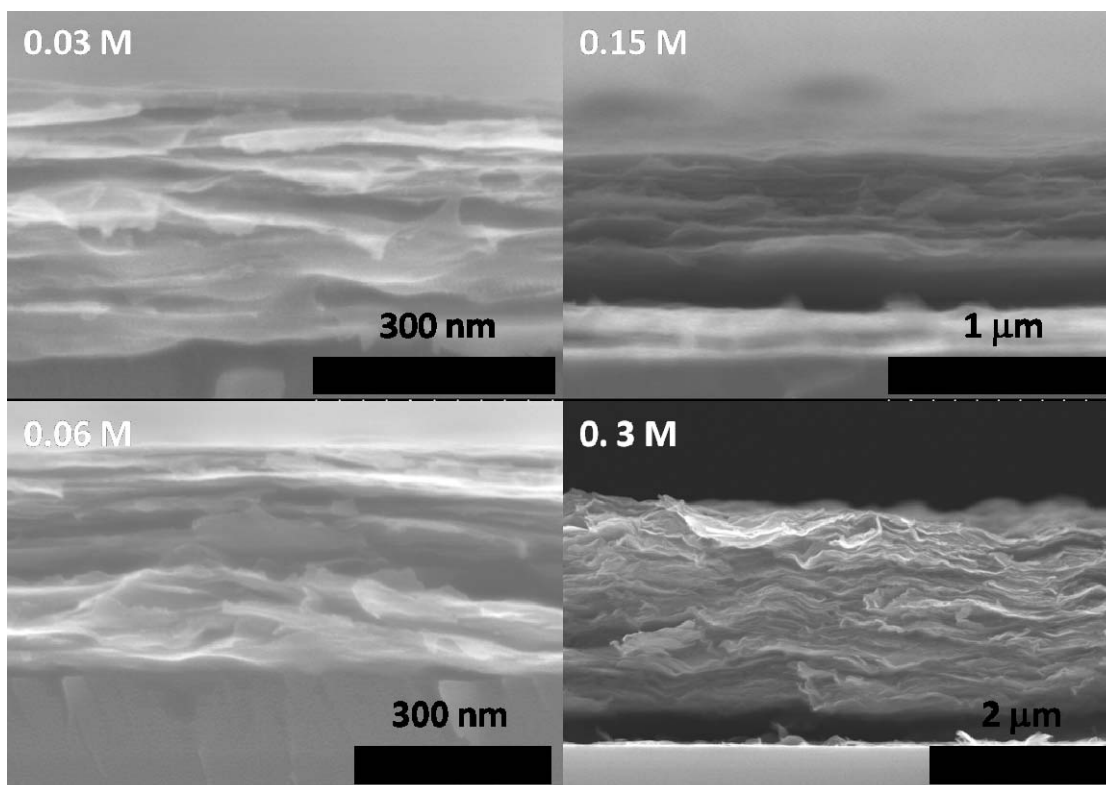


(a)



(b)



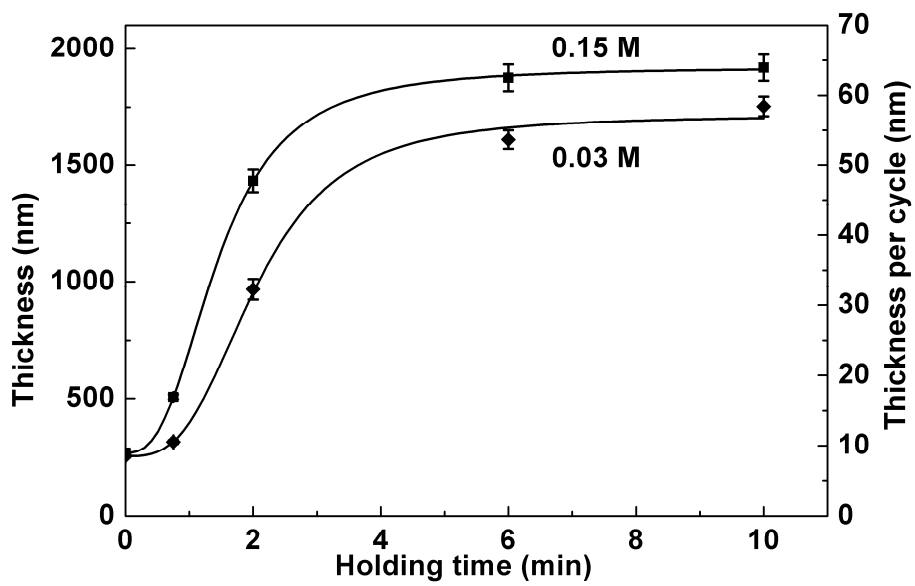


(c)

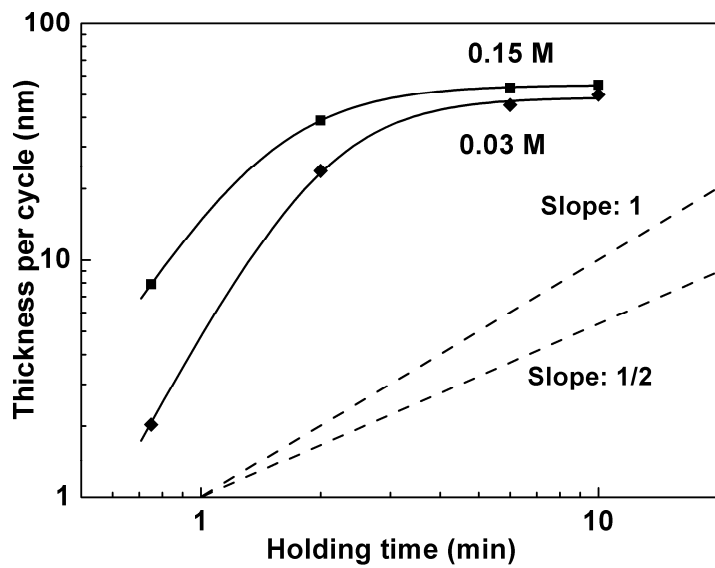
**Figure 26.** (a) The relationship between the film thickness and precursor solution concentration. The holding times in the precursor solutions are labeled. The dashed line and the symbol “X” indicate that the films become non-uniform at high concentrations with prolonged holding time due to the gelation of the solution. As a comparison, the two solid cycles represent the measured thickness for films made by dipping only in MMT suspension (labeled as “Only MMT”) or only in zirconium acetate hydroxide solution (near the origin point, labeled as “No MMT”, holding time = 45 seconds). (b) The relationship between the estimated net thickness for the sol-gel layers grown during 45-second holdings in precursor solutions and the precursor solution concentration. (c) Representative cross-sectional SEM images. The precursor solution concentrations are labeled; holding time = 45 seconds.

### ***3.3. Growth of Non-Aged Sol-Gel layers: Effect of Holding Time***

In the second set of systematic experiments designed to investigate the sol-gel layer growth kinetics, the thickness of the multilayers were analyzed as a function of the holding time (0-10 minutes) in the freshly prepared precursor solutions with two selected concentrations, 0.03 and 0.15 M. The results are shown in Figure 27 (a), while representative cross-sectional SEM images are shown in Figure 27 (c). For both concentrations, the growth of sol-gel layers again exhibits three characteristic regimes: an initial incubation regime with a slow growth speed (to reduce ambiguity, “growth speed” refers to the film thickness change per unit holding time, while “growth rate” is defined as the film thickness change per deposition cycle), an intermediate regime with a high growth speed, and a final saturation regime where the growth speed approaches zero. The maximum growth speeds in the intermediate regime are approximately 20-30 nm per minute of holding time for both curves. The saturation thickness is ~ 48 nm per deposition cycle for 0.03 M and ~ 55 nm per cycle for 0.15 M precursor solution. It is interesting to note that the saturation or self-limiting thickness increases only by ~ 12% when the precursor solution concentration has a fivefold increase from 0.03 to 0.15 M.



(a)



(b)

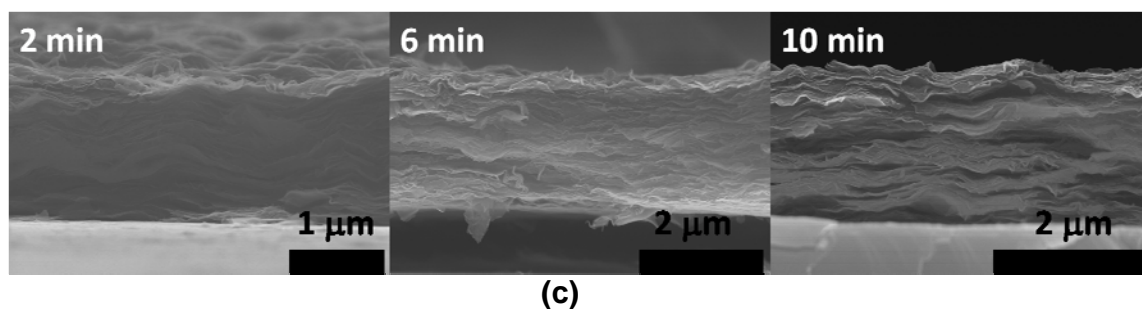


**Figure 27.** (a) The multilayer thickness versus holding time for two different precursor solution concentrations (0.15 M and 0.03 M). (b) a double logarithmical plot of the estimated net thickness of sol-gel layer grown on the MMT surface per cycle versus holding time. (c) Representative cross-sectional SEM images (0.15 M zirconium acetate hydroxide solutions; the holding times are labeled)

With zero-holding time in the precursor solution, the multilayer film grows at a rate of  $\sim 8$  nm per deposition cycle, which is about the same for both concentrations. This net thickness increment per deposition cycle results from the thickness of the MMT layers and the hydrodynamic adsorption of sol-gel  $\text{ZrO}_2$  during both the dipping and withdrawing processes. To the first order of approximation, this growth rate can be used as a reference value to estimate the net growth of sol-gel  $\text{ZrO}_2$  layers while holding the specimens in the precursor solutions.

To directly analyze the growth kinetics in the 0.03 and 0.15 M solutions, the net thickness of the sol-gel  $\text{ZrO}_2$  layers, obtained by subtracting the reference value of  $\sim 8$  nm as discussed above, are re-plotted at a double logarithmic scale in Figure 27 (b). If the growth of a sol-gel  $\text{ZrO}_2$  layer on the MMT surfaces were considered as a precipitation (i.e., first-order phase transformation) process without electrostatic interactions, the

classical kinetic models would be applicable. In such cases, the deposition process would be controlled by either interfacial reaction rates or mass transfer (diffusion) rates<sup>110</sup>. For the former, the sol-gel layer should grow linearly with time ( $t$ ), i.e., the layer thickness is

$$\chi \propto t. \quad (1)$$

For the latter, the sol-gel layer should grow parabolically or the thickness is

$$\chi \propto \sqrt{t}. \quad (2)$$

The above two equations can be represented by the two linear lines with slopes of 1 and  $\frac{1}{2}$ , respectively, in the double logarithmic plot, as indicated by the two dashed lines in Figure 27 (b). However, the experimental data in Figure 27 (b) show that the growth speeds between 0.75 to 2 minutes exhibit slopes that are greater than those predicted by either interfacial reaction or mass transfer controlled kinetics. It suggests that the sol-gel layer growth in this regime is surface-controlled and is further accelerated by the electrostatic attractions resulting from the large negative surface charges on the MMTs.

Furthermore, at a later stage (i.e., when holding time is greater than 6 minutes), the further growth of the sol-gel layer virtually stops. In fact, the observed saturation thicknesses in both Figure 27 and Figure 26 are in the same range of 50-60 nm per deposition cycle, after subtracting the estimated thickness (i.e., 8 nm per deposition cycle) of MMT layers. This saturation thickness is significantly greater than the commonly known monolayer or submonolayer self-limiting thickness<sup>87-89</sup>. If the growth of sol-gel layer between 0.75 to 2 minutes holding time is indeed controlled by electrostatic attractions, this observed self-limiting growth of sol-gel layer on the MMT

surfaces may be explained, as a hypothesis, by the screening of the electrostatic interactions. To quantify the screening effect and to justify this hypothesis, the Debye length ( $\kappa^{-1}$ ) is estimated to be around 30 nm for 0.15 M precursor solution, using the following equation:

$$\kappa^{-1}(\text{nm}) = 10 / \sqrt{I(\text{mM})} \quad , \quad (3)$$

where  $I$  is the ionic strength, which is estimated to be  $\sim 0.1$  mM based on the measured pH value of 4.06, assuming that  $\text{H}^+$  is the leading cations that are balanced by monovalent anions. Thus, the potential at a distance of 69 nm from the MMT surface drops to 10% of the surface potential. It should be noted that the actual screening effect will change when the sol-gel layer forms on the MMT surface. Because the effective dielectric constant of and the charge distribution in the sol-gel layer are both unknown, it is difficult to quantify the screening effect more accurately. Nonetheless, such a simple estimate of the screening length, although not rigorous, supports the above hypothesis.

#### ***3.4. Coupling of the Growth of MMT and Sol-Gel ZrO<sub>2</sub> Layers***

To further examine whether the growth of MMT layers and sol-gel ZrO<sub>2</sub> layers is coupled or independent, two control experiments were conducted to grow MMT only (i.e., by skipping the dips in the precursor solution) and to grow the sol-gel ZrO<sub>2</sub> layer only (i.e., by skipping the dips in the MMT suspension), respectively. When the substrate was dipped in a MMT suspension and deionized water twice for rinsing alternately for 30 deposition cycles, the resultant film's total thickness is less than 20 nm (Figure 28). Since

the thickness of one monolayer of exfoliated MMT (i.e., a 2:1 or T-O-T layer in the clay mineralogy concepts) is about 1 nm<sup>33</sup>, the observed overall growth rate of 20 nm (or ~ 20 MMT T-O-T platelets) in 30 deposition cycles suggested that the LbL growth is neither linear nor continuous. Instead, after several layers of clay platelets were deposited, further adhesion of clay platelets in subsequent deposition cycles was impeded due to electrostatic repulsions among MMT layers.

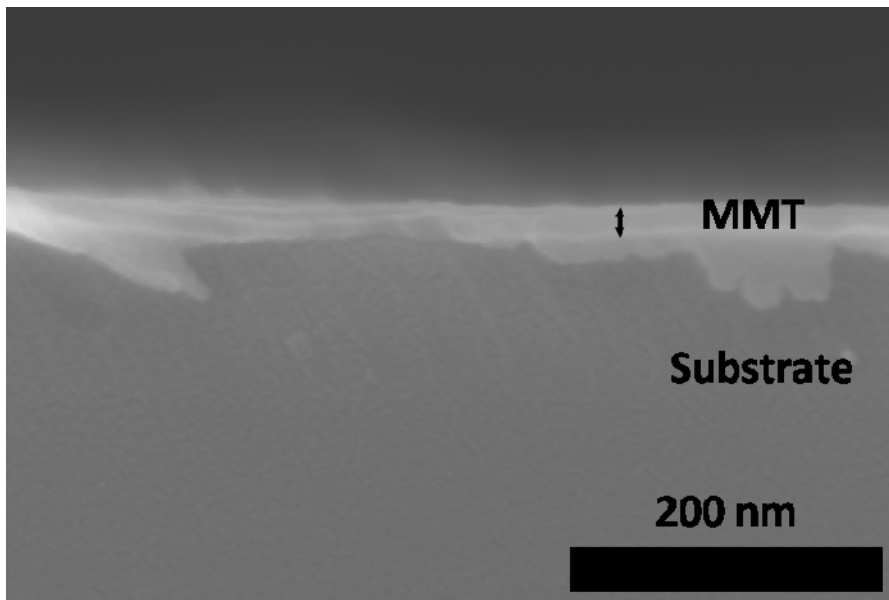


**Figure 28.** A representative cross-sectional SEM image for a film made after dipping a substrate in a MMT suspension and rinsing water (twice each cycle) for 30 deposition cycles (i.e., without dipping in a zirconium acetate hydroxide solution).

This gives an average growth rate of 0.6 nm per deposition cycle, which is less than the thickness (i.e., ~ 1 nm) of one monolayer of exfoliated MMT<sup>33</sup>. This growth rate is nominal, because we do not expect a linear LbL growth in this case. This observation clearly demonstrates that MMT layers cannot continuously grow without

depositing sol-gel ZrO<sub>2</sub> layers in between. For comparison, when the thickness vs. concentration curve in Figure 26 (a) for zero time of holding in the precursor solution is extrapolated to 0 M concentration, a growth rate of ~ 8 nm per cycle (i.e., ~ 250 nm for 30 deposition cycles) is obtained. This extrapolated growth rate of ~ 8 nm per deposition cycle is significantly greater than the observed overall growth rate of 20 clay platelets in 30 deposition cycles without depositing sol-gel layers. It is therefore concluded that the MMT deposition mechanisms are remarkably different for the growth with and without the deposition of the sol-gel layers. One possible reason is that the negative surface charges on the MMT will prevent continuous adsorption of additional MMT layers unless a sol-gel oxide was deposited to neutralize or reverse charges on the surface of the growing film.

In the second set of control experiments, substrates were dipped only in the 0.3 M precursor solution and deionized water twice repeatedly, but not in the MMT suspension. It was found that the sol-gel layers grow linearly. The growth rate is estimated to be ~ 1.6 nm per deposition cycle, as shown in Chapter 3. This value is similar to the size of a zirconia polyoxocation (i.e., ~ 2 nm<sup>49, 111</sup>) that is presumably present in the precursor solutions. This observation suggests that about one monolayer of zirconia polyoxocations was deposited to the substrate per deposition cycle. This finding is further supported by the fact that, when the holding time increases from 45 seconds to 10 minutes, there is virtually no increase in the film thickness (Figure 29(a) vs. Figure 29 (b)). Therefore the growth of sol-gel layers is self-limited to ~ 1.6 nm per deposition cycle when no MMT layers are involved. All these results suggest that the growth of sol-gel ZrO<sub>2</sub> layers



follows a similar mechanism that was proposed to control the successive ionic layer adsorption and reaction (SILAR) process, where an ideal growth of one monolayer of ionic species per deposition cycle is usually expected<sup>87-89</sup>. In contrast, when the sol-gel layers were grown on the MMT surfaces under the same dipping conditions, significantly increased growth rates that are much greater than the monolayer growth were observed. For instance, the total growth rate for a 45 seconds holding time in a 0.3 M precursor solution is  $\sim 70$  nm per deposition cycle. As a rough estimate, the growth rate of 8 nm per deposition cycle, obtained by extrapolating the 45 seconds holding time curve to 0 M precursor solution (Figure 26 (a)), is used to represent the thickness increment of the MMT layers per deposition cycle. The difference of these two values,  $\sim 62$  nm per deposition cycle, is then attributed to the net growth of the sol-gel layer on the MMT surfaces, which is  $\sim 40$  times greater than that observed for dipping only in the precursor solution (Figure 29). This comparison unequivocally shows that the growth rates of sol-gel layers are significantly increased due to the presence of negatively charged MMT layers. This increase can be attributed to primarily the presence of electrostatic attractions, and secondarily the increased surface roughness of the MMT surfaces.

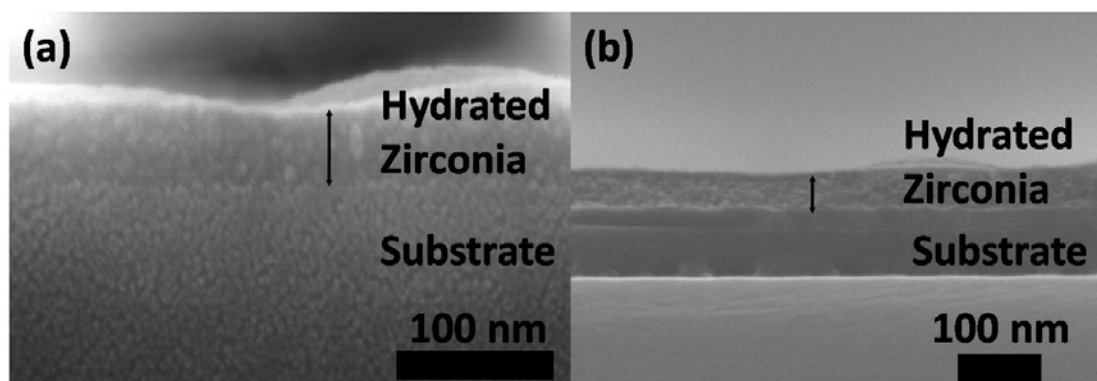


**Figure 29.** Cross-sectional SEM images of films made via dipping substrates in 0.3 M zirconium acetate hydroxide solutions for 30 deposition cycles with (a) 45 seconds and (b) 10 minutes holding time in the solutions, respectively.

### 3.5. Additional Discussion of Possible Sol-Gel Growth Mechanisms

To date, the exact sequence for the sol-gel reaction to form  $ZrO_2$  is unknown. A mostly likely process consists of three steps: hydrolysis, which likely results in weakly ionized zirconium polyoxocations of  $\sim 2$  nm in size<sup>94</sup>; condensation/polymerization, which may generate neutral and soluble zirconium polymer species with a  $(Zr^{4+}):(\text{CH}_3\text{COO}^-)$  ratio of 1:2<sup>94</sup>; and gelation via replacing  $\text{CH}_3\text{COO}^-$  groups with  $\text{OH}^-$  groups on the polymeric zirconium species, which results in the precipitation of insoluble gels at a  $(Zr^{4+}):(\text{CH}_3\text{COO}^-)$  ratio of  $\sim 1:1$ . Possible surface initiated sol-gel processes for the low and high concentration regions (as shown in Figure 26 (a)) are proposed as follows. At the low concentration region, the precursor solution is likely composed of zirconium polymer species<sup>94</sup> and a smaller portion of zirconium polyoxocations<sup>49</sup>. Since the  $\text{Na}^+$  cations on MMT surfaces are exchangeable with other monovalent cations in solution (note that the MMT has an exchange capacity of 92.6 meq per 100 g)<sup>72</sup>,  $\text{Na}^+$

cations on MMT may exchange with zirconium polyoxocations, leading to the formation of a submonolayer of zirconium polyoxocations on MMT surfaces. In the low concentration range (i.e.,  $< \sim 0.1$  M) in Figure 26, the difference in growth rates between 0 and 45 seconds holding time is small,  $\sim 1.4$  nm per cycle, which is less than the thickness of one monolayer of zirconium polyoxocations (i.e., 2 nm in size). This suggests that monolayer adsorption via cation exchanging may be the main growth process at low concentrations, and additional surface-initiated gelation process is not significant. In the high concentration range (i.e.,  $> \sim 0.2$  M) in Figure 26 (a), the growth rate difference is much significant. This indicates that surface-initiated gelation may be dominant, and electrostatic interactions can enhance the deposition of sol-gel layer. This surface initiated sol-gel process may be sustained by the precipitation via replacing the  $\text{CH}_3\text{COO}^-$  groups with  $\text{OH}^-$  groups on polymeric zirconium species.

### ***3.6. Effects of Aging (Aged Zirconium Acetate Used as Precursors)***

With no aging, the viscosity of the freshly prepared zirconium acetate hydroxide solution is small or not measurable by a commercial viscosity meter. Thus, the deposition of sol-gel  $\text{ZrO}_2$  layers is likely a surface sol-gel process (a.k.a., no significant gelation in the bulk solution). When the precursor solution is aged, a sol-gel process will occur in the bulk solution, resulting in a significant increase in viscosity<sup>82</sup>. To investigate how such aging process affects sol-gel layer deposition and growth, a 0.15 M precursor solution was first aged for various durations at 60 °C before it was used to prepare the  $\{\text{MMT}-(\text{sol-gel ZrO}_2)\}_{30}$  multilayers. It was found that the 0.15 M precursor

solution turned into a viscous gel after aging for 21 hours at 60 °C. At such viscosity, uniform multilayer films could no longer be synthesized. As such, in this series of experiments, the maximum aging time was limited to 14 hours.

Figure 30 shows the relationships between the multilayer thickness and aging time for two sets of specimens that were prepared with 0 and 45 seconds holding time in aged precursor solutions, respectively. In general, the aging process causes an increase in the viscosity of the sol and affects the hydrodynamics of the film growth during the withdrawing step and, presumably to a less extent, advancing/dipping step. Empirically, it is common to assume that the viscosity ( $\eta$ ) of an aged sol increases exponentially with aging time ( $t$ ), i.e.,  $\eta = A_\eta e^{t/\tau}$ , where  $A_\eta$  and  $\tau$  are two constants<sup>82</sup>. Then, the entrained film thickness ( $h$ , which scales the final total film thickness) during dipping can be estimated by the Landau-Levich Equation<sup>86</sup>:

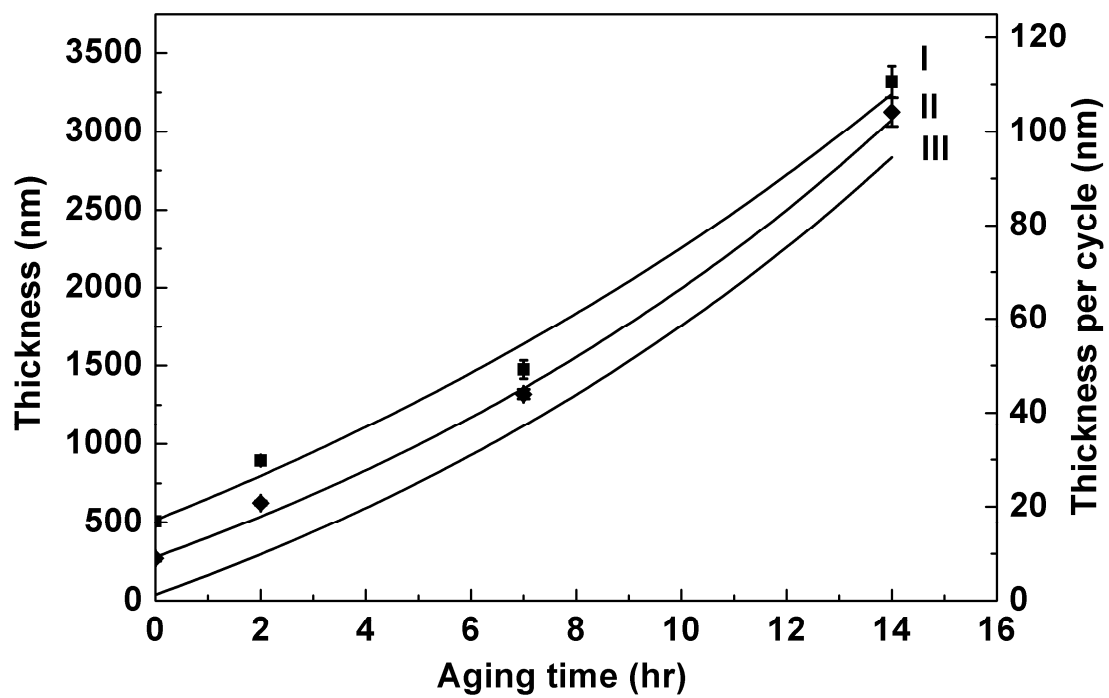
$$h = 0.94(A_\eta e^{t/\tau} U)^{2/3} / \gamma_{LV}^{1/6} (\rho g)^{1/2} \quad (4)$$

where  $U$  is the withdrawal speed and  $\rho$  is the density of the sol. We may assume, for simplicity, that the surface tension ( $\gamma_{LV}$ ) is a constant<sup>112</sup>, and there is no volume change during gelation. Then, Eq. (4) can be simplified as

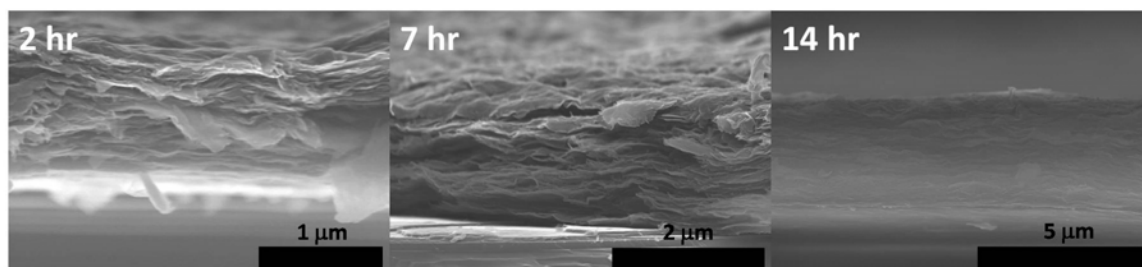
$$h \propto e^{\frac{2}{3\tau}t} \quad (5)$$

In other words, the thickness of the sol-gel film deposited during the hydrodynamic process is an exponential function of aging time, at a first order of approximation. To compare the above equation with experimental data, the net thickness of the sol-gel ZrO<sub>2</sub>

layers is estimated in the hydrodynamic process via subtracting the thickness of MMT layers of  $\sim 8$  nm per deposition cycle (which was estimated by extrapolating to 0 precursor solution concentration in Figure 26 (a) from the actual measured multilayer thickness; see the discussion above). This corrected curve, shown as Curve III in Figure 30 (a), can be well fitted by an exponential function [ $h = 60.1 \times \exp(t \text{ (hours)}/14.9) - 58.7$  (nm/cycle)]. Hence, this agreement supports that the deposition of aged sol is controlled by a hydrodynamic process following the Landau-Levich Equation.



(a)



(b)

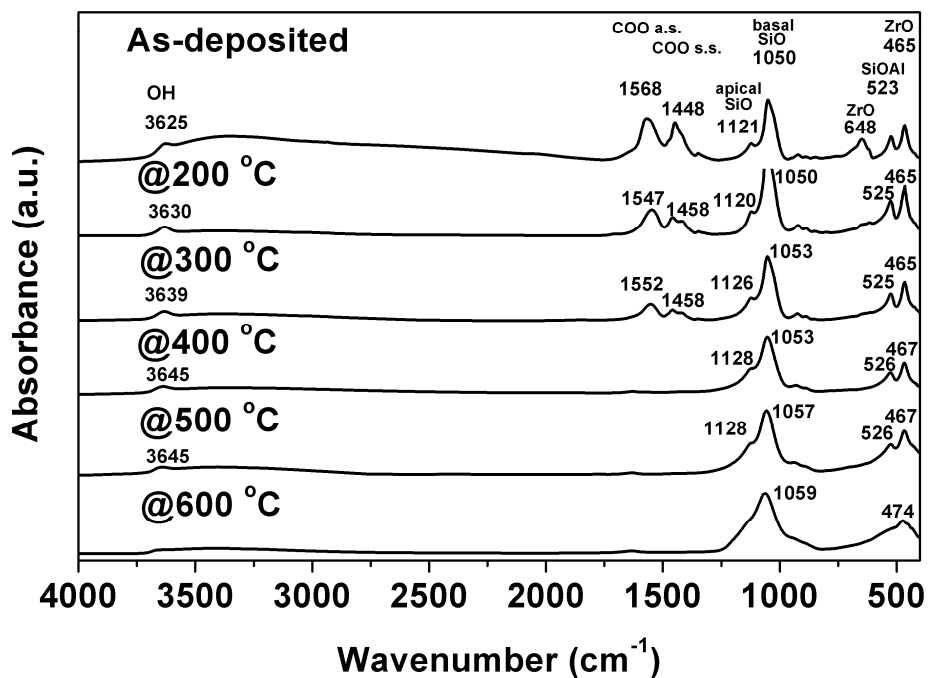
**Figure 30.** The multilayer thickness versus precursor solution aging time at 60 °C for holding time of 45 (Curve I) and (Curve II) 0 seconds, respectively. Curve III represents the net thickness of hydrodynamic deposited sol-gel layers (estimated by subtracting the thickness of MMT layer from Curve II). (b) Representative cross-sectional SEM images of selected multilayers (corresponding to Curve I).

The aging time constant can be intentionally tuned by changing precursor concentration, solution pH, temperature, and other parameters that affect the sol-gel kinetics. It should be noted that the Landau-Levich Equation is not applicable when the aging time,  $t$ , approaches zero, where the film growth is no longer controlled by hydrodynamics. This may explain the occurrence of an extra constant in the fitted thickness vs. aging time function. Another interesting finding is that the difference between the thicknesses of multilayers for the two sets of specimens is almost independent of the aging time, as shown in Curves I vs. II in Figure 30 (a). This again indicates that the sol-gel layer growth is controlled by hydrodynamics (i.e., the increase in viscosity does not significantly affect the deposition of sol-gel layers during the holding in the aged sols). Representative cross-sectional SEM images of multilayers made using aged precursors are shown in Figure 30 (b); these images show that nanoscale

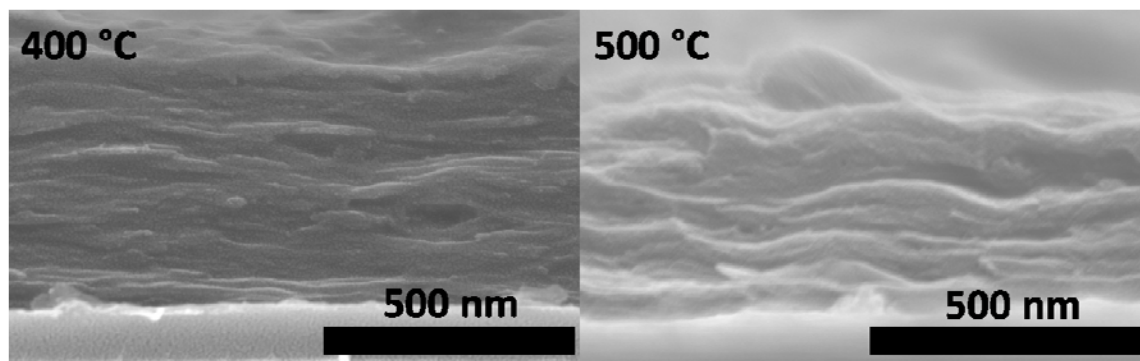
layered structures are well maintained in these multilayers, where the growth of sol-gel layers is controlled by hydrodynamics.

### ***3.7. Structure and Effects of Annealing***

The as-deposited films are typically hydrated and contain some residual acetate groups, which can be removed by controlled annealing. Thus, we conducted further experiments to investigate the thermal stability and the changes in molecular structures of the {MMT-(sol-gel ZrO<sub>2</sub>)}<sub>30</sub> multilayer after annealing at different temperatures. FTIR spectra of an as-deposited specimen and the specimens annealed between 200 and 600 °C (for 2 hours) are shown in Figure 31 (a). The characteristic vibration bands of MMT and zirconium acetate are present in an as-deposited multilayer specimen. The 3625 cm<sup>-1</sup> band is related to the stretching mode of O-H attached to the Al or Mg in the MMT octahedral sheet layer<sup>72</sup>. The 1121 and 1050 cm<sup>-1</sup> bands are related to the two Si-O stretching bands for apical and basal oxygen in the MMT, respectively. The 523 cm<sup>-1</sup> band is related to Si-O-Al bending in the MMT<sup>113</sup>. On the other hand, the two major bands of zirconium acetate can be found at 1568 and 1448 cm<sup>-1</sup>, which are related to asymmetric and symmetric COO stretching bands<sup>114</sup>. The 646 cm<sup>-1</sup> band is related to Zr-O stretching band<sup>115</sup>. The 465 cm<sup>-1</sup> band may be related to Zr-O bending from tetragonal Zr-O<sup>116, 117</sup>. These bands indicate that hydrated sol-gel ZrO<sub>2</sub> and some residual acetate groups are present in the as-deposited films.



(a)



(b)

**Figure 31.** (a) FTIR spectra of an as-deposited  $\{\text{MMT}-(\text{sol-gel ZrO}_2)\}_{30}$  multilayer and multilayers annealed at different temperatures. All specimens were made using 0.15 M



precursor solution and a holding time of 45 seconds. (b) Cross-sectional SEM images of selected annealed multilayers.

When the multilayers were annealed, the molecular structure changed gradually (Figure 31 (a)). Two strong COO stretching bands weaken with increasing annealing temperature and eventually disappear at 400 °C. The 646  $\text{cm}^{-1}$  band from the Zr-O stretching band disappears at 300 °C, inferring the complete removal of  $\text{CH}_3\text{COO}$  groups at 300 °C. The 1121  $\text{cm}^{-1}$  band of Si-O (apical oxygen) stretching becomes a weak shoulder at 500 °C and virtually disappears at 600 °C, indicating the onset of the MMT crystal structure collapse at this temperature. The disappearance of 3625  $\text{cm}^{-1}$  OH stretching at 600 °C is another evidence for the disintegration of MMT crystal structure. However, the 465  $\text{cm}^{-1}$  band, which is the combination of Si-O and Zr-O bending bands, remained strong at all temperatures but shifted slightly to 474  $\text{cm}^{-1}$  at 600 °C. In summary, annealing at ~ 400 °C results in the formation of MMT-zirconia multilayers with MMT crystal structures intact, but the acetate residues and moisture are removed. Selected SEM images of annealed multilayers are shown in Figure 31 (b), and these images show that the layered structures are well maintained after annealing at 400-500 °C.

The averaged thickness of an as-deposited (air-dried)  $\{\text{MMT}-(\text{sol-gel ZrO}_2)\}_{30}$  multilayer is 507 nm  $\pm$  11 nm. After annealing at 400 °C for 2 hours, the average thickness is reduced by ~ 13% to 439 nm  $\pm$  15 nm. It is further reduced to 381 nm  $\pm$  8 nm

after annealing at 600 °C for 2 hours (i.e., ~ 25% linear shrinkage from the as-deposited multilayer).

The XRD patterns of as-deposited and annealed  $\{\text{MMT}_x\text{-(sol-gel ZrO}_2\text{)}\}_{30}$  multilayers were shown in Figure 32. A strong MMT (001) peak with a  $d$ -spacing of ~ 1.2 nm was found in the XRD pattern of as-deposited multilayer, implying the presence of stacked nanoclay platelets, which are likely orientated parallel to the surface. The crystallite size (perpendicular to the MMT (001) plane) calculated based the Scherrer Equation was ~ 2.6 nm. Consistently, our kinetic growth study discussed above suggested that  $< \sim 8$  nm thick MMTs were deposited in each deposition cycle (see elaboration in §3.4). After annealing at 400 °C, the MMT (001) peak became weaker, but it is still distinguishable. This indicated the partial loss of crystallinity of the MMT stacks. When the annealing temperature was increased to 600 °C, the MMT (001) peak virtually disappeared, indicating the disintegration of MMT stacks. These XRD results of annealing effects are consistent with the FTIR results discussed above. After annealing at 400-600 °C, a wide bump appeared at  $\sim 2\theta = 29\text{-}30^\circ$ , indicating the partial crystallization of ZrO<sub>2</sub>. This broad zirconia peak appears to be a sum of a diffused monoclinic ZrO<sub>2</sub> (-111)<sub>m</sub> peak ( $2\theta = 27.3^\circ$ ) and a diffused tetragonal ZrO<sub>2</sub> (111)<sub>t</sub> peak ( $2\theta = 30.3^\circ$ ), as labeled in Fig. 9. The equivalent crystallite size calculated based the Scherrer Equation was ~ 1.5-2.2 nm (dependent on whether we consider this bump as a single peak or double peaks), indicating that ZrO<sub>2</sub> is poorly crystallized (largely amorphous or possibly nanocrystalline) after annealing at 400-600 °C.

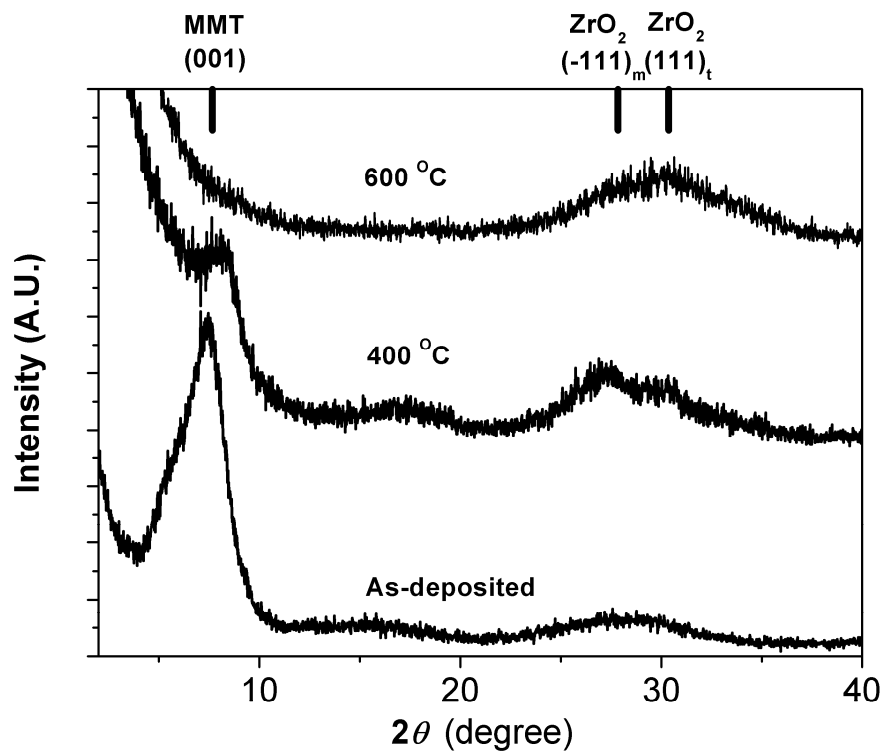


**Figure 32.** XRD patterns of as-deposited and annealed  $\{\text{MMT}_x\text{-(sol-gel ZrO}_2\text{)}\}_{30}$  multilayers. Annealing temperatures are labeled.

### 3.8. Mechanical Properties

Table 6 summarizes the derived mechanical properties of several multilayer films. In general, both the hardness  $H$  and elastic modulus  $E$  of the as-deposited films are much lower than those of the annealed ones, because the former contains a significant amount of water in the structure, present either as absorbed water inside the MMT interlayer spaces or as hydrated water in the hydrated oxide gels. Annealing significantly enhances the hardness and elastic modulus. As the data analysis has eliminated the substrate effect,

the effect of film thickness on the hardness and mechanical properties is also removed. Consistently, measurements of the two films,  $\{\text{MMT}_x\text{-(sol-gel ZrO}_2)\}_{30}$  and  $\{\text{MMT}_x\text{-(sol-gel ZrO}_2)\}_{60}$ , resulted in similar results. Furthermore, the inclusion of a soft oxide,  $\text{SnO}_2$ , significantly reduces both the hardness and elastic modulus of a  $\{\text{MMT}_x\text{-(sol-gel ZrO}_2)\text{-MMT}_x\text{-(sol-gel SnO}_2)\}_{15}$  multilayer. This particular result clearly demonstrated that the properties (e.g., elastic modulus) of these nanocomposite multilayers can be intentionally tuned via changing their designed structure. Finally, the measured elastic modulus of the  $\{\text{MMT}_x\text{-(sol-gel ZrO}_2)\}_n$  multilayers are  $\sim 40\text{-}45$  GPa, which are significantly lower than those of monoclinic  $\text{ZrO}_2$  ( $\sim 244$  GPa at room temperature<sup>118-120</sup>) and MMT (250-260 GPa for a single MMT nanoplatelet<sup>121</sup>). Since it is well established the elastic modulus of a ceramic material depends on its porosity (e.g., a prior study showed that the modulus of monoclinic  $\text{ZrO}_2$  decreases from  $> 200$  GPa to  $\sim 92$  GPa with 22.8% porosity<sup>118</sup>), this result suggested the presence of significant porosity in these nanocomposite multilayers even after annealing.

**Table 6.** The measured hardness and elastic modulus of clay-oxide multilayers prepared using 0.40 wt.% clay concentration. The nano mechanical tests were conducted in LSU by Z. Wei and G. Zhang using our specimens.

Specimen	Hardness $H$ (GPa)	Modulus $E$ (GPa)
$\{\text{MMT}_x\text{-(sol-gel ZrO}_2)\}_{30}$	As-deposited	0.33
	Annealed at 600 °C	1.68
$\{\text{MMT}_x\text{-(sol-gel ZrO}_2)\}_{60}$	As-deposited	0.39
	Annealed at 600 °C	1.86
$\{\text{MMT}_x\text{-(sol-gel ZrO}_2)\text{-MMT}_x\text{-(sol-gel SnO}_2)\}_{15}$	As-deposited	0.43
	Annealed at 400 °C	1.32
	Annealed at 600 °C	1.50

#### 4. Conclusions

We report an optimized LbL synthesis route to fabricate a new class of multilayers,  $\{\text{MMT}_x\text{-(sol-gel ZrO}_2)\}_n$  with an ordered layer structure and sol-gel oxide layers as structural “glues”. The film growth rate can be controlled between ~ 10 nm and ~ 60 nm per cycle via varying the precursor concentration, holding time in the precursor solution, and precursor aging time. A series of systematic experiments and kinetic studies led to the following main conclusions. First, the growth of the MMT and sol-gel ZrO<sub>2</sub> layers is strongly coupled, and these two oppositely charged building units can enhance each other significantly, primarily due to electrostatic attractions. Second, the growth

kinetics of the sol-gel layers cannot be explained by simple mass diffusion or interfacial reaction controlled kinetic models, indicating that the electrostatic interactions may significantly impact the growth of sol-gel ZrO<sub>2</sub> layers on the MMT surfaces. Third, the growth of sol-gel ZrO<sub>2</sub> layers on MMT surfaces exhibit a self-limiting thickness of ~ 50-60 nm, which may be explained by the screening of the electrostatic interactions. Fourth, when the zirconium acetate hydroxide solutions are aged, the growth of sol-gel layers is controlled by a hydrodynamic process that obeys the well-known Landau-Levich model. Fifth, isothermal annealing at ~ 400 °C will dehydrate the multilayers and remove the residue acetate groups without damaging the MMT nanoplatelets and the ordered layer structure of the films. Finally, the mechanical properties (hardness and elastic modulus) of these composite multilayers have been measured. Nanomechanical measurements also showed that the elastic modulus (and presumably other properties) of these composite multilayers can be intentionally tuned by changing the multilayer design and that significant porosity is present in these multilayers even after annealing.

This study demonstrated the feasibility of replacing polyelectrolytes by sol-gel oxides as “glues” to fabricate LbL assembled multilayers. Various potential applications for this new class of all-inorganic {MMT<sub>x</sub>-(sol-gel ZrO<sub>2</sub>)<sub>n</sub>} multilayers, as well as various other types of {nanosheet-(sol-gel oxide)<sub>n</sub>} and {nanoparticle-(sol-gel oxide)<sub>n</sub>} multilayers with similar structures, will be envisioned and discussed in Chapter 8.

## CHAPTER SIX

### SYNTHESIS OF NANOCLAY-NANOPARTICLE MULTILAYERS

#### 1. Introduction

In prior chapters, we reported the synthesis of {nanoclay-(sol-gel oxide)}<sub>n</sub> multilayers by an LbL technique. An alternative method to incorporate oxide components is using oxide nanoparticles, to make {nanoclay-(oxide nanoparticle)}<sub>n</sub> multilayers with a new “plate-ball” architecture. In addition to potential new applications, {nanoclay-(oxide nanoparticle)}<sub>n</sub> multilayers provide a platform to study electrostatic interactions during the LbL assembling process with well-defined geometry and surface charge states.

In prior studies, nanoparticles have been used as building blocks to make polymer-nanoparticle multilayers<sup>95, 122-124</sup> or nanoparticle-nanoparticle multilayers<sup>11, 12, 52, 53</sup>. In suspensions, nanoparticles are either negatively or positively charged. On one hand, negatively charged CdS, PbS, TiO<sub>2</sub><sup>122</sup>, and SiO<sub>2</sub><sup>95</sup> nanoparticles were used to synthesize polymer-nanoparticle multilayers with PDDA polycations. On the other hand, positively charged Au (surfactanted with the positive poly(amidoamine) dendrimer)<sup>123</sup> and Co-Zn-Fe ferrite<sup>124</sup> nanoparticles were used together with negatively charged PSS polyanions to synthesize multilayers.

Furthermore, a few all-nanoparticle multilayers have been synthesized. Iler *et al.* made inorganic nanoparticle multilayers using negatively charged SiO<sub>2</sub> and positively charged boehmite fibrils in 1960s<sup>52</sup>, but this work did not receive much attention at that time. Lee *et al.* at MIT re-examined the possibility to make all-nanoparticle multilayers

by synthesizing  $\text{TiO}_2\text{-SiO}_2$ <sup>11, 12</sup> and  $\text{SiO}_2\text{-SiO}_2$ <sup>53</sup> (with surface modification for charge reversion) multilayers.

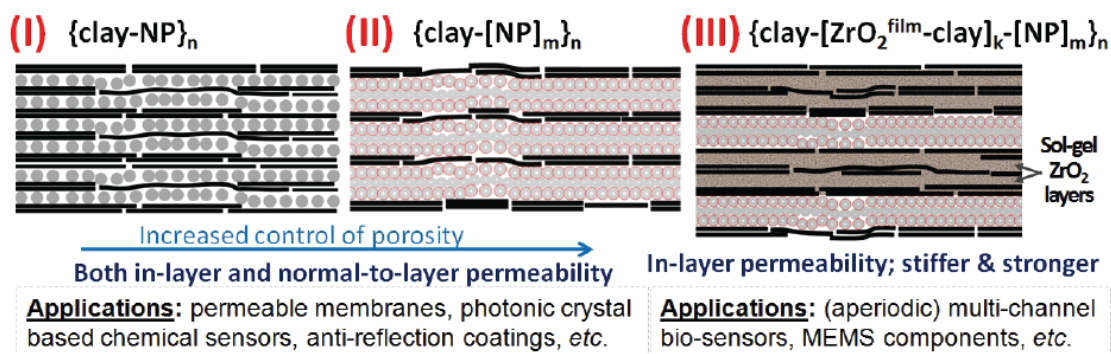


**Figure 33.** Three proposed nanostructures with an increased complexity.

This chapter documented our recent effort to synthesize yet another new type of nanoclay-nanoparticle multilayers or  $\{\text{clay-NP}\}_n$ , via LbL assembly of positively charged nanoparticles and negatively charged nanoclays (Figure 33 (I)). Then, we further demonstrated the synthesis of two more complex multilayers,  $\{\text{clay-[NP]}_m\}_n$  and  $\{\text{clay-[ZrO}_2^{\text{film-clay}}]_k\text{-[NP]}_m\}_n$ , as schematically shown in Figure 33 (II) and (III). Potential applications of such multilayers will be discussed in Chapter. 8.

We also investigated effects of the pH of suspensions on the growth of nanoclay-nanoparticle multilayers, and the key results were documented in Appendix C.

## 2. Experimental

**Materials.** Cerium (IV) oxide (< 25 nm), anatase titanium (IV) oxide (< 25 nm), and aluminum oxide (< 50 nm) nanoparticles were purchased from Sigma-Aldrich (St. Louis,



MO). Montmorillonite (cloisite Na<sup>+</sup>) was purchased from Southern Clay Products (Gonzales, TX).

**Suspensions.** Approximately, 0.0225 g nanoparticles were dispersed into 75 ml deionized water to prepare a 0.03 wt. % nanoparticle suspension. The suspension was stirred for 20 minutes with a magnet, and ultrasonicated for 20 minutes. NaOH (0.01 M) or HCl (1 N) was added into the suspension to change the pH. The suspension was further ultrasonicated for 20 minutes before usage. A nanoclay suspension (0.5 wt. %) was prepared by dispersing 5 g MMT into 1 L deionized water. The suspension was vigorously stirred one week and settled for one day, before the supernatant of the suspension was used to synthesize multilayers.

**Multilayer synthesis.** Nanoclay-nanoparticle multilayers were prepared using Si/SiO<sub>2</sub> substrates (which were cleaned using the same procedure described in prior chapters) by repeating the following four steps periodically. First, a substrate was dipped into a nanoparticle suspension and held for 10 minutes. Second, the substrate was rinsed in deionized water for three times (in three beakers; for 2, 1, and 1 minute respectively). Third, the substrate was dipped into a clay suspension and held for 45 seconds. Fourth, the substrate was rinsed twice in deionized water (in two beakers; 1 minute in each beaker).

### 3. Results and Discussions

#### *Type I: {clay-NP}<sub>n</sub>*

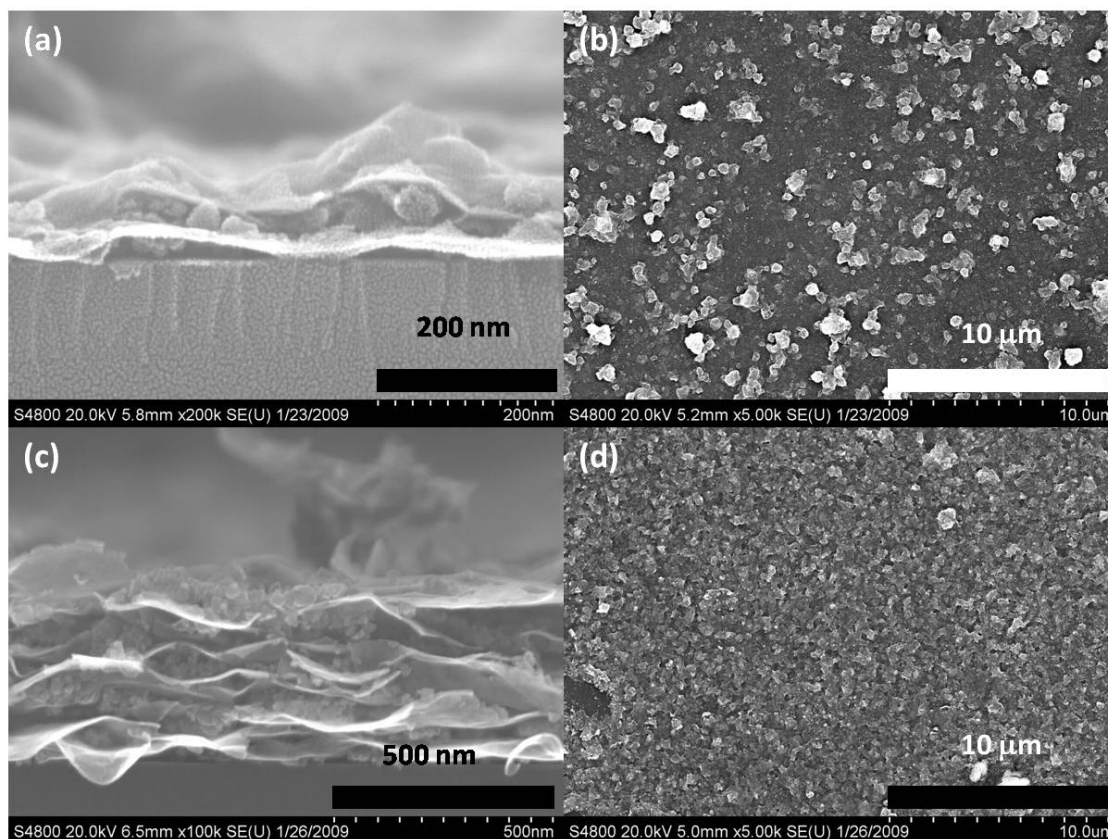


**Figure 34.** Cross-sectional and in-plane SEM images of (a) and (b) {MMT-TiO<sub>2</sub>}<sub>n</sub> and (c) and (d) {MMT-CeO<sub>2</sub>}<sub>n</sub> multilayers.

First, we prepared nanoclay-nanoparticle multilayers with a simple architecture: {clay-NP}<sub>n</sub>, where *n* is number of deposition cycles. Positively charged TiO<sub>2</sub> and CeO<sub>2</sub> nanoparticles were selected. The point of zero charge (PZC) of TiO<sub>2</sub> (anatase and rutile) is ~ 5.9<sup>125</sup>, and the PZC of CeO<sub>2</sub> is ~ 8.1<sup>126</sup>. Thus, the pH of TiO<sub>2</sub> and CeO<sub>2</sub>

suspensions was controlled to be  $\sim 2.4$ , which was far below the PZC of either oxide, to obtain positively charged nanoparticles.

Representative SEM images of the synthesized  $\{\text{MMT-TiO}_2\}_n$  and  $\{\text{MMT-CeO}_2\}_n$  multilayers are shown in Figure 34. Both multilayers show layered structures, where the nanoparticles between layers of nanoclays are clear visible. The estimated thickness is  $\sim 32$  nm per deposition cycle for  $\{\text{MMT-TiO}_2\}_n$  and  $\sim 36$  nm per deposition cycle for  $\{\text{MMT-CeO}_2\}_n$ . These are consistent with the size of  $\text{TiO}_2$  ( $< 25$  nm) and  $\text{CeO}_2$  ( $< 25$  nm) nanoparticles, assuming the thickness of MMT layers is  $\sim 8$ - $10$  nm (similar to that in  $\{\text{MMT-sol gel ZrO}_2\}$  multilayers). The results indicate that about one layer of nanoparticles were adsorbed/deposited in each deposition cycle. The  $\{\text{MMT-CeO}_2\}_n$  multilayer exhibits a more uniform surface, as shown in Figure 34d.

**Type II:  $\{\text{clay-[NP]}_m\}_n$**

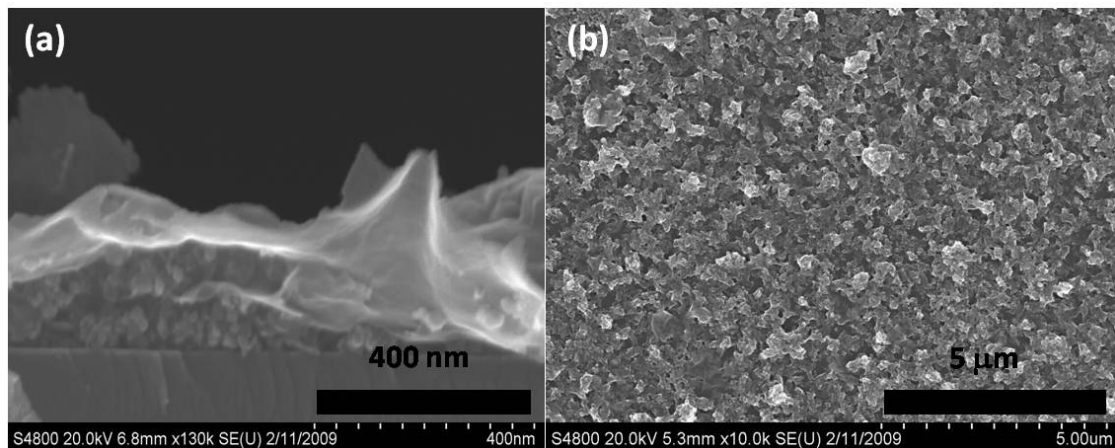


**Figure 35.** (a) Cross-sectional and (b) in-plane SEM images of  $\{\text{MMT-}((\text{CeO}_2\text{-TiO}_2)_2\text{-CeO}_2)\}_n$  multilayers.

Both positively and negatively charged nanoparticles are needed to form a more complex multilayer  $\{\text{clay}-[\text{NP}]_m\}_n$ , where multiple layers of nanoparticles (with opposite charges) are deposited in each cycle. The targeted structure is schematically shown in Figure 33 (II). To achieve this structure, we set the pH of both  $\text{TiO}_2$  and  $\text{CeO}_2$  suspensions to be  $\sim 7$ , which was smaller than PZC of  $\text{CeO}_2$  and greater than PZC of  $\text{TiO}_2$ . Thus  $\text{CeO}_2$  nanoparticles were positively charged and  $\text{TiO}_2$  nanoparticles were negatively charged. Then we synthesized  $\{\text{MMT}-((\text{CeO}_2-\text{TiO}_2)_2-\text{CeO}_2)\}_n$  multilayers by depositing three layers of  $\text{CeO}_2$  and two layers of  $\text{TiO}_2$  nanoparticles in each deposition cycle. Representative SEM images are shown in Figure 35. This  $\{\text{MMT}-((\text{CeO}_2-\text{TiO}_2)_2-\text{CeO}_2)\}_n$  multilayer shows layered structures, and it is clear that multiple layers of nanoparticles have been deposited between two layers of MMT. The estimated thickness is  $\sim 82$  nm per deposition cycle. Assuming the MMT layer is  $\sim 8-10$  nm, the total thickness of  $\text{CeO}_2$  and  $\text{TiO}_2$  nanoparticles is  $\sim 70-75$  nm, which is about 3 times of the particle size ( $\sim 25$  nm for both  $\text{CeO}_2$  and  $\text{TiO}_2$ ). Since the targeted structure is  $\{\text{MMT}-((\text{CeO}_2-\text{TiO}_2)_2-\text{CeO}_2)\}_n$ , this result indicates that  $\sim 0.6$  monolayer of nanoparticles are deposited in each dip. This multilayer also exhibits a fairly uniform surface, as shown in Figure 35 (b).

**Type III:**  $\{\text{clay}-[\text{ZrO}_2^{\text{film}}-\text{clay}]_k-[\text{NP}]_m\}_n$

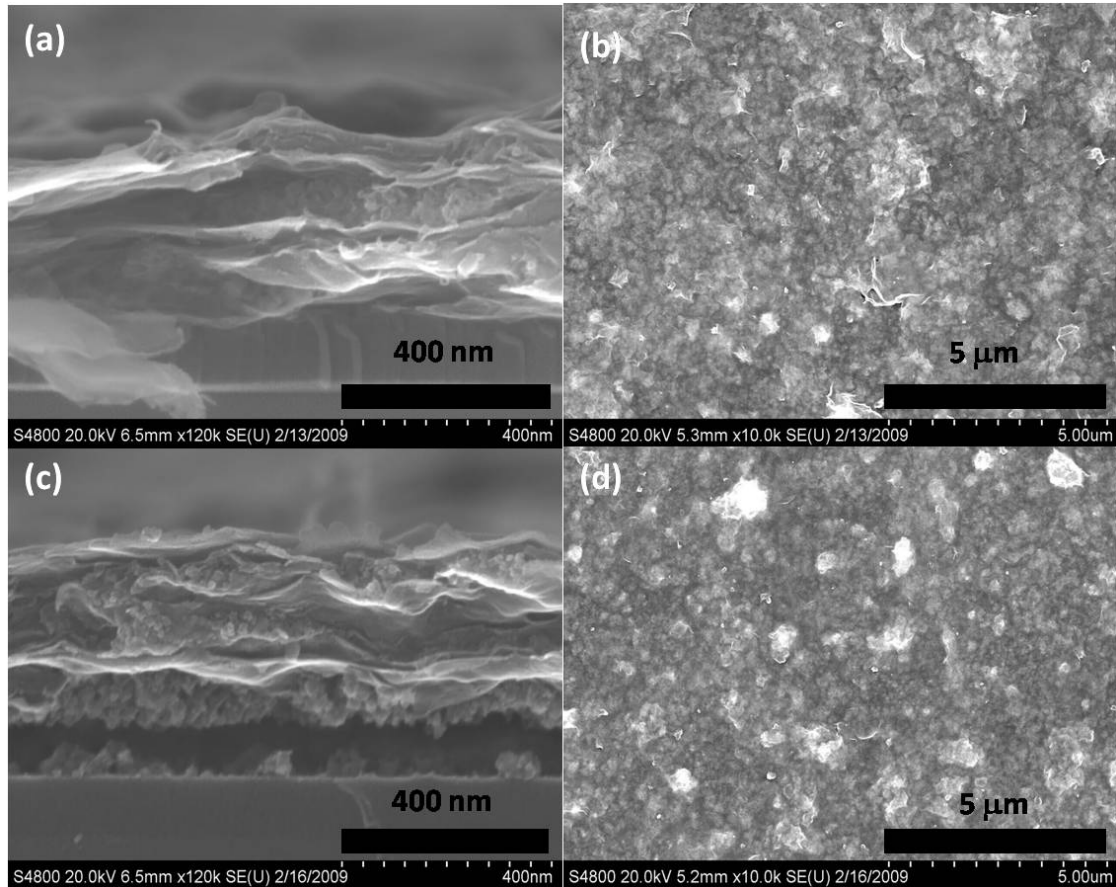


**Figure 36.** Cross-sectional and in-plane SEM images of (a) and (b): as-deposited and (c) and (d): annealed  $\{(\text{CeO}_2\text{-TiO}_2)_2\text{-CeO}_2\text{-(MMT-ZrO}_2)_2\text{-MMT}\}_n$  multilayers.

Finally, we incorporated sol-gel  $\text{ZrO}_2$  into the multilayer structure to synthesize  $\{(\text{CeO}_2\text{-TiO}_2)_2\text{-CeO}_2\text{-(MMT-ZrO}_2^{\text{sol-gel film}})_2\text{-MMT}\}_n$  multilayers; the targeted structure was schematically shown in Figure 33 (III). This multilayer was synthesized by using 0.15 M zirconium acetate to make the sol-gel films in the  $(\text{MMT-ZrO}_2^{\text{sol-gel film}})_2\text{-MMT}$  part of the multilayer structure, following the procedure described in Chapter 5. The other

deposition procedure was the same as that for making  $\{\text{MMT}-((\text{CeO}_2-\text{TiO}_2)_2-\text{CeO}_2)\}_n$  multilayers. The representative SEM images are shown in Figure 36. The as-deposited multilayer shows layered structures (Figure 36 (a)). The estimated thickness is about 140 nm per deposition cycle, which agrees reasonably with the targeted structure. We further annealed the as-deposited multilayers at 200 °C for 1 hour to dehydrate. The annealed multilayers still exhibit a layered structure (Figure 36(c)) but the thickness is reduced to ~ 100 nm per deposition cycle. Both as-deposited and annealed multilayers exhibit uniform and smooth surfaces (Figure 36 (b) and (d)).

## CHAPTER SEVEN

### AN EXPLORATORY STUDY OF SYNTHESIS OF OTHER TYPES MULTILAYERS

This chapter documented an exploratory study of synthesis of several other types of multilayers. One of the objectives is to demonstrate that our methodology of using sol-gel oxides (instead of polymers or polyelectrolytes) as structural “glues” to build multilayers can be extended to include other metal oxides. In addition, we also explored the feasibility of synthesizing several other types of novel structures, including MMT-ionic liquid, polymer-oxide multilayer, and carbon nanotube-oxide multilayers.

#### 1. MMT-SnO<sub>2</sub> Multilayers

##### 1.1 Introduction

Tin oxide (SnO<sub>2</sub>) is a transparent oxide and a wide bandgap *n*-type semiconductor<sup>127</sup>. Because of its good optical transparency in visible and near IR regions, SnO<sub>2</sub> finds applications in photovoltaic cells, liquid crystal displays, and photo detectors<sup>128</sup>. Sol-gel methods have been used to prepare tin oxide. Li *et al.* dissolved SnCl<sub>2</sub>·2H<sub>2</sub>O into a mixture of ethanol and hydrochloric acid and aged the solution to obtain tin oxide sol<sup>129</sup>. Maddalena<sup>130</sup>, Terrier<sup>128, 131</sup>, Benrabah<sup>127</sup>, Ota<sup>132</sup>, Bhat<sup>133</sup>, Zhang<sup>134</sup>, and Banerjee<sup>135</sup> prepared tin oxide sol similarly by dissolving tin salts (SnCl<sub>2</sub> or SnCl<sub>4</sub>) into alcohol (ethanol, isopropyl alcohol, or propanol alcohol) solutions. Dopants, such as F, Sb, Zn and In, were added when needed.

In this study,  $\text{SnCl}_2 \cdot 2\text{H}_2\text{O}$  was selected as the tin oxide precursor. We successfully prepared MMT- $\text{SnO}_2$  multilayers by an LbL method.

### ***1.2 Experimental***

A tin chloride solution (0.05 M) was prepared by dissolving 1.422 g tin(II) chloride (Sigma-Aldrich, St. Louis, MO) into 75 ml deionized water and adding 4 ml HCl (1 N) dropwise. A nanoclay suspensions was prepared by adding a sodium hexametaphosphate ( $(\text{NaPO}_3)_6$ ) solution (5 g/L) dropwise into a 0.4 wt. % MMT suspension with a volumetric ratio of 1:100. As-deposited MMT- $\text{SnO}_2$  multilayers were synthesized by dipping a pre-cleaned silicon substrate into the tin chloride solution and the nanoclay suspension alternatively (without inter-rinsing) for 30 cycles.

### ***1.3 Results and discussion***

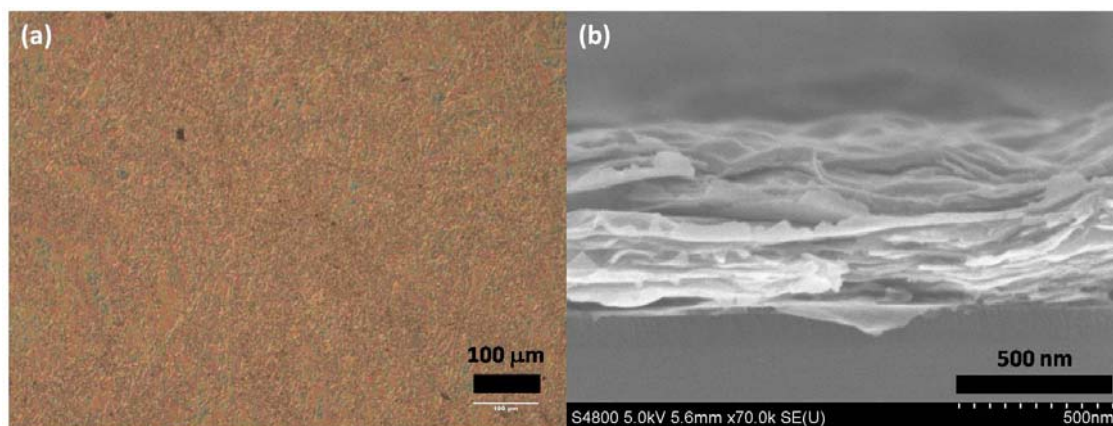


**Figure 37.** (a) An optical micrograph and (b) a cross-sectional SEM image of MMT- $\text{SnO}_2$  multilayers.



A MMT-SnO<sub>2</sub> multilayer showed a smooth and uniform surface (Figure 37 (a)). The multilayer was ~ 500 nm thick and exhibited a layered structure, as shown in Figure 37(b). An EDS spectrum of the as-deposited multilayer (Figure 38) showed strong Sn peaks, which confirmed the existence of Sn in the multilayers. Presumably, the tin oxide deposition occurred via a condensation of oxohydroxo polymeric species<sup>136</sup>

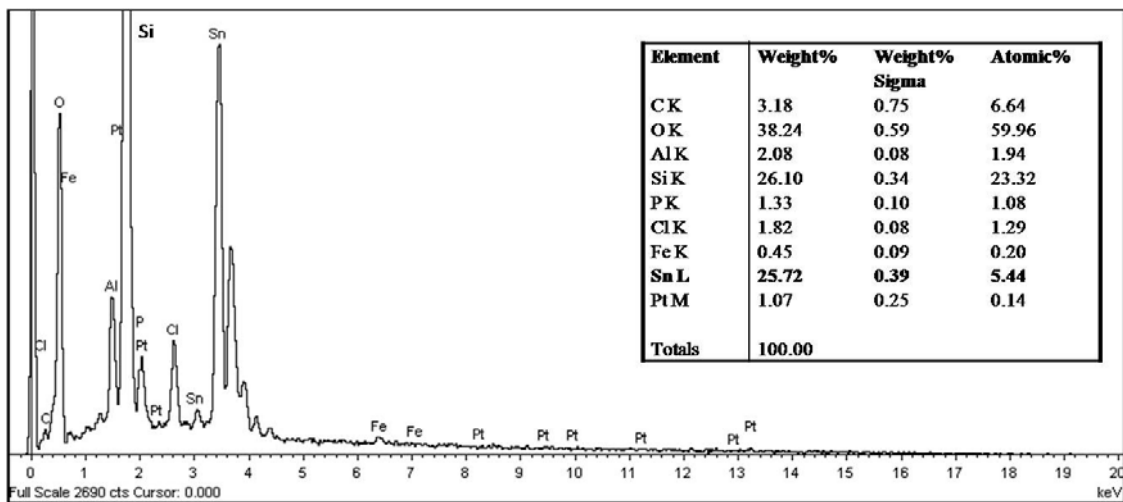
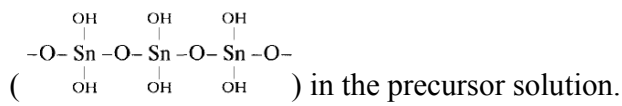


**Figure 38.** An EDS spectrum of a MMT-SnO<sub>2</sub> multilayer. The inset is a table of the apparent (measured) elemental composition.

## 2. MMT-ZnO Multilayers

### 2.1 Introduction

Zinc oxide (ZnO) is a transparent oxide and a wide bandgap (3.37 eV) semiconductor. Because of its optical transparency, zinc oxide is used as a conducting electrode for display devices and solar cells when doped with Al or In<sup>137</sup>. Other

applications of ZnO include materials for room-temperature ultraviolet lasers, field-effect transistors, photo detectors, and gas sensors. ZnO thin films can be prepared by sputtering, molecular beam epitaxy, chemical vapor deposition, pulsed laser deposition, spray pyrolysis and sol-gel methods<sup>138</sup>. Among all the synthesis methods, the sol-gel method is a low-cost and low-temperature processing. Furthermore it is easy to control compositions, and large area coatings can be made. Zinc oxide precursor solutions (sol) were usually prepared by mixing inorganic zinc salts with alcohols. O'Brien *et al.* dissolved zinc acetate ( $Zn(OAc)_2$ ) in isopropanol ( $(CH_3)_2CHOH$ ), added monoethanolamine (MEA,  $H_2NCH_2CH_2OH$ ) as a sol stabilizer, stirred this mixture to obtain sol, and prepared zinc oxide films with spin coating<sup>138</sup>. Dutta *et al.* mixed zinc acetate dihydrate ( $Zn(OAc)_2 \cdot 2H_2O$ ), isopropanol, and diethanolamine (DEA) to obtain sol<sup>139</sup>. Zhu<sup>140</sup>, Lee<sup>141</sup>, Srinivasan<sup>142</sup>, and Ohyama<sup>143</sup> mixed zinc acetate dihydrate, 2-methoxyethanol and MEA to obtain sol. Znaidi *et al.* mixed zinc acetate dihydrate, ethanol and MEA to obtain sol<sup>144</sup>.

In this study, zinc acetate dihydrate ( $Zn(OAc)_2 \cdot 2H_2O$ ) was used as the zinc oxide precursor. We prepared MMT-ZnO multilayers by an LbL method with only a limited success.

## **2.2 Experimental**

A zinc acetate solution (0.05 M) was prepared by dissolving 1.646 g zinc acetate dihydrate (Sigma-Aldrich, St. Louis, MO) into 75 ml deionized water. A nanoclay

suspension was prepared by adding a sodium hexametaphosphate ((NaPO<sub>3</sub>)<sub>6</sub>) solution (5 g/L) dropwise into a 0.4 wt. % MMT suspension with a volumetric ratio of 1:100. An as-deposited nanoclay-zinc oxide multilayer was synthesized by dipping a pre-cleaned silicon substrate into the zinc acetate precursor solution and the nanoclay suspension alternatively (without inter-rinsing) for 30 cycles.

### 2.3 Results and discussions

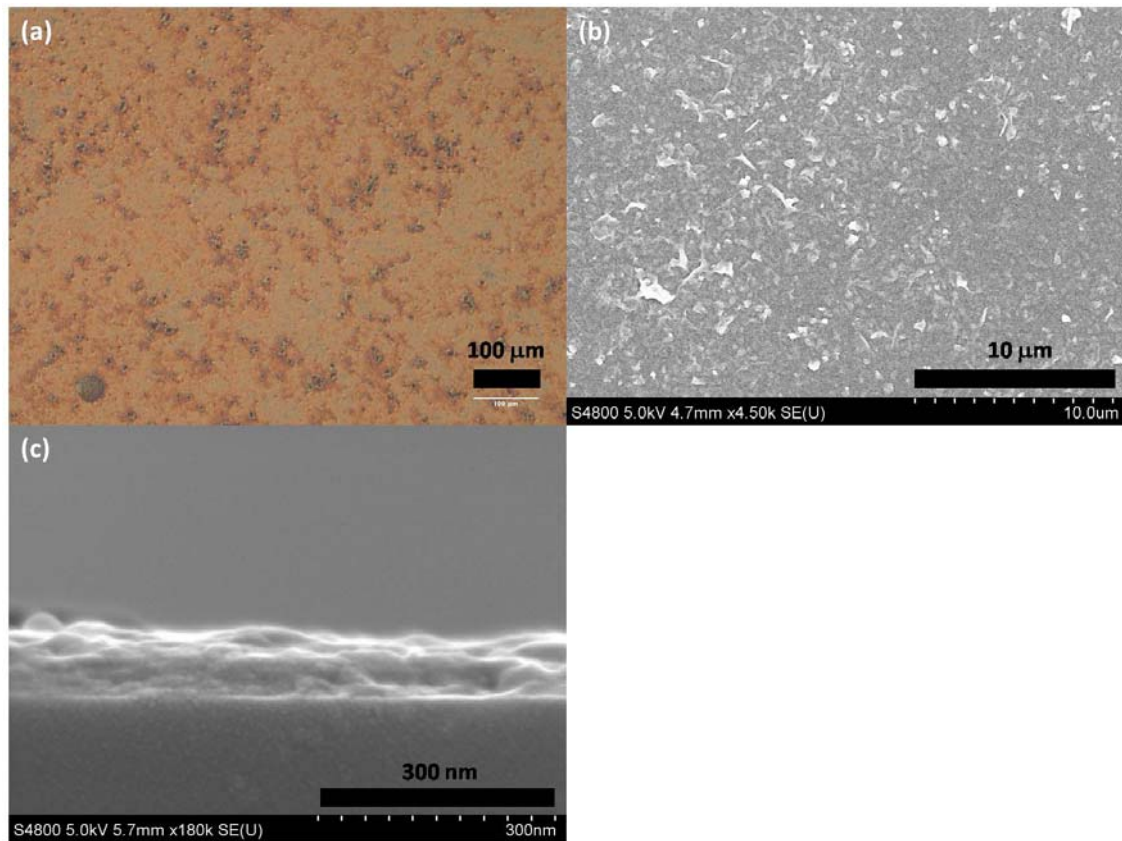


**Figure 39.** (a) An optical micrograph and (b) in-plane and (c) cross-sectional SEM images of a MMT-zinc oxide multilayer.

As-deposited nanoclay-zinc oxide “multilayers” showed no clear layered structure (Figure 39(c)). An EDS spectrum (Figure 40) showed Zn peaks, which confirmed the existence of zinc (~ 0.2 at. %) within the composite film. The film had a fairly smooth surface (as shown in Figure 39(a) and (b)), and it was uniform in thickness (Figure 39(c)). The thin thickness (less than 100 nm) and the lack of a layered structures are probably due to weak interactions between zinc oxide sol and nanoclays.

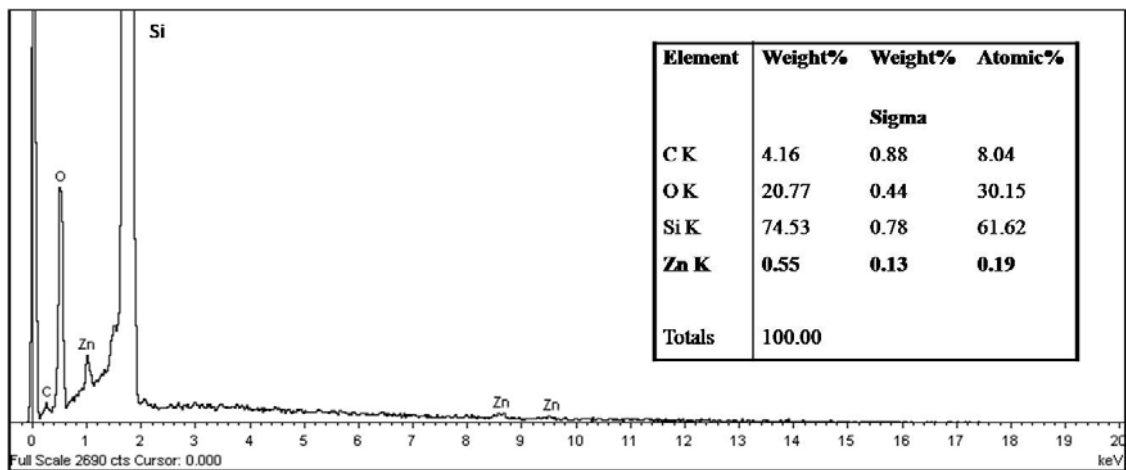


**Figure 40.** An EDS spectrum of MMT-ZnO multilayer. The inset is a table of measured elemental composition.

### 3. MMT-CeO<sub>2</sub> Multilayers

#### 3.1 Introduction

Cerium oxide (CeO<sub>2</sub>) is a wide bandgap (~ 3.2 eV) semiconductor. Applications of cerium oxide include: passive electrode materials because of its good visible transparencies and strong ultraviolet absorbency<sup>145</sup>, electrolyte materials for solid oxide fuel cells because of its high ionic conductivity<sup>146</sup>, catalysis materials for automotive

emission-control because of its high oxygen storage capacity, and substrate materials of mesoporous membranes because of its porous structures<sup>147</sup>.

Sol-gel methods were used to prepare cerium oxide films. The two inorganic cerium salts were used as cerium oxide precursors. One was cerium nitrate, which was either mixed with alcohols or bases. Guo *et al.* dissolved cerium nitrate hexahydrate ( $\text{Ce}(\text{NO}_3)_3 \cdot 6\text{H}_2\text{O}$ ) in a water-ethanol solution, added  $\text{HNO}_3$ , and used citric acid and PEG as chelating and cross-linking agents<sup>148</sup> to obtain sols. Chen *et al.* dissolved  $\text{Ce}(\text{NO}_3)_3 \cdot 6\text{H}_2\text{O}$  in acetylacetone ( $\text{C}_5\text{H}_8\text{O}_2$ ), mixed with 2-methoxyethanol and glycol, and prepared cerium oxide films by spin coating<sup>149</sup>. Epifani *et al.* dissolved  $\text{Ce}(\text{NO}_3)_3 \cdot 6\text{H}_2\text{O}$  in methanol, mixed with acetylacetone, and added  $\text{NH}_4\text{OH}$  dropwise to prepare sols<sup>150</sup>. Rane<sup>147</sup> and Huang<sup>146</sup> dissolved  $\text{Ce}(\text{NO}_3)_3 \cdot 6\text{H}_2\text{O}$  in distilled water, precipitated the solution with  $\text{NH}_4\text{OH}$ , and peptized the precipitation with  $\text{HNO}_3$  to obtain sols. Wu *et al.* added urea ( $(\text{NH}_2)_2\text{CO}$ ) to cerium nitrate solutions and obtained sols by aging<sup>151</sup>. The other cerium oxide precursor was cerium chloride. Verma *et al.* added citric acid, with a controlled quantity, into a solution of cerium chloride heptahydrate ( $\text{CeCl}_3 \cdot 7\text{H}_2\text{O}$ ) and ethanol to obtain sols<sup>145</sup>. Chen *et al.* dissolved cerium chloride hexahydrate ( $\text{CeCl}_3 \cdot 6\text{H}_2\text{O}$ ) and zirconium oxychloride octahydrate in anhydrous ethanol to obtain sols with aging, and prepared ceria stabilized zirconia films by dip coating<sup>152</sup>. Murali added acrylamide (*N,N* bis methylene acrylamide) and ammonium persulphate to cerium chloride solutions to obtain sols<sup>153</sup>.

In this study, cerium chloride ( $\text{CeCl}_3$ ) and cerium nitrate ( $\text{Ce}(\text{NO}_3)_3$ ) were used as two different cerium oxide precursor solutions. We prepared MMT- $\text{CeO}_2$  multilayers using both precursors by an LbL method with a limited success.

### ***3.2 Experimental***

A cerium chloride solution (0.05 M) was prepared by dissolving 1.397 g cerium chloride heptahydrate (Sigma-Aldrich, St. Louis, MO) into 75 ml deionized water. A cerium nitrate solution (0.05 M) was prepared by dissolving 1.628 g cerium nitrate hexahydrate (Sigma-Aldrich, St. Louis, MO) into 75 ml deionized water. A nanoclay suspension was prepared by adding a sodium hexametaphosphate ( $(\text{NaPO}_3)_6$ ) solution (5 g/L) dropwise into a 0.4 wt. % MMT suspension with a volumetric ratio of 1:100. As-deposited MMT-cerium oxide multilayers were synthesized by dipping pre-cleaned silicon substrates into cerium precursor solutions (cerium chloride or cerium nitrate) and the nanoclay suspensions (without inter-rinsing) for 30 cycles.

### 3.3 Results and discussions

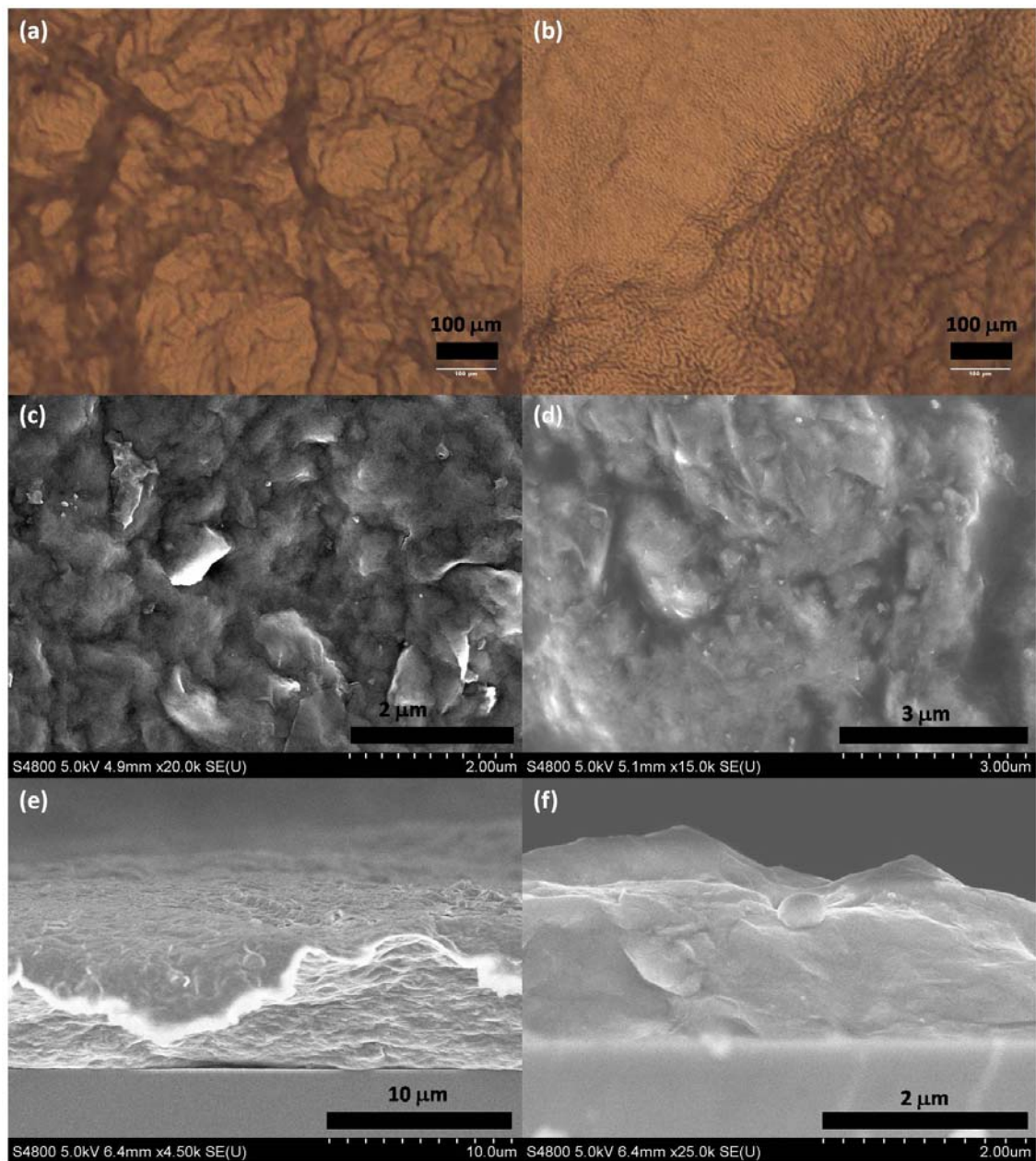


**Figure 41.** Optical micrographs and in-plane and cross-sectional SEM images of MMT-CeO<sub>2</sub> multilayers made using cerium chloride (a, c, e) or cerium nitrate (b, d, f) precursor solutions.

As-deposited MMT-CeO<sub>2</sub> multilayers made with CeCl<sub>3</sub> and Ce(NO<sub>3</sub>)<sub>3</sub> precursor solutions showed no clear layered structures (Figure 41 (e) and (f)). EDS spectra of both MMT-CeO<sub>2</sub> films confirmed the presence of cerium (Figure 42). Both films were micrometer thick and showed rough surfaces, with clay platelets on top (Figure 41).

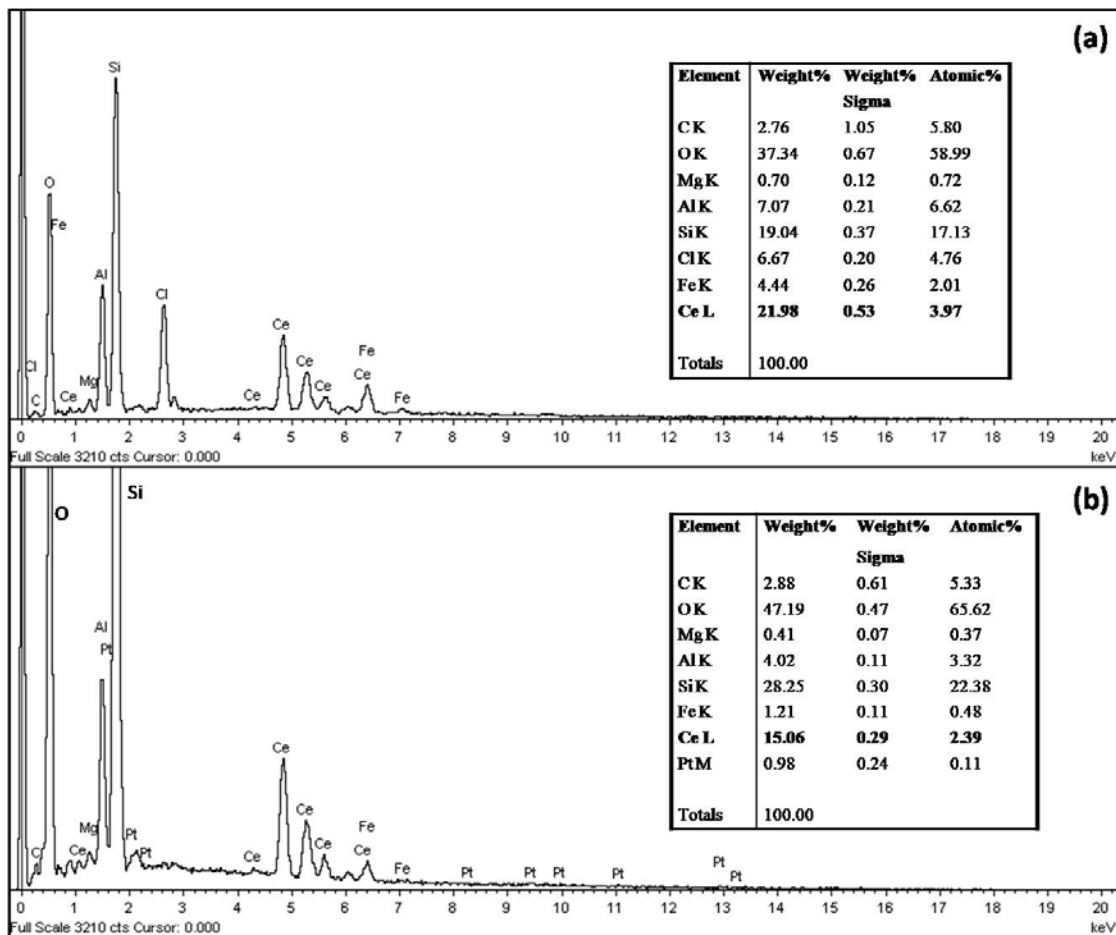


**Figure 42.** EDS spectra of as-deposited MMT-cerium oxide multilayers made using (a) cerium chloride and (b) cerium nitrate precursor solutions. The insets are tables of measured elemental compositions.



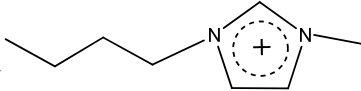
## 4. MMT-Ionic Liquid Multilayers

### 4.1 Introduction

An ionic liquid, which usually has a melting temperature below 100 °C, is one type of ionic salts. Cations of ionic liquids are organics, such as include 1-alkyl-3-methylimidazolium, N-alkylpyridinium, tetraalkylammonium, and tetraalkylphosphonium. Anions of ionic liquids can be either organics or inorganics, such as hexafluorophosphate, tetrafluoroborate, trifluoromethylsulfonate, trifluoroethanoate, ethanoate, nitrate, and halide<sup>154</sup>. Anion types affect the water solubility of ionic liquids: ionic liquids with halides or nitrate are soluble; ionic liquids with PF<sub>6</sub><sup>-</sup> or AsF<sub>6</sub><sup>-</sup> are insoluble<sup>155</sup>. Applications of ionic liquids include: catalysis materials<sup>156</sup>, intercalation materials for kaolinite<sup>157, 158</sup>, and green solvents, which can replace volatile and toxic polar solvents because of their low vapor pressures.

In this study, a 1-butyl-3-methylimidazolium chloride ([BMIM]Cl) was used as cationic solution. We prepared MMT-ionic liquid multilayers by an LbL method.

### 4.2 Experimental

A [BMIM]Cl ( , Cl<sup>-</sup>) solution (0.05 M) was prepared by dissolving 0.655 g [BMIM]Cl (Sigma-Aldrich, St. Louis, MO) into 75 ml deionized water. A nanoclay suspension was prepared by adding a sodium hexametaphosphate ((NaPO<sub>3</sub>)<sub>6</sub>) solution (5 g/L) dropwise into a 0.4 wt. % MMT suspension with a volumetric ratio of 1: 00. An as-deposited MMT-ionic liquid multilayer was synthesized

by dipping a pre-cleaned silicon substrate into the [BMIM]Cl precursor solution and the clay suspension for 30 cycles.

#### 4.3 Results and discussions

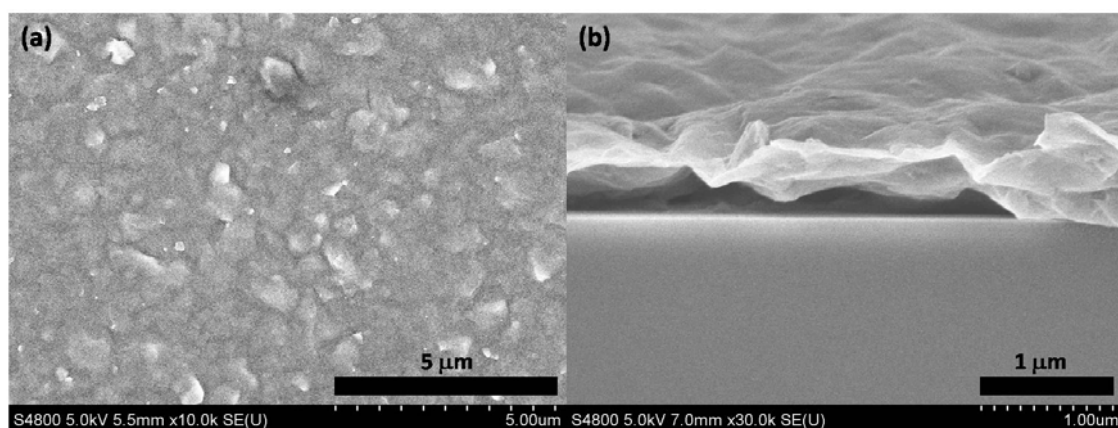


**Figure 43.** (a) In-plane and (b) cross sectional SEM images of MMT-ionic liquid multilayers.

An as-deposited MMT-ionic liquid multilayer showed no clear layered structure (Figure 43(b)). The as-deposited film exhibited a smooth surface and good thickness uniformity (Figure 43). The role of organic cation ( $[\text{BMIM}]^+$ ) in the formation of films should be studied further. Strong electrostatic interactions between  $[\text{BMIM}]^+$  and negative MMT surfaces are possible.

## 5. Polymer-Oxide Multilayers and Carbon Nanotube-Zirconia Multilayers

### 5.1 Introduction

Polymer-oxide hybrid materials are designed to have enhanced mechanical, thermal, or electrical properties. For example, a polymer-oxide composite made of polyaniline (conductive polymers) and  $V_2O_5$  showed better electrochemical responses than both components, which made this composite a good cathode material for Li batteries with a better reversibility and an increased Li capacity<sup>159</sup>. Polymer-oxide composites made of proton conductive polymers and oxides (e.g.,  $SiO_2$ ) have better chemical and thermal stabilities, which are good for applications as proton exchange membranes (PEM) for PEM fuel cells<sup>160</sup>.

Single wall carbon nanotubes (SWCNT) have cylindrical structures and high length-to-diameter ratios. Unique features of SWCNT include superior mechanical properties, e.g., an Young modulus of 1 TPa and a shear modulus of 450 GPa<sup>161</sup>. Depending on its diameter and helicity, an SWCNT can exhibit either metallic or semiconductive electrical conductivities<sup>162</sup>. Mamedov *et al.* prepared PEI-SWCNT composites by a LbL method, and the composites showed an increased mechanical property: a tensile strength close to that of a hard ceramic material<sup>163</sup>.

In this study, we used an LbL method to prepared polymer-oxide multilayers with zirconium acetate, PSS, and PEI. We also prepare a SWCNT- $ZrO_2$  multilayer.

## ***5.2 Experimental***

A polymer-oxide multilayer (with a nominal structure of  $\{\text{ZrO}_2/\text{PSS}/\text{PEI}\}_{10}$ ) was synthesized by dipping a pre-cleaned silicon substrate into a 0.06 M zirconium acetate (ZA) solution, a 1.5 mg/ml sodium polystyrene sulfonate (PSS) polyanion solution, and a 1.5 mg/ml polyethylenimine (PEI) polycation solution in an order of ZA/PSS/PEI/PSS/PEI/PSS. The deposition cycles were repeated 10 times.

SWCNT suspensions were generously given by Dr. Pu-Chun Ke's group (Physics Department, Clemson University). The dispersion agent of SWCNT suspensions is sodium dodecyl sulfate ( $\text{NaC}_{12}\text{H}_{25}\text{SO}_4$ , SDS). A SWCNT-zirconia composite film was synthesized by repeatedly dipping a pre-cleaned silicon substrate into a 0.15 M zirconium acetate solution and a 10.5 mg/L SWCNT suspension for 30 cycles.

## ***5.3 Results and discussions***

An as-deposited polymer-oxide multilayer showed no layered structures (Figure 44 (b)). An EDS spectrum of the composite film (Figure 44(c)) indicated the presence of zirconium ( $\sim 0.7$  at. %). The film was  $\sim 300$  nm thick; some pores ( $\sim 10$ - $100$  nm) can be observed on its surface (Figure 44(a)). The results suggested that this polymer-oxide multilayer has a possible porous structure, which may find applications as a membrane material.

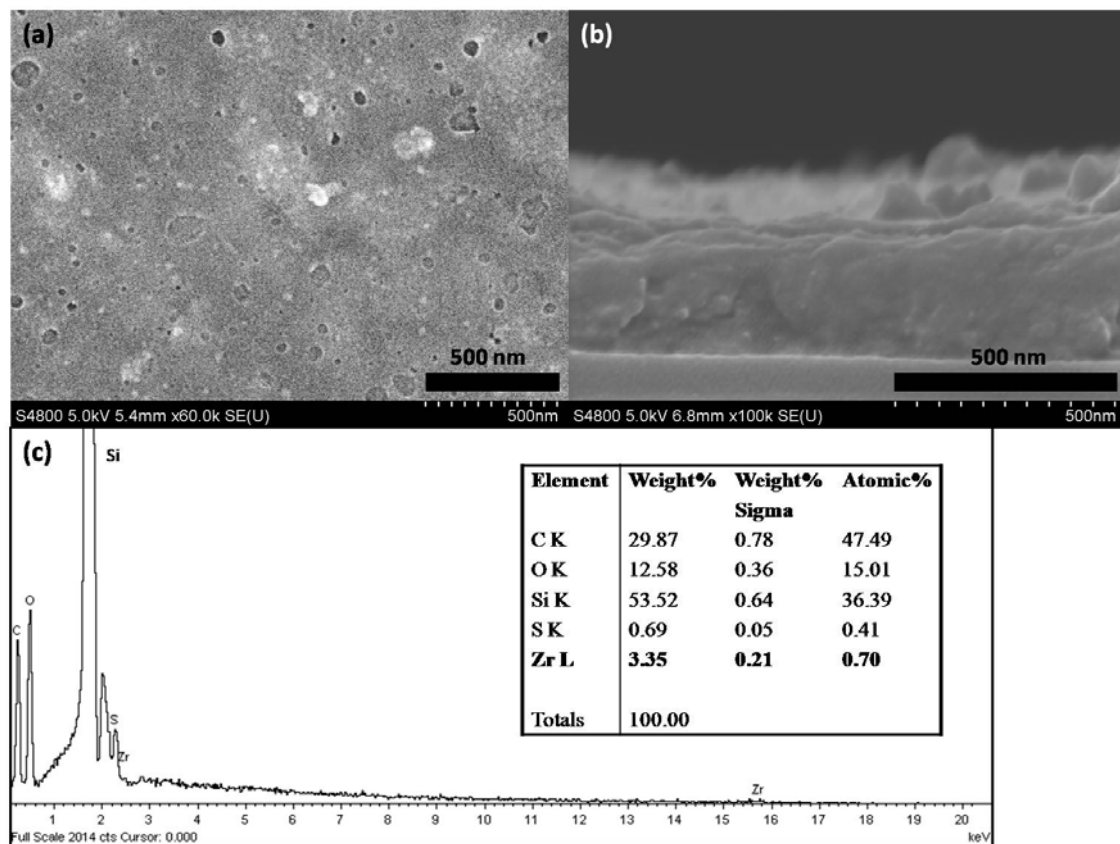


**Figure 44.** (a) In-plane and (b) cross-sectional SEM images, and (c) an EDS spectrum of polymer-oxide multilayers.

The SWCNT-zirconia film was uniform to naked eyes, but it showed a granular structure under an optical microscope (Figure 45). The “grain” size is similar to the length of SWCNT. Further optimization, such as functionalizing SWCNT with charged groups, is necessary to obtain more uniform multilayers.

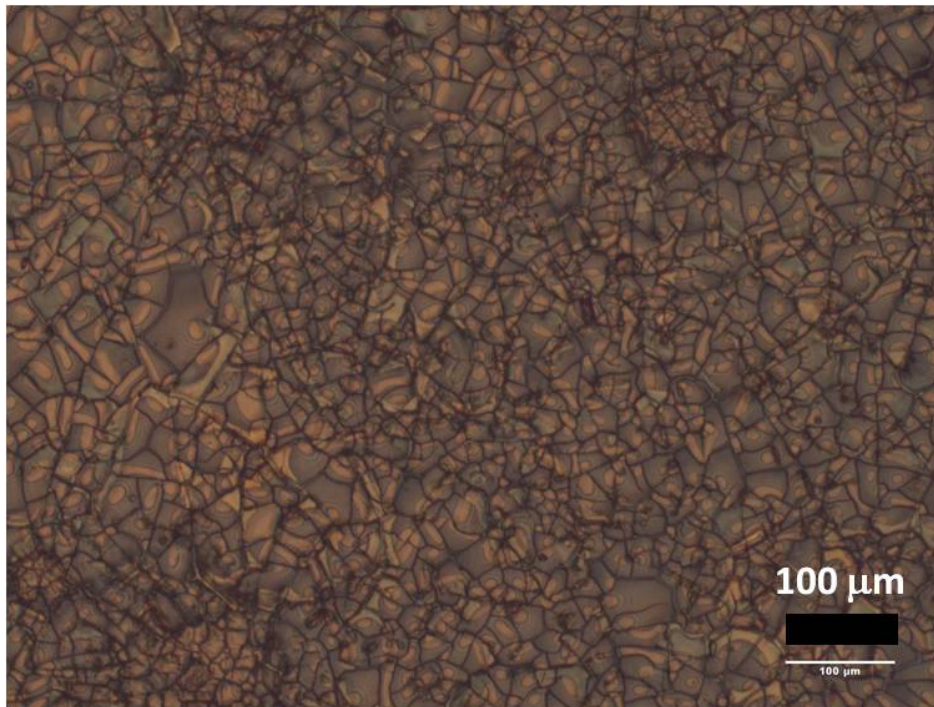


**Figure 45.** An optical micrograph of a SWCNT-zirconia multilayer.

## CHAPTER EIGHT

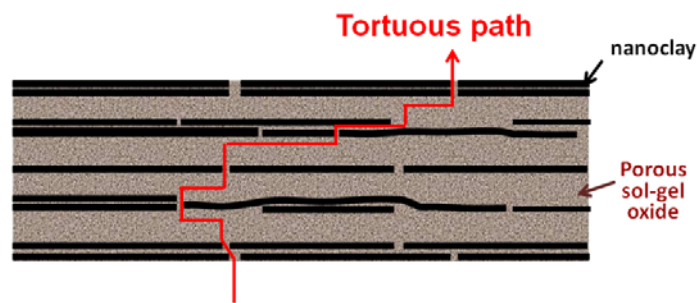
### A DISCUSSION OF POTENTIAL APPLICATIONS

The  $\{\text{MMT}_x\text{-(sol-gel ZrO}_2)\}_n$  and several other types of multilayers described in Chapter 6 and Chapter 7 were synthesized for the first time in our studies. Because of their all inorganic building units and distinct structure, the  $\{\text{nanoclay-(sol-gel oxide)}\}_n$  and  $\{\text{nanoclay-(oxide nanoparticle)}\}_n$  multilayers are expected to have new applications as high-temperature gas membranes, microelectromechanical system (MEMS) structure components, fast ion conductor, sensors, and protective coatings. Although future studies are needed to explore and verify these applications, a few example potential applications are discussed below.

#### **1. High-Temperature Filtering Membranes**

The application of  $\{\text{nanoclay-(sol-gel oxide)}\}_n$  and  $\{\text{nanoclay-(oxide nanoparticle)}\}_n$  multilayers as a class of novel high-temperature filtering membranes with tortuous paths can be envisioned. In general, the inorganic membranes possess high thermal stability, chemical stability in a wide pH range, structural integrity, mechanical strength and stiffness, and long-term durability<sup>164</sup>. More specifically, it is well known that zirconia<sup>165</sup> or zirconia composites<sup>166-169</sup> made by sol-gel processes are good membrane materials bearing nanometer-sized pores. These membranes can be used for high-temperature CO<sub>2</sub> separation<sup>170</sup>, hydrogen production, and purification<sup>164</sup>. In  $\{\text{MMT}_x\text{-(sol-gel ZrO}_2)\}_n$  or other  $\{\text{nanoclay-(sol-gel oxide)}\}_n$  and  $\{\text{nanoclay-(oxide$

nanoparticle) $\}_n$  multilayers, the distinct layered structure and the inclusion of the clay nanoplatelets or other nanosheets as tiny barriers in the structure lead to the formation of tortuous paths throughout the film. The penetrating gas molecules will easily transport through the pore network inside the zirconia, but will be blocked by the nanosheets. As such, permeation of gas molecules is only allowed through the gaps among the clay nanoplatelets, as schematically illustrated in Figure 46. Fine processing controls can be used to regulate the pore size in the zirconia layer and the gaps among nanoclay platelets to modify gas permeability and selectivity of the films. Furthermore, in {nanoclay-(oxide nanoparticle) $\}_n$  multilayers, even though the surface charges of nanoclays are always negative, edge charges of nanoclays can be reversed (to be positive) via reducing pH (to  $< \sim 7$ ) to control the vertical permeability (via repelling the positively charged nanoparticles). This novel concept is schematically illustrated in Figure 46 (b). Finally, different sol-gel oxides can be conveniently, flexibly incorporated into a unified, multi-phase nanoclay-based multilayer, allowing the integration of multiple functionalities into a single membrane.



(a)



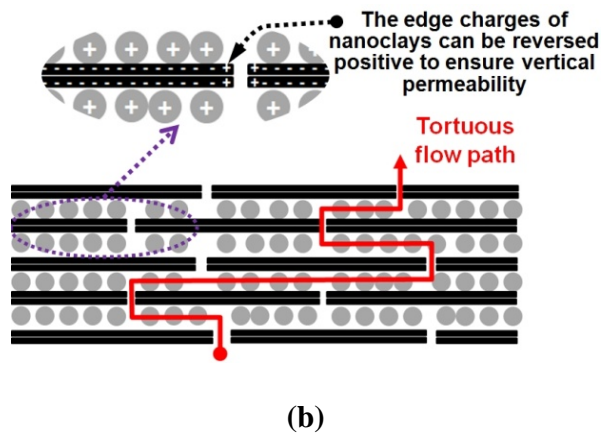


**Figure 46.** A conceptual illustration for the multilayers used as filtering membranes with tortuous paths.

## 2. Micro-Cantilevers

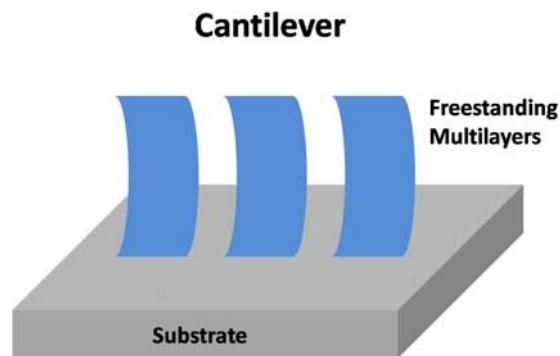


**Figure 47.** Schematic of micro-cantilevers made of freestanding MMT-zirconia multilayers.

In addition to coatings, these nanoclay-sol gel oxide multilayers can find applications in MEMS components or sensors/actuators. Freestanding MMT-zirconia multilayers, which have been synthesized in our study (Figure 25 in Chapter 5), can be used as micro-cantilevers, an important sensing unit in these sensors (Figure 47). Other

similar ultrathin cantilever sensors have already been developed by using polymer-ceramic nanocomposites synthesized by LbL assembly <sup>61</sup>. However, cantilever sensors made of all inorganic nanoclay-oxide multilayers are more suitable for high-temperature applications. Moreover, these all inorganic multilayer cantilevers can possess enhanced dynamic or vibrational properties, when compared with polymer-nanoclay multilayers, as suggested by the inorganic structural components.

### **3. Interface-Enhanced Fast Ionic Conductors**

A high density of interfaces within MMT-zirconia multilayers may enhance their ionic conductivity. Ionic conductors are critical components for fuel cells, batteries, certain chemical filters, solid-state electrolyte reactors, and gas sensors.

In a seminal paper published in *Nature* in 2000 <sup>171</sup>, Sata *et al.* reported a new route to enhance ionic conductivity via interface effects using  $(\text{CaF}_2\text{-BaF}_2)_n$  hetero-multilayers as a model system, and systematic investigations of  $(\text{CaF}_2\text{-BaF}_2)_n$  have been conducted <sup>172, 173</sup>. The interface enhanced ionic conduction phenomenon has also been observed in doped  $(\text{CeO}_2\text{-ZrO}_2)_n$  multilayers <sup>174-176</sup> and thin polycrystalline films of yttrium-stabilized zirconia (YSZ) <sup>177, 178</sup>, Gd-doped  $\text{CeO}_2$  <sup>179</sup>, and lanthanum germanite <sup>180-183</sup>. These multilayers or thin films have been synthesized using sophisticated molecular beam epitaxy (MBE) and pulsed laser deposition (PLD) methods. Furthermore, an economical sol-gel route has been used to make nanocrystalline Y/Sm-doped  $\text{CeO}_2\text{-ZrO}_2$  composite films, which also exhibit enhanced ionic conductivity <sup>184</sup>.

The enhanced ionic conductivity can be attributed to either an increase of ion concentrations due to an electrical double-layer space-charge effect, or an increase of ion mobility at or near interfaces. In the first case, when the distance between two interfaces, e.g., the  $\text{CaF}_2/\text{BaF}_2$  and the  $\text{BaF}_2/\text{CaF}_2$  interface in  $(\text{CaF}_2\text{-BaF}_2)_n$  hetero-multilayers, is close to the Debye length, the space charge regions overlap, increasing  $\text{F}^{-1}$  vacancy concentration<sup>171, 185</sup>. In contrast, another study of single-layers of yttria-stabilized zirconia (with 10%  $\text{Y}_2\text{O}_3$ ) suggested that increased ion mobility at the interface is the major cause of enhanced ionic conductivity<sup>177, 178</sup>. While both mechanisms likely contribute to the enhanced ionic conductivity, to date, quantitatively testing these hypothesized mechanisms remains difficult, partly because the exact amount of interfacial charges is usually unknown.

Although it needs to be confirmed experimentally,  $\{\text{nanoclay-(sol-gel oxide)}\}_n$  has the potential to be a new type of interface-enhanced ionic conductors. First, if the space charge mechanism is valid,  $\{\text{nanoclay-(sol-gel oxide)}\}_n$  can exhibit significantly enhanced ionic conductivity because the large and permanent surface charges of nanoclays. Second, in addition to potentially significant enhancement in ionic conductivity induced by the large surface charges of nanoclays, a unique experimental opportunity for quantitatively testing the hypothesized mechanism is also envisaged, because the interfacial charge density resulted from nanoclays is known and can be further varied. Third, making oxide-clay multilayers via a cost-effective, solution-based method, as originally demonstrated in our study, represents yet another novel idea to manufacture interface-enhanced ionic conductors. Finally, while  $\{\text{nanoclay-(sol-gel$

oxide) $\}_n$  multilayers are potentially a new type of high-temperature interface-enhanced ionic conductors, the {nanoclay-(ionic liquid) $\}_n$  multilayers that are made (and reported in Section 4 of Chapter 7, Figure 43) represents yet another type of low-temperature interface-mediated ionic conductors with applications in different environments.

#### **4. Photonic Clays**

“Photonic clays” or one-dimensional photonic crystals made of spin-coated clay-TiO<sub>2</sub> multilayers have recently been developed as a new type of clay-based chemical sensors<sup>186, 187</sup>. In these photonic clay sensors, adsorption, ion exchange, and interlayer intercalation inside the nanoclays will alter the optical paths and lead to a shift in the Bragg reflection peak and hence the change in color. These photonic clay sensors have already attracted great attention because of their sensitivity and simplicity. Substituting the spin-coated clay layers in the “photonic clays” with the MMT-zirconia multilayers synthesized in this study, or even other derivative nanoclay-ceramic multilayers, can in principle lead to a better control of thickness, composition, periodicity, and nanoporosity. Thus, the effects of adsorption, ion exchange, and intercalation can be beneficially separated, and a better selectivity of sensing is achievable.

Specifically, we expect that substituting the spin-coated clay layers with proposed either {nanoclay-(sol-gel oxide) $\}_n$  or {nanoclay-(oxide nanoparticle) $\}_n$  multilayers will significantly enhance the sensitivity and selectivity of these sensors, because we have an improved control of nanoporosity and we can now separate the effects of adsorption, ion exchange and intercalation. Thus, it becomes feasible to design a matrix of multilayer

sensors with different nanoporosity and nanoparticles, which will respond selectively to different chemical or biological species (Figure 48). Such responses can be detected by a combination of adsorption band/color changes. Consequently, this is a new platform for designing low-cost, user-friendly, versatile sensor matrix with high sensitivity and selectivity. Moreover, we can clarify and elucidate the mechanisms of photonic clay sensors.

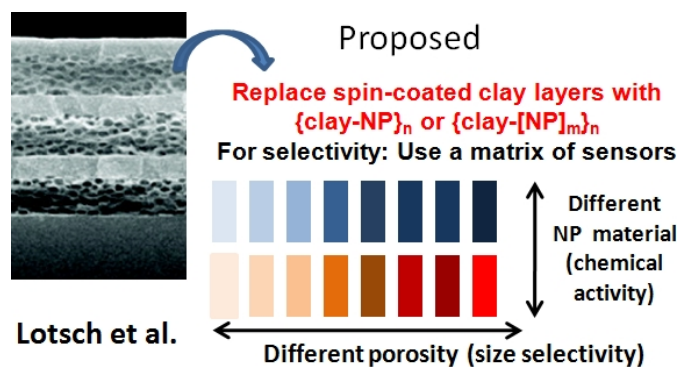


**Figure 48.** Photonic clays: a new class of chemical sensors made of spin-coated porous clay-TiO<sub>2</sub> multilayers and the proposed photonic sensor matrix.

## 5. Protective Coatings

The {MMT<sub>x</sub>-(sol-gel ZrO<sub>2</sub>)<sub>n</sub>} or other {nanoclay-(sol-gel oxide)}<sub>n</sub> multilayers can be used as protective coatings. The nacre-like, the brick-and-mortar structures of these multilayers is similar to that of polymer-MMT multilayers, which have proven to have superior mechanical properties<sup>9,97</sup>. The {MMT<sub>x</sub>-(sol-gel ZrO<sub>2</sub>)<sub>n</sub>} multilayers are composed of hard zirconia components and planar nanoclay layers; the presence of planar

clay nano-layers may increase the fracture toughness of these nanocomposite films by deflecting cracks.

These 2-D nanoclays may also serve as diffusion barriers; thus, applications as anti-corrosive and anti-oxidation coatings may also be envisioned. In fact, anticorrosive coatings made of nanoclay-polymer composites have already been synthesized. For example, Yeh *et al.* coated a MMT-PMMA composite film on a cold-rolled steel substrate, and electrochemical evaluations showed that these coatings have better performance than PMMA coatings<sup>188, 189</sup>. It was proposed that the incorporation of nanoclays enhances the anticorrosive performance by increasing the diffusion pathways

50 .

MMT-zirconia multilayers are potentially good anticorrosive coatings, particularly for applications at high temperatures where polymer-nanoclay coatings cannot be used. In fact, sol-gel zirconia coatings on magnesium alloys showed good anticorrosive performances<sup>190</sup>. The incorporation of 2-D MMT nanosheets will increase diffusion pathways; the concept is essentially similar to that is shown in Figure 46 (a) for applications in filtering membranes.

## CHAPTER NINE

### SUMMARY

A new class of all-inorganic nanostructure multilayers,  $\{\text{MMT}_x\text{-(sol-gel oxide)}\}_n$ , has been synthesized for the first time to our knowledge. These multilayers are synthesized by sequentially dipping a substrate in an exfoliated nanoclay suspension and a sol-gel precursor solution. This study demonstrated the feasibility of replacing polyelectrolytes by sol-gel oxide as “glues” to fabricate LbL assembled multilayers. It represents an innovative concept of fabricating nanoscale multilayers via layer-by-layer methods.

A series of systematic experiments of  $\{\text{nanoclay-(sol-gel ZrO}_2)\}_n$  multilayers led to the following main conclusions about the growth kinetics and assembly mechanisms:

- The growth of the MMT and sol-gel  $\text{ZrO}_2$  layers is strongly coupled, and these two oppositely charged building units can enhance each other significantly, primarily due to electrostatic attractions.
- The film growth rate can be controlled between  $\sim 10$  nm and  $\sim 60$  nm per cycle via varying the precursor concentration, holding time in the precursor solution, and precursor aging time.
- The growth kinetics of the sol-gel layers cannot be explained by simple mass diffusion or interfacial reaction controlled models, indicating that the electrostatic

interactions may significantly impact the growth of sol-gel ZrO<sub>2</sub> layers on the MMT surfaces,

- The growth of sol-gel ZrO<sub>2</sub> layers on MMT surfaces exhibit a self-limiting thickness of ~ 50-60 nm, which may be explained by the screening of the electrostatic interactions.
- When the zirconium acetate precursors are aged, the growth of sol-gel layers is controlled by a hydrodynamic process that obeys the well-known Landau-Levich model.

We have further demonstrated that:

- Isothermal annealing at ~400 °C will dehydrate the multilayers and remove the residue acetate groups without damaging the MMT nanoplatelets and the ordered layered structure of the films.
- Free-standing multilayers can be made via using sacrificial substrates.
- Nanomechanical measurements also showed that the elastic modulus (and presumably other properties) of these composite multilayers can be intentionally tuned by changing the multilayer design and that significant porosity is present in these multilayers even after annealing.
- This newly developed methodology can be extended to other metal oxides.

Moreover, we have synthesized yet another new class of {nanoclay-(oxide nanoparticle)}<sub>n</sub> multilayers (again for the first time), with a novel “plate-ball”



architecture. Several derivative and more complex multilayer structures have also been made. Finally, we also explore the feasibility to synthesize several other types of multilayer structure, including nanoclay-ionic liquid, polymer-oxide multilayers, and nanotube-oxide multilayers.

Potential applications of the {nanoclay-(sol-gel oxide)}<sub>n</sub> and {nanoclay-(oxide nanoparticle)}<sub>n</sub> multilayers as high-temperature gas membranes, micro-cantilevers, interface-based fast ion conductor, photonic sensors, and protective coatings are discussed.

The success of this series of studies enables further endeavors to make a variety of novel nanostructured films. These LbL deposition techniques can be conveniently adapted for making periodic multilayers or functionally-graded oxide films via changing the composition or concentration of oxide cationic precursor solutions periodically or continuously. As shown in Figure 49, integration of various active (e.g., piezoelectric or magnetic) oxide and non-oxide ceramic materials enables a versatile yet inexpensive approach to fabricate functional nanostructures in further studies, and other types of nanosheets (e.g., exfoliated layered double hydroxides, MoS<sub>2</sub>, or graphenes) can be used to replace nanoclays to provide further versatility for the design of these nanostructures. Finally, LbL assembly of hybrid ceramic-nanosheet-polymer multilayers can also be envisioned.

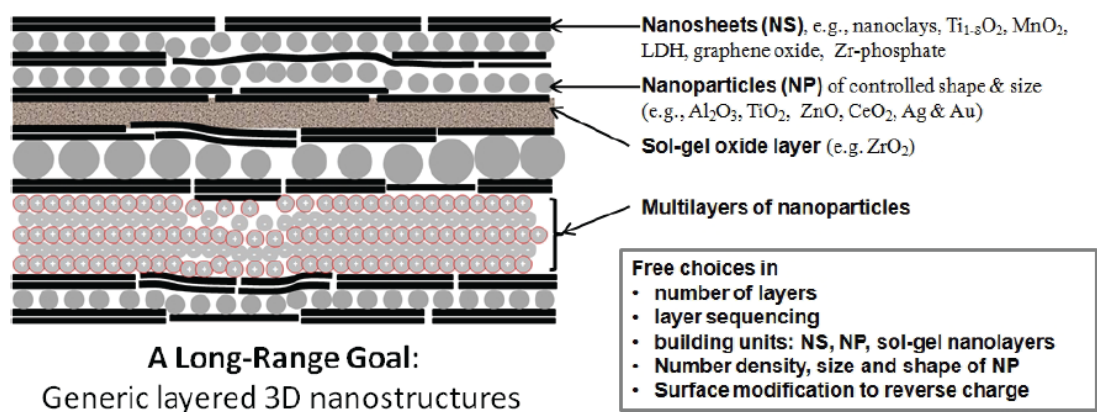


**Figure 49.** Generic layered 3D nanostructures of nanoclay-nanoparticle based multilayers.

## APPENDICES

## Appendix A

### SYNTHESIS OF CERIA FILMS

Ceria films were synthesized with a modified SILAR method. A 0.1 M cerium nitrate and 1 N  $\text{NH}_4\text{OH}$  were used as the cationic and anionic solutions respectively. The cerium nitrate solution was prepared by dissolving 0.326 g cerium (III) nitrate hexahydrate ( $\text{Ce}(\text{NO}_3)_3 \cdot 6\text{H}_2\text{O}$ ) in 75 ml deionized water. Ceria films were made using the following parameters: dipping speed = 20 mm per minute, holding time = 10 seconds, annealing temperature =  $600^\circ\text{C}$ , annealing time = 2 hours, and deposition cycles = 10. The quality of ceria films made by our modified method (one rinsing step) was comparable with those made by Arcot's method (no rinsing steps), as shown in Figure 50 (a) vs. (b). Both films are uniform and nanocrystalline. The grow rate of ceria film made by our method is 5 nm per cycle, which is similar to that made using Arcot's method (6 nm per cycle<sup>90</sup>).

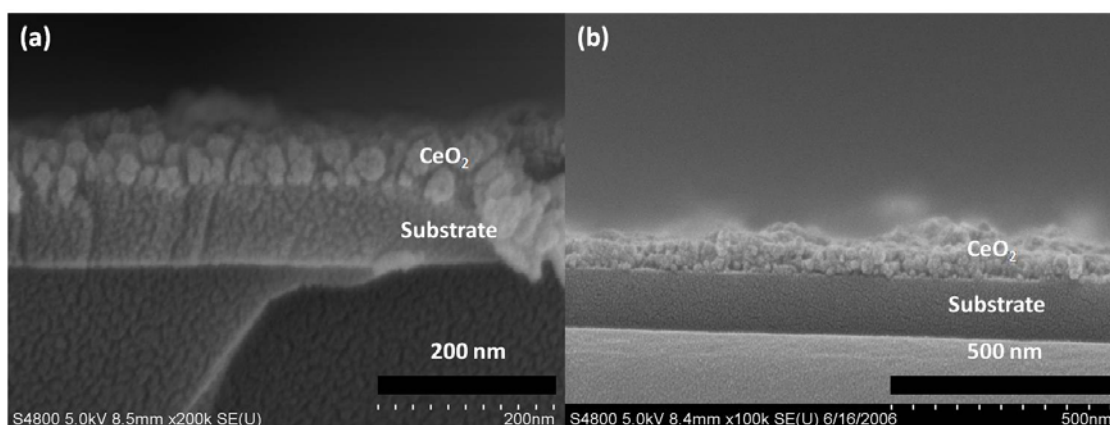


**Figure 50.** Cross sectional SEM images of ceria films made using (a)  $Ce(NO_3)_3 \cdot 6H_2O$  and  $NH_4OH$  precursors and (b) Arcot's method.

One issue about using the  $Ce(NO_3)_3$  cationic solution and the  $NH_4OH$  anionic solution is that one noticeable layer of impurity film appears on the surface of the  $Ce(NO_3)_3$  solution after/during the deposition procedure, or even without running the deposition procedure. Probably, the evaporated ammonia from  $NH_4OH$  solution reacts with  $Ce(NO_3)_3$  on its solution surface, forming complexes  $(NH_4)_x Ce(NO_3)_y$ .

Therefore, two new recipes were tried. In one recipe, a 0.1 M  $Ce(NO_3)_3$  and a 0.01 N  $NaOH$  precursor solution were used. In the other recipe, which was adapted from Tolstoy *et al.*'s<sup>191</sup>, ceria films were synthesized with a 10-minute holding in 0.01 M  $Ce(NO_3)_3$  as a substrate pretreatment and then with repeatedly dipping in 0.001 M cerium acetate, rinsing, dipping in a mixture of 0.1 M  $H_2O_2$  and  $NH_4OH$ , and rinsing. The ceria film made with  $Ce(NO_3)_3$  and  $NaOH$  solutions had a growth rate of 4.8 nm per cycle and good thickness uniformity (Figure 51a). The ceria film made with the adapted Tolstoy's recipe had a growth rate of  $\sim 1$  nm per cycle, similar as Tolstoy's report (0.75 nm per cycle<sup>191</sup>), and was also uniform (Figure 51 b). Importantly, no impurity films formed on any solution surfaces. Therefore, both recipes can be used for future ceria film synthesis.

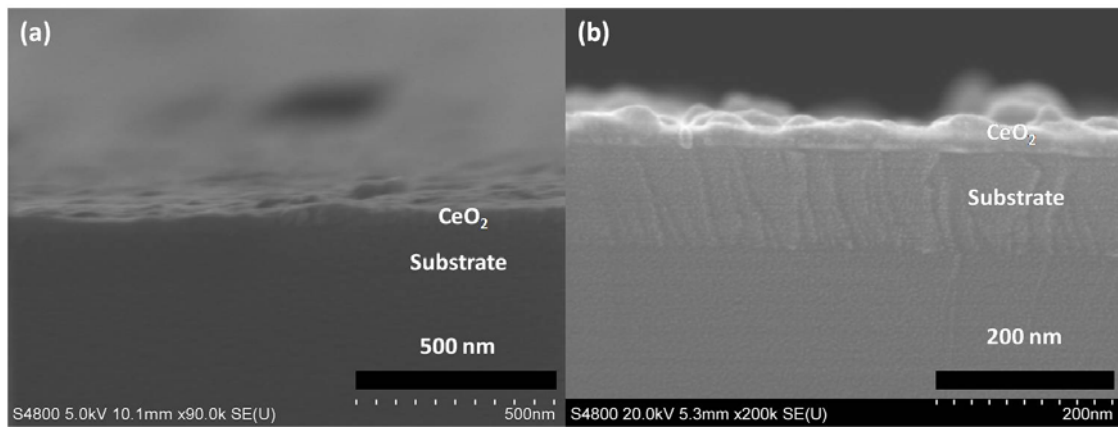


**Figure 51.** Cross-sectional SEM images of ceria films made with (a)  $Ce(NO_3)_3 \cdot 6H_2O$  and NaOH precursor solutions, and (b) the recipe adapted from Tolstoy *et al.*'s<sup>191</sup>

## Appendix B

### OPTIMIZATION EXPERIMENTS

#### **1. Substrate Cleaning**

Five cleaning methods were investigated, and a well-cleaned SiO<sub>2</sub> substrate is expected.

##### ***1.1 Cleaning procedures***

###### **Method a. (standard cleaning)**

1. A sulfuric acid and hydrogen peroxide mixture (piranha solution) was prepared with 3:1 volume ratio of 98% H<sub>2</sub>SO<sub>4</sub> and 30% H<sub>2</sub>O<sub>2</sub>. Silicon substrates were immersed into a 40 ml piranha solution and kept in a fume hood for 20 minutes.
2. Rinsing the substrates 4 times with deionized water.
3. An ammonium hydroxide and hydrogen peroxide mixture (SC 1<sup>192</sup>) was prepared with 5:1:1 volume ratio of deionized water, 30% H<sub>2</sub>O<sub>2</sub>, and 29% NH<sub>4</sub>OH. The substrates were immersed into a 70 ml SC 1 solution and were heated at 70 °C for 10 minutes with a hot plate.
4. Rinsing the substrates 4 times with deionized water.
5. A hydrochloride acid and hydrogen peroxide mixture (SC 2<sup>192</sup>) was prepared with 5:1:1 volume ratio of deionized water, 30% H<sub>2</sub>O<sub>2</sub>, and 37% HCl. The substrates were immersed into a 70 ml SC 2 solution and were heated at 70 °C for 10 minutes with a hot plate.

6. Rinsing the substrates 4 times with deionized water.
7. Drying the substrates with N<sub>2</sub> gas.

**Method b. (acetone cleaning)** <sup>90,98</sup>

1. Substrates were immersed into a 30 ml 99.5% acetone solution and ultrasonicated for 30 minutes.
2. The substrates were held in air until acetone residues evaporated.

**Method c. (alkali cleaning)** <sup>90,98</sup>

1. Substrates were immersed into a 75 ml 0.1 M NaOH solution for 20 minutes.
2. The substrates were immersed into a 75 ml 1N HCl solution for 5 minutes.
3. The substrates were ultrasonically rinsed in deionized water for 20 minutes.
4. The substrates were held in air for ~ 20 minutes until no visible water residues on the substrate surface.

**Method d.**

1. Substrates were immersed into a 30 ml 95% hexane (C<sub>6</sub>H<sub>14</sub>) solution for 10 minutes.
2. The substrates were immersed into a 30 ml 99.5% toluene (C<sub>7</sub>H<sub>8</sub>) solution for 10 minutes.
3. The substrates were immersed into a 30 ml 99.5% acetone (CH<sub>3</sub>COCH<sub>3</sub>) solution for 10 minutes.
4. The substrates were immersed into a 30 ml 99.5% ethanol (C<sub>2</sub>H<sub>5</sub>OH) solution for 10 minutes.
5. The substrates were immersed into 30 ml deionized water for 10 minutes.



6. The substrates were immersed into a 30 ml 99.5% acetone solution for 10 minutes.

**Method e.**

1. Substrates were immersed into 75 ml 0.1 M NaOH and ultrasonicated for 20 minutes.
2. Rinsing the substrates 4 times with deionized water.
3. The substrates were immersed into a 40 ml piranha solution and kept in a fume hood for 20 minutes.
4. Rinsing the substrates 4 times with deionized water.
5. The substrates were held in air for ~ 20 minutes until no visible water residues on the substrate surface.

**1.2 Comparisons**

Optical micrographs of silicon substrates cleaned by five different methods are shown in Figure 52, and the background color difference is caused by incident light polarizations. All the substrates showed uniform and scratch-free surfaces. Furthermore, Figure 52 (a), (d) and (e) showed no impurity particles, but Figure 52 (b) and (c) showed more than ~ 10 particles per 0.5 mm<sup>2</sup>. Therefore, method *a*, *d*, and *e* are more effectively to clean the surface than method *b* or *c*. Method *e* uses fewer chemicals and has an easier procedure to follow, while having similar cleaning results as method *a* and *d*. Specifically, the basic NaOH and the piranha solution can remove both inorganic and organic contaminants. In addition, the treatment of the piranha solution makes substrates

more hydrophilic and good for solution-based film depositions. Therefore method *e* is selected to be the routine cleaning procedure.

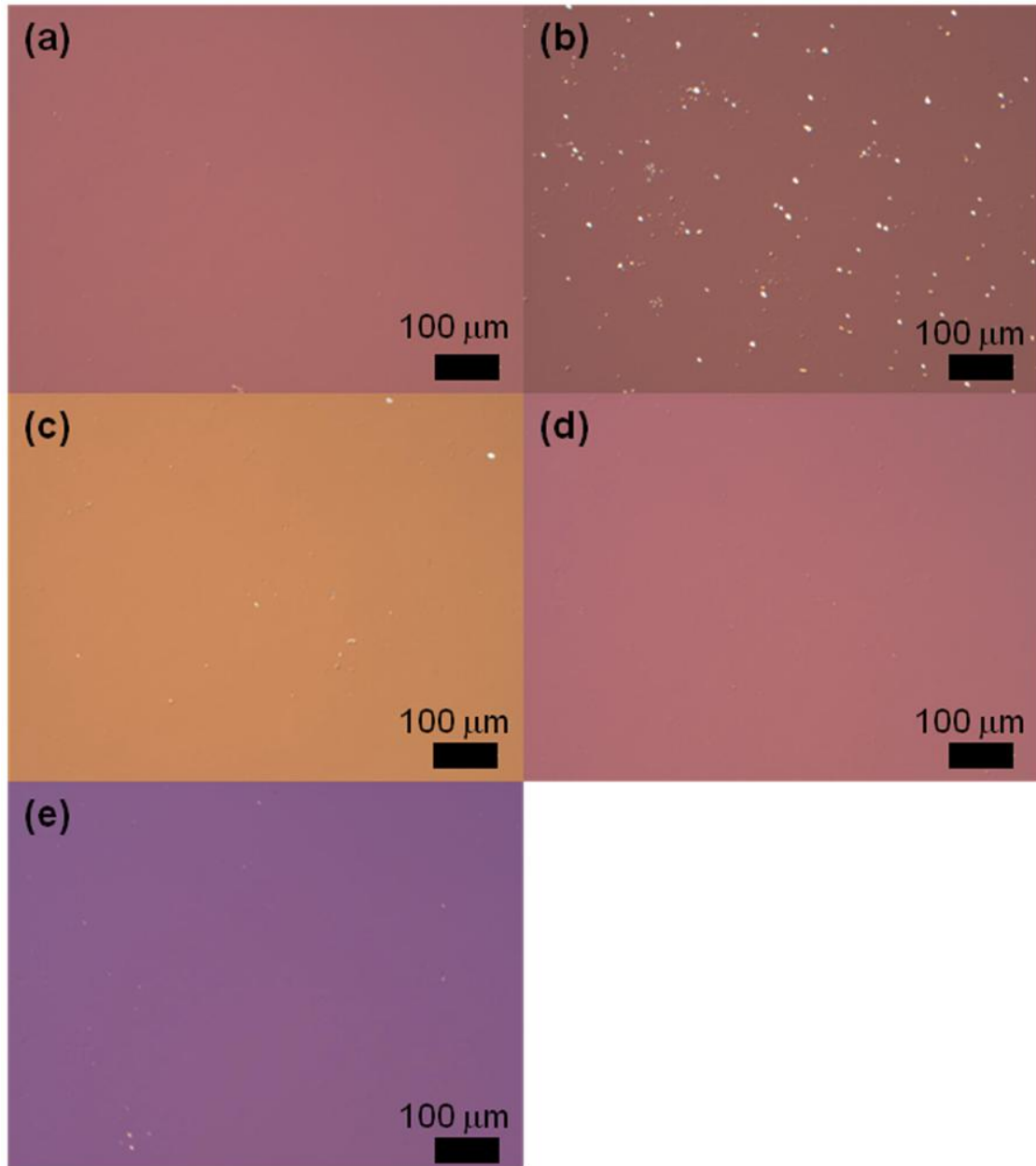


**Figure 52.** Optical micrographs of substrates cleaned by (a) method *a*, (b) method *b*, (c) method *c*, (d) method *d*, and (e) method *e*.

## 2. Montmorillonite Exfoliations

A variety of nanoclay exfoliation methods have been explored for synthesis of nanoclay-polymer multilayers, as listed in Table 7.

**Table 7.** Nanoclay exfoliation procedures from literatures.

Nanoclay	Exfoliation Procedures	Reference
Montmorillonite	<ol style="list-style-type: none"> <li>1. A few microgram clay powders were dispersed into 10 mL water.</li> <li>2. The suspension was ultrasonicated for 8-16 hours.</li> <li>3. The suspension settled one day or more.</li> </ol>	Piner <i>et al.</i> <sup>193</sup>
Montmorillonite	<ol style="list-style-type: none"> <li>1. 4 g MMT was dispersed into 120 mL deionized water.</li> <li>2. The suspension was stirred at room temperature for 24 hours and ultrasonicated for 30 minutes.</li> </ol>	Wang <i>et al.</i> <sup>194</sup>
Saponite	<ol style="list-style-type: none"> <li>1. Saponite was dispersed in deionized water with a concentration of 0.2 wt. %.</li> <li>2. The suspension was shaken 1 day, ultrasonicated 4-6 hours, and shaken additional 12-24 hours.</li> <li>3. The supernatant of the suspension was collected.</li> </ol>	Kim <i>et al.</i> <sup>195</sup>
Montmorillonite (Japan)	<ol style="list-style-type: none"> <li>1. MMT was dispersed in deionized water with a concentration of 0.3 mg/mL.</li> <li>2. The suspension was ultrasonicated for 3 minutes and</li> </ol>	Lvov <i>et al.</i> <sup>36</sup>

	controlled at pH 6.5.	
Montmorillonite (Hungary)	<ol style="list-style-type: none"> <li>1. A 10 g/L MMT suspension was prepared and settled in a 20-cm long jar for 17 hours.</li> <li>2. The supernatant of the suspension was removed and converted to Na-MMT by stirring with 1.0 N NaCl.</li> <li>3. The Na-MMT particles were then separated by centrifugation, washed, and dialyzed to remove excess electrolytes.</li> <li>4. 2.0 g of purified, air-dried Na-MMT was ultrasonicated in 100 mL distilled water (2 wt. %) for 40 minutes.</li> <li>5. The supernatant of the suspension was removed and ultrasonicated for another 20 minutes.</li> <li>6. The top fraction of the supernatant was separated and used after another two centrifugations at 3000 rpm.</li> </ol>	Kotov <i>et al.</i> <sup>37</sup>
Montmorillonite (USA)	<ol style="list-style-type: none"> <li>1. 5 g MMT was dispersed into 1 L deionized water.</li> <li>2. The suspension was vigorously stirred for 1 week.</li> <li>3. The suspension was allowed to sediment for 1 day and the supernatant was collected and used.</li> </ol>	Podsiadlo <i>et al.</i> <sup>10, 25</sup>

Three exfoliation methods were compared.

Method I (adapted from Lvov's method<sup>36</sup>)

1. 0.0225 g MMT (Cloisite Na<sup>+</sup>) was dispersed into 75 ml deionized water to form a 0.03 wt. % suspension (pH 7.24).
2. The suspension was stirred for 20 minutes at 1k rpm with a magnet.
3. The suspension was ultrasonicated for 20 minutes.

#### Method II

1. Preparing 0.2 g/ 40 ml sodium hexametaphosphate (Na-HMP; (NaPO<sub>3</sub>)<sub>6</sub>) solution.
2. 0.3 g MMT (Cloisite Na<sup>+</sup>) was dispersed into 75 ml deionized water to form a 0.4 wt. % suspension.
3. A 0.75 ml Na-HMP solution was added dropwise into the MMT suspension with a weight ratio of 1:100.
4. If the pH value of the MMT suspension is less than 7, then 0.1 N NaOH was added.
5. The MMT suspension was stirred for 20 minutes and then ultrasonicated for another 20 minutes.

Method III is same as Podsiadlo's, as listed in Table 7.

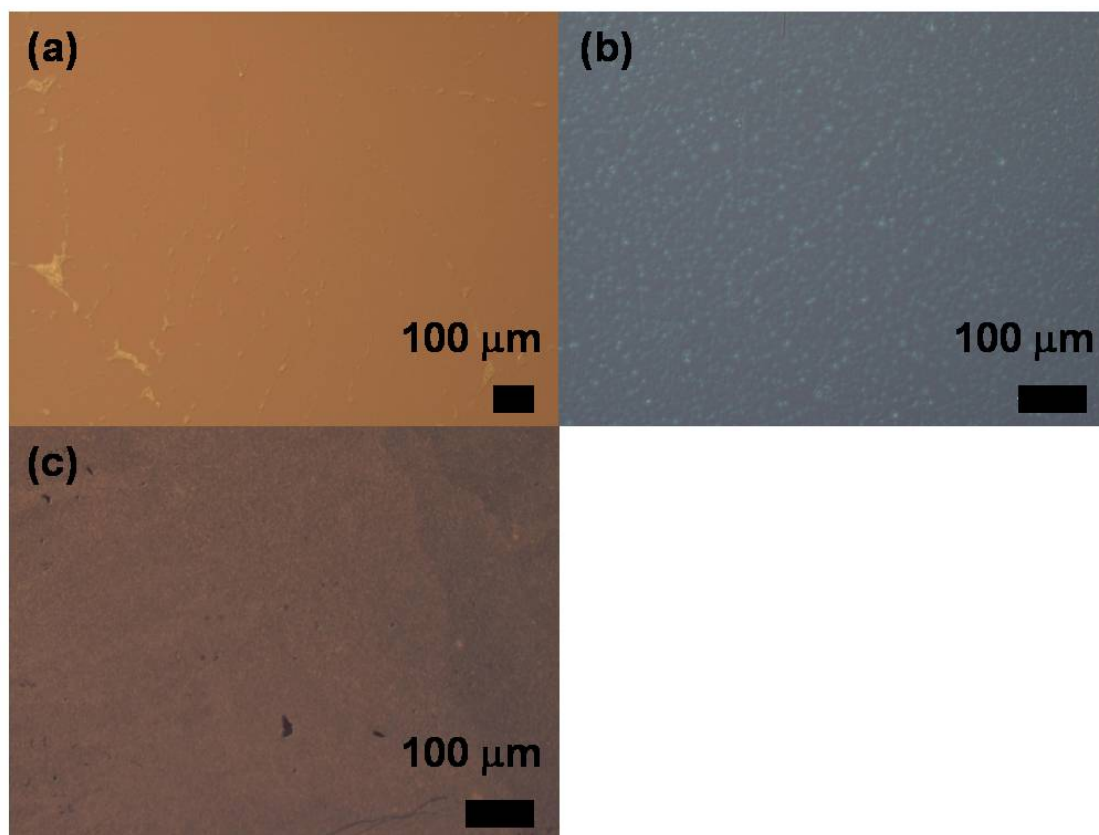


**Figure 53.** (a-c) Optical micrographs of pre-cleaned silicon substrates, which were dipped into the MMT suspension exfoliated by method I-III respectively.

Pre-cleaned substrates were dipped into the MMT suspension exfoliated with method I, II, or III, and their optical micrographs were shown in Figure 53. Both Figure 53 (b) and (c) show uniform substrate surfaces, and uniformly distributed clay platelets can be seen in Figure 53 (b). The substrate in Figure 53 (a) is largely uniform except some clay aggregations at the corner. Therefore, exfoliation method II and III result a better MMT coating on the substrate, suggesting a better quality of multilayers. Exfoliation method III takes a longer time to stir a MMT suspension than method I and

II, ensuring a fully exfoliation, and one-day settling removes residue large particles.

Therefore, we selected method III to further prepare nanoclay-zirconia multilayers.

## Appendix C

### EFFECTS OF PH ON THE GROWTH OF NANOCLAY-NANOPARTICLE MULTILAYERS

Two groups of experiments were designed to investigate effects of the pH of suspensions (nanoparticle or both nanoparticle and nanoclay) on the growth of {nanoclay-(CeO<sub>2</sub> nanoparticle)}<sub>n</sub> multilayers. In the first group of experiments, CeO<sub>2</sub> suspensions with the pH value from 1 to 7 were used, and nanoclay suspensions were used as-prepared (pH: 7.93). Cross-sectional SEM images of {MMT-CeO<sub>2</sub>}<sub>n</sub> multilayers are shown in Figure 54. If pH<sub>CeO<sub>2</sub></sub> = 6.97, {MMT-CeO<sub>2</sub>}<sub>n</sub> multilayers showed no layered structures. If pH<sub>CeO<sub>2</sub></sub> = 1.28 or 2.38, the multilayers showed regular layered structures, and the thickness was 52 and 36 nm per layer respectively.

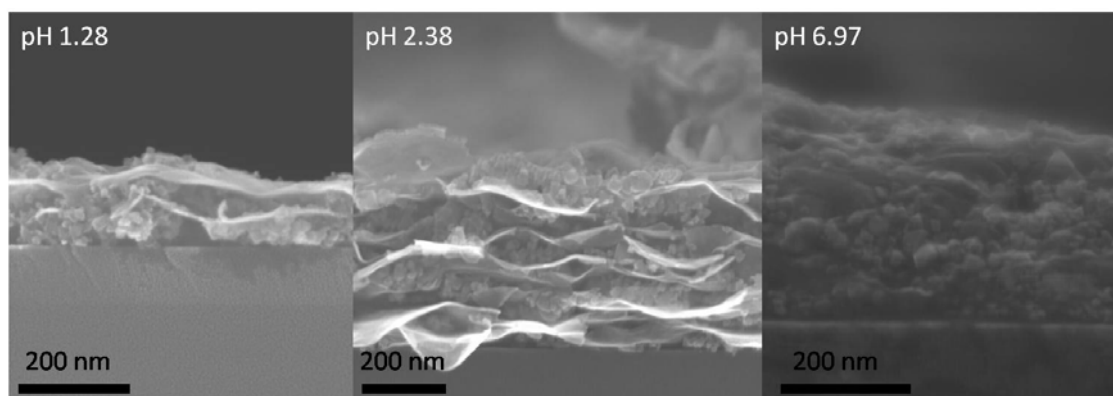


**Figure 54.** Cross-sectional SEM images of {MMT-CeO<sub>2</sub>}<sub>n</sub> multilayers synthesized with different pH values of CeO<sub>2</sub> suspensions.

Since the PZC of CeO<sub>2</sub> is 8.1<sup>126</sup>, CeO<sub>2</sub> nanoparticles were positively charged when pH of the suspensions (MMT or CeO<sub>2</sub>) is less than 8.1. The zeta potential of CeO<sub>2</sub>



( $\zeta_{\text{CeO}_2}$ ) nanoparticles is  $\sim 0$  mV for  $\text{pH} = 7.93$  (in MMT suspension), slightly positive for  $\text{pH}_{\text{CeO}_2} = 6.97$ , and largely positive for  $\text{pH}_{\text{CeO}_2} = 2.38$  or  $1.28$ . However, the zeta potential of MMT surfaces ( $\zeta_{\text{MMT}}$ ) keeps constant  $\sim -30$  mV regardless of the pH of suspensions. When a substrate was dipped into a MMT suspension ( $\text{pH} = 7.93$ ), electrostatic attractions between  $\text{CeO}_2$  nanoparticles and MMT were negligible. When a substrate was dipped into a  $\text{CeO}_2$  suspension with a low pH ( $\text{pH} = 2.38$  or  $1.28$ ), electrostatic interactions between  $\text{CeO}_2$  nanoparticles and MMT were strong, and electrostatic-assisted LbL assembly forms multilayers. When a substrate was dipped into a  $\text{CeO}_2$  suspension with a high pH ( $\text{pH} = 6.97$ ), the electrostatic interactions between  $\text{CeO}_2$  nanoparticles and MMT were weak, hence neither layered structures nor multilayers were formed.

In the second group of experiments, the pH of  $\text{CeO}_2$  and MMT were set to be same. Cross-sectional SEM images of  $\{\text{MMT-CeO}_2\}_n$  multilayers are shown in Figure 55. No layered structures were observed for conditions as  $\text{pH}_{\text{CeO}_2} = \text{pH}_{\text{MMT}} = 1.3$  or  $\text{pH}_{\text{CeO}_2} = \text{pH}_{\text{MMT}} = 4.3$ . Though electrostatic interactions between  $\text{CeO}_2$  nanoparticles and MMT in both  $\text{CeO}_2$  and MMT suspensions are strong, as  $\text{CeO}_2$  nanoparticles are now positively charged in the both suspensions, the electrostatic interactions are more complex because of the change of pH of MMT suspension.

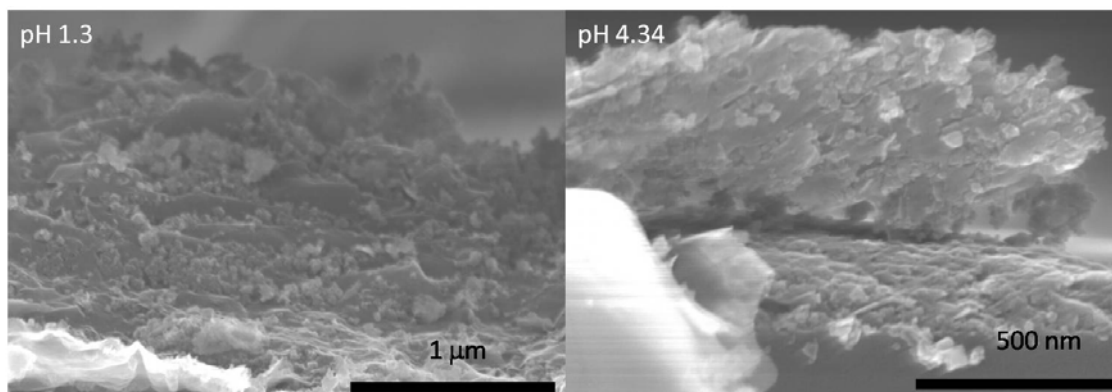


**Figure 55.** Cross-sectional SEM images of  $\{\text{MMT-CeO}_2\}_n$  multilayers made with  $\text{pH}_{\text{CeO}_2} = \text{pH}_{\text{MMT}} = 1.3$  (left image) or  $\text{pH}_{\text{CeO}_2} = \text{pH}_{\text{MMT}} = 4.3$  (right image).

MMT edges take only 1% of total surface area of a MMT platelet<sup>196</sup>, and have pH-dependent charges (not as MMT surfaces). Since the PZC of the MMT edge is 7<sup>196</sup>, the MMT edge is positively charged when  $\text{pH}_{\text{CeO}_2} = \text{pH}_{\text{MMT}} = 1.3$  or 4.3, with zeta potential  $\approx 20$  mV for both cases<sup>196</sup>. In a  $\text{CeO}_2$  suspension ( $\text{pH}_{\text{CeO}_2} = 1.3$  or 4.3), MMT surfaces were negatively charged (-30 mV) and positive  $\text{CeO}_2$  nanoparticles were attracted to them, though the electrostatic interactions between MMT edges and  $\text{CeO}_2$  may be negligible due to the low amount of exposed edges. In a MMT suspension ( $\text{pH}_{\text{MMT}} = 1.3$  or 4.3), positive  $\text{CeO}_2$  nanoparticles attracted negative MMT surfaces, as shown in Figure 56. While, simultaneously, positive MMT edges would move towards negative MMT surfaces, forming ‘edge-face’ aggregations. This may also explain the lack of layered structures in Figure 55.

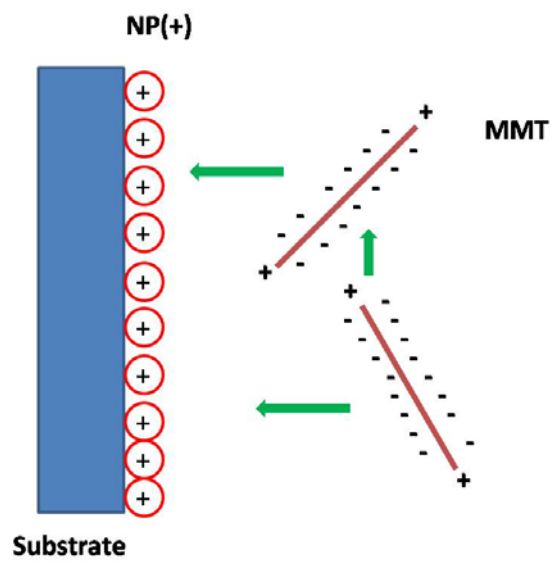


**Figure 56.** A schematic of the MMT adsorption on positive nanoparticles with MMT edges positively charged.

## REFERENCES

1. Peterson, I. R., Langmuir-Blodgett films. *J. Phys. D: Appl. Phys.* **1990**, *23*, 379-395.
2. Decher, G., Fuzzy nanoassemblies: toward layered polymeric multicomposites. *Science* **1997**, *277*, (5330), 1232-1237.
3. Decher, G.; Lvov, Y.; Schmitt, J., Proof of multilayer structural organization in self-assembled polycation-polyanion molecular films. *Thin Solid Films* **1994**, *244*, 772-777.
4. Lvov, Y.; Ariga, K.; Onda, M.; Ichinose, I.; Kunitake, T., A careful examination of the adsorption step in the alternate layer-by-layer assembly of linear polyanion and polycation. *Colloids Surf., A* **1999**, *146*, 337-346.
5. Lvov, Y.; Decher, G.; Mohwald, H., Assembly, structural characterization, and thermal-behavior of layer-by-layer deposited ultrathin films of poly(vinylsulfate) and poly(allylamine). *Langmuir* **1993**, *9*, (2), 481-486.
6. Schmitt, J.; Decher, G.; Dressick, W. J.; Brandow, S. L.; Geer, R. E.; Shashidhar, R.; Calvert, J. M., Metal nanoparticle/polymer superlattice films: Fabrication and control of layer structure. *Adv. Mater.* **1997**, *9*, (1), 61-65.
7. Lvov, Y.; Decher, G.; Sukhorukov, G., Assembly of thin films by means of successive deposition of alternate layers of DNA and poly(allylamine). *Macromolecules* **1993**, *26*, (20), 5396-5399.
8. Lvov, Y.; Haas, H.; Decher, G.; Mohwald, H., Successive deposition of alternate layers of polyelectrolytes and a charged virus. *Langmuir* **1994**, *10*, 4232-4236.
9. Tang, Z.; Kotov, N. A.; Magonov, S.; Ozturk, B., Nanostructured artificial nacre. *Nature Materials* **2003**, *2*, 413-418.
10. Podsiadlo, P.; Kaushik, A. K.; Arruda, E. M.; Waas, A. M.; Shim, B. S.; Xu, J.; Nandivada, H.; Pumphlin, B. G.; Lahann, J.; Ramamoorthy, A.; Kotov, N. A., Ultrastrong and stiff layered polymer nanocomposites. *Science* **2007**, *318*, 80-83.
11. Lee, D.; Rubner, M. F.; Cohen, R. E., All-nanoparticle thin-film coatings. *Nano Lett.* **2006**, *6*, (10), 2305-2312.

12. Lee, D.; Omolade, D.; Cohen, R. E.; Rubner, M. F., pH-dependent structure and properties of TiO<sub>2</sub>/SiO<sub>2</sub> nanoparticle multilayer thin films. *Chem. Mater.* **2007**, *19*, 1427-1433.
13. Koorevaar, P.; Menelik, G.; Dirksen, C., *Elements of the soil physics*. Elsevier: 1984; p 228.
14. Powrie, W., *Soil mechanics: concepts and applications*. Taylor & Francis: 2004; p 675.
15. Fendler, J. H., Self-assembled nanostructured materials. *Chem. Mater.* **1996**, *8*, (8), 1616-1624.
16. Lutkenhaus, J. L.; Hammond, P. T., Electrochemically enabled polyelectrolyte multilayer devices: from fuel cells to sensors. *Soft Matter* **2007**, *3*, (7), 804-816.
17. Hammond, P. T., Form and function in multilayer assembly: new applications at nanoscale. *Adv. Mater.* **2004**, *16*, (15), 1271-1293.
18. Bertrand, P.; Jonas, A.; Laschewsky, A.; Legras, R., Ultrathin polymer coatings by complexation of polyelectrolytes at interfaces: suitable materials, structure and properties. *Macromol. Rapid Commun.* **2000**, *21*, (y), 319-348.
19. Ras, R. H. A.; Umemura, Y.; Johnston, C. T.; Yamagishi, A.; Schoonheydt, R. A., Ultrathin hybrid films of clay minerals. *Phys. Chem. Chem. Phys.* **2007**, *9*, (8), 918-932.
20. Ariga, K.; Hill, J. P.; Ji, Q., Layer-by-layer assembly as a versatile bottom-up nanofabrication technique for exploratory research and realistic application. *Phys. Chem. Chem. Phys.* **2007**, *9*, (19), 2319-2340.
21. Jiang, S. P.; Liu, Z. C.; Tian, Z. Q., Layer-by-layer self-assembly of composite polyelectrolyte-nafion membranes for direct methanol fuel cells. *Adv. Mater.* **2006**, *18*, (8), 1068-1072.
22. Tang, Z.; Wang, Y.; Podsiadlo, P.; Kotov, N. A., Biomedical applications of layer-by-layer assembly: from biomimetics to tissue engineering. *Adv. Mater.* **2006**, *18*, 3203-3224.
23. Wang, Y.; Angelatos, A. S.; Caruso, F., Template synthesis of nanostructured materials via layer-by-layer assembly. *Chem. Mater.* **2008**, *20*, (3), 848-858.

24. Kim, D. W.; Blumstein, A.; Kumar, J.; Tripathy, S. K., Nanocomposite films derived from exfoliated functional aluminosilicate through electrostatic layer-by-layer assembly (vol 13, pg 1916, 2001). *Chem. Mater.* **2001**, 13, (8), 2742-2742.
25. Podsiadlo, P.; Liu, Z.; Paterson, D.; Messersmith, P. B.; Kotov, N. A., Fusion of seeshell nacre and marine bioadhesive analogs: high-strength nanocomposite by layer-by-layer assembly of clay and L-3,4-Dihydroxyphenylalanine polymer. *Adv. Mater.* **2007**, 19, (949-955), 949.
26. Quinn, J. F.; Johnston, A. P. R.; Such, G. K.; Zelikin, A. N.; Caruso, F., Next generation, sequentially assembled ultrathin films: beyond electrostatics. *Chem. Soc. Rev.* **2007**, 36, (5), 707-718.
27. Kleinfeld, E. R.; Ferguson, G. S., Stepwise formation of multilayered nanostructural films from macromolecular precursor. *Science* **1994**, 265, 370-373.
28. Mitzi, D. B., Thin-film deposition of organic-inorganic hybrid materials. *Chem. Mater.* **2001**, 13, (10), 3283-3298.
29. Bruening, M. L.; Dotzauer, D. M.; Jain, P.; Ouyang, L.; Baker, G. L., Creation of Functional Membranes Using Polyelectrolyte Multilayers and Polymer Brushes. *Langmuir* **2008**, 24, 7663-7673.
30. Jaber, J. A.; Schlenoff, J. B., Recent developments in the properties and applications of polyelectrolyte multilayers. *Curr. Opin. Colloid In.* **2006**, 11, 324-329.
31. Ferguson, G. S.; Kleinfeld, E. R., Mosaic tiling in molecular dimensions. *Adv. Mater.* **1995**, 7, (4), 414-416.
32. Olphen, H. v., *An introduction to clay colloid chemistry*. John Wiley & Sons: 1963; p 64.
33. Auerbach, S. M.; Carrado, K. A.; Dutta, P. K., *Handbook of layered materials*. CRC Press: 2004.
34. Kotov, N. A.; Magonov, S.; Tropsha, E., Layer-by-layer self-assembly of aluminosilicate-polyelectrolyte composites: Mechanism of deposition, crack resistance, and perspectives for novel membrane materials. *Chem. Mater.* **1998**, 10, (3), 886-895.
35. Podsiadlo, P.; Paternel, S.; Rouillard, J. M.; Zhang, Z. F.; Lee, J.; Lee, J. W.; Gulari, L.; Kotov, N. A., Layer-by-layer assembly of nacre-like nanostructured composites with antimicrobial properties. *Langmuir* **2005**, 21, (25), 11915-11921.

36. Lvov, Y.; Ariga, K.; Ichinose, I.; Kunitake, T., Formation of ultrathin multilayer and hydrated Gel from montmorillonite and linear polycations. *Langmuir* **1996**, 12, 3038-3044.
37. Kotov, N. A.; Haraszti, T.; Turi, L.; Zavala, G.; Geer, R. E.; Dekany, I.; Fendler, J. H., Mechanism of and defect formation in the self-assembly of polymeric polycation-montmorillonite ultrathin films. *J. Am. Chem. Soc.* **1997**, 119, 6821-6832.
38. Aksay, I. A.; Trau, M.; Manne, S.; Honma, I.; Yao, N.; Zhou, L.; Fenter, P.; Eisenberger, P. M.; Gruner, S. M., Biomimetic pathways for assembling inorganic thin films. *Science* **1996**, 273, 892-898.
39. Smith, B. L.; Schaffer, T. E.; Viani, M.; Thompson, J. B.; Frederick, N. A.; Kindt, J.; Belcher, A.; Stucky, G. D.; Morse, D. E.; Hansma, P. K., Molecularmechanistic origin of the toughness of natural adhesives, fibers and composites. *Nature* **1999**, 399, 761-763.
40. Munch, E.; Launey, M. E.; Alsem, D. H.; Saiz, E.; Tomsia, A. P.; Ritchie, R. O., Tough, bio-inspired hybrid materials. *Science* **2008**, 322, (5907), 1516-1520.
41. Bellamkonda, R. V., Biomimetic materials - Marine inspiration. *Nature Materials* **2008**, 7, (5), 347-348.
42. Tamura, K.; Yokoyama, S.; Pascua, C. S.; Yamada, H., New age of polymer nanocomposites containing dispersed high-aspect-ratio silicate nanolayers. *Chem. Mater.* **2008**, 20, (6), 2242-2246.
43. Ortiz, C.; Boyce, M. C., Materials science - bioinspired structural materials. *Science* **2008**, 319, (5866), 1053-1054.
44. Bonderer, L. J.; Studart, A. R.; Gauckler, L. J., Bioinspired design and assembly of platelet reinforced polymer films. *Science* **2008**, 319, (5866), 1069-1073.
45. Wagner, H. D., Nanocomposites - Paving the way to stronger materials. *Nature Nanotechnology* **2007**, 2, (12), 742-744.
46. Edwards, J., Transparent film with strength of steel. *Chemistry World* **2007**, 4, (11), 31-31.
47. Mamedov, A.; Ostrander, J.; Aliev, F.; Kotov, N. A., Stratified assemblies of magnetite nanoparticles and montmorillonite prepared by the layer-by-layer assembly. *Langmuir* **2000**, 16, 3941-3949.

48. Gao, G.; Hong, H.-G.; Mallouk, T. E., Layered metal phosphates and phosphonates: from crystals to monolayers. *Acc. Chem. Res.* **1992**, *25*, 420-427.
49. Johnson, J. W.; Brody, J. F.; Alexander, R. M.; Yacullo, L. N.; Klein, C. F., Zirconia-pillared tetrasilicic fluoromica. *Chem. Mater.* **1993**, *5*, 36-42.
50. Yeh, J.-M.; Chang, K.-C., Polymer/layered silicate nanocomposite anticorrosive coatings. *J. Ind. Eng. Chem.* **2008**, *14*, 275-291.
51. Jiang, C.; Tsukruk, V. V., Freestanding nanostructures via layer-by-layer assembly. *Adv. Mater.* **2006**, *18*, 829-840.
52. Iler, R. K., Multilayers of colloidal particles. *J. Colloid Interface Sci.* **1966**, *21*, 569-594.
53. Lee, D.; Gemici, Z.; Rubner, M. F.; Cohen, R. E., Multilayers of oppositely charged SiO<sub>2</sub> nanoparticles: effect of surface charge on multilayer assembly. *Langmuir* **2007**, *23*, (17), 8833-8837.
54. Zhang, X.; Wang, Y.; Chen, X.; Yang, W., Fabrication and characterization of a novel inorganic MnO<sub>2</sub>/LDHs multilayer thin film via a layer-by-layer self-assembly method. *Mater. Lett.* **2008**, *62*, 1613-1616.
55. Lee, S. W.; Kim, B.-S.; Chen, S.; Shao-Horn, Y.; Hammond, P. T., Layer-by-layer assembly of all carbon nanotube ultrathin films for electrochemical applications. *J. Am. Chem. Soc.* **2009**, *131*, 671-679.
56. Kim, J.; Lee, S. W.; Hammond, P. T.; Shao-Horn, Y., Electrostatic layer-by-layer assembled Au nano particle/MWNT thin films: microstructure, optical Property, and electrocatalytic activity for methanol oxidation. *Chem. Mater.* **2009**, *21*, (13), 2993-3001.
57. Kumar, A.; Mandale, A. B.; Sastry, M., Sequential electrostatic assembly of amine-derivatized gold and carboxylic acid-derivatized silver colloidal particles on glass substrates. *Langmuir* **2000**, *16*, 6921-6926.
58. Musick, M. D.; Keating, C. D.; Lyon, L. A.; Botsko, S. L.; Pena, D. J.; Holliday, W. D.; McEvoy, T. M.; Richardson, J. N.; Natan, M. J., Metal films prepared by stepwise assembly. 2. construction and characterization of colloidal Au and Ag multilayers. *Chem. Mater.* **2000**, *12*, 2869-2881.
59. Wang, Z.-S.; Sasaki, T.; Muramatsu, M.; Ebina, Y.; Tanaka, T.; Wang, L.; Watanabe, M., Self-assembled multilayers of titania nanoparticles and nanosheets with polyelectrolytes. *Chem. Mater.* **2003**, *15*, 807-812.



60. Zhou, Y.; Ma, R.; Ebina, Y.; Takada, K.; Sasaki, T., Multilayer hybrid films of titania semiconductor nanosheet and silver metal fabricated via layer-by-layer self-assembly and subsequent UV irradiation. *Chem. Mater.* **2006**, 18, 1235-1239.
61. Hua, F.; Cui, T.; Lvov, Y. M., Ultrathin cantilevers based on polymer-ceramic nanocomposite assembled through layer-by-layer adsorption. *Nano Lett.* **2004**, 4, (5), 823-825.
62. Sukhishvili, S. A.; Kharlampieva, E.; Izumrudov, V., Where polyelectrolyte multilayers and polyelectrolyte complexes meet. *Macromolecules* **2006**, 39, (26), 8873-8881.
63. Yoo, D.; Shiratori, S. S.; Rubner, M. F., Controlling bilayer composition and surface wettability of sequentially adsorbed multilayers of weak polyelectrolytes. *Macromolecules* **1998**, 31, (13), 4309-4318.
64. Shiratori, S. S.; Rubner, M. F., pH-dependent thickness behavior of sequentially adsorbed layers of weak polyelectrolytes. *Macromolecules* **2000**, 33, 4213-4219.
65. Hoogeveen, N. G.; Stuart, M. A. C.; Fleer, G. J., Formation and stability of multilayers of polyelectrolytes. *Langmuir* **1996**, 12, 3675-3681.
66. Khopade, A. J.; Caruso, F., Investigation of the factors influencing the formation of dendrimer/polyanion multilayer films. *Langmuir* **2002**, 18, 7669-7676.
67. Chen, W.; McCarthy, T. J., Layer-by-layer deposition: a tool for polymer surface modification. *Macromolecules* **1997**, 30, 78-86.
68. Bucur, C. B.; Sui, Z.; Schlenoff, J. B., Ideal Mixing in Polyelectrolyte Complexes and Multilayers: Entropy Driven Assembly. *J. Am. Chem. Soc.* **2006**, 128, 13690-13691.
69. Bharadwaj, S.; Montazeri, R.; Haynie, D. T., Direct determination of the thermodynamics of polyelectrolyte complexation and implications thereof for electrostatic layer-by-layer assembly of multilayer films. *Langmuir* **2006**, 22, 6093-6101.
70. Srivastava, S.; Kotov, N. A., Composite layer-by-layer (LBL) assembly with inorganic nanoparticles and nanowires. *Acc. Chem. Res.* **2008**, 41, (12), 1831-1841.

71. Stockton, W. B.; Rubner, M. F., Molecular-level processing of conjugated polymers. 4. layer-by-layer manipulation of polyaniline via hydrogen-bonding interactions. *Macromolecules* **1997**, 30, 2717-2725.
72. Grim, R. E., *Clay Mineralogy*. McGraw-Hill: New York, 1968.
73. Grim, R. E.; Kulbicki, G., Montmorillonite: high temperature reactions and classification. *Am. Mineral* **1961**, 46, 1329-1369.
74. Way, J. T., On the power of Sols to absorb manure. *J. roy. Agr. Soc. Engl.* **1852**, 13, 123-143.
75. Norrish, K., The swelling of montmorillonite. *Discuss. Faraday Soc.* **1954**, 18, 120-134.
76. Theng, B. K. G., *Formation and properties of clay-polymer complexes*. Elsevier: Amsterdam, The Netherlands, 1979; p 362.
77. Jolivet, J.-P.; Henry, M.; Livage, J.; Bescher, E., *Metal oxide chemistry and synthesis: from solution to solid state*. John Wiley & Sons, Ltd: 2000; p 338.
78. Parks, G. A., The isoelectric points of solid oxides, solid hydroxides, and aqueous hydroxo complex systems. *Chem. Rev.* **1965**, 65, (2), 177-198.
79. Bedzyk, M. J.; Bommarito, G. M.; Caferey, M.; Penner, T. L., Diffuse-Double Layer at a Membrane-Aqueous Interface Measured with X-ray Standing Waves. *Science* **1990**, 248, 52-56.
80. Butt, H.-J.; Graf, K.; Kappl, M., *Physics and Chemistry of Interfaces*. Wiley-VCH: 2003; p 373.
81. Davis, J. A.; James, R. O.; Leckie, J. O., Surface ionization and complexation at the oxide/water interface I. computation of electrical double layer properties in simple electrolytes. *J. Colloid Interface Sci.* **1977**, 63, (3), 480-499.
82. Brinker, C. J.; Scherer, G. W., *SOL-GEL SCIENCE The Physics and Chemistry of Sol-Gel Processing*. Academic Press, Inc.: 1990; p 912.
83. Pierre, A. C., *Introduction to Sol-Gel processing*. Kluwer Academic Publishers: 1998; Vol. 1, p 394.
84. Livage, J.; Henry, M.; Sanchez, C., Sol-gel chemistry of transition metal oxides. *Prog. Solid St. Chem.* **1988**, 18, 259-341.

85. Brinker, C. J.; Hurd, A. J.; Schunk, P. R.; Frye, G. C.; Ashley, C. S., Review of sol-gel thin film formation. *J. Non-Cryst. Solids* **1992**, 147&148, 424-436.
86. Brinker, C. J.; Hurd, A. J., Fundamentals of sol-gel dip-coating. *J. Phys. III France* **1994**, 4, 1231-1242.
87. Niesen, T. P.; Guire, M. R. D., Review: deposition of ceramic thin films at low temperatures from aqueous solutions. *J. Electroceram.* **2001**, 6, 169-207.
88. Niesen, T. P.; Guire, M. E. D., Review: deposition of ceramic films at low temperatures from aqueous solutions. *Solid State Ionics* **2002**, 151, 61-68.
89. Nicolau, Y. F., Solution deposition of thin solid compound films by a successive ionic-layer adsorption and reaction process. *Appl. Surf. Sci.* **1985**, 22/23, 1061-1074.
90. Arcot, P. K. Solution based synthesis of zirconia and ceria thin films. Clemson University, Clemson, 2006.
91. Aoki, Y.; Kunitake, T., Solution-based fabrication of high-k gate dielectrics for next-generation metal-oxide semiconductor transistors. *Adv. Mater.* **2004**, 16, 118-123.
92. Aoki, Y.; Kunitake, T.; Nakao, A., Sol-gel fabrication of dielectric HfO<sub>2</sub> nano-films: Formation of uniform, void-free layers and their superior electrical properties. *Chem. Mater.* **2005**, 17, 450-458.
93. Park, S.; Clark, B. L.; Keszler, D. A.; Bender, J. P.; Wager, J. F.; Reynolds, T. A.; Herman, G. S., Low-temperature thin-film deposition and crystallization. *Science* **2002**, 297, (5578), 65-65.
94. Pizzi, A.; Mittal, K. L., *Handbook of adhesive technology*. CRC Press: 2003.
95. Ariga, K.; Lvov, Y.; Ichinose, I.; Kunitake, T., Ultrathin films of inorganic materials (SiO<sub>2</sub> nanoparticle, montmorillonite microplate, and molybdenum oxide) prepared by alternate layer-by-layer assembly with organic polyions. *Appl. Clay Sci.* **1999**, 15, 137-152.
96. Isayama, M.; Kunitake, T., Self-supporting films of clay minerals and metal oxides: molecular ceramics. *Adv. Mater.* **1994**, 6, (1), 77-78.
97. Rubner, M., Synthetic sea shell. *Nature* **2003**, 423, 925-926.

98. Arcot, P. K.; Luo, J., Solution-based synthesis of oxide thin films via a layer-by-layer deposition method: feasibility and a phenomenological film growth model. *Surf. Coat. Technol.* **2008**, 202, (12), 2690-2697.
99. Arcot, P. K.; Luo, J., Layer-by-layer deposition of zirconia thin films from aqueous solutions. *Mater. Lett.* **2008**, 62, 117-120.
100. Brindley, G. W., Invited review: Ethylene glycol and glycerol complexes of smectites and vermiculite. *Clay Miner.* **1966**, 6, 237-259.
101. Jeon, J.; Panchagnula, V.; Pan, J.; Dobrynin, A. V., Molecular dynamics simulations of multilayer films of polyelectrolytes and nanoparticles. *Langmuir* **2006**, 22, (10), 4629-4637.
102. Ostrander, J. W.; Mamedov, A. A.; Kotov, N. A., Two modes of linear layer-by-layer growth of nanoparticle-polyelectrolyte multilayers and different interactions in the layer-by-layer deposition. *J. Am. Chem. Soc.* **2001**, 123, (6), 1101-1110.
103. Kotov, N. A., Layer-by-layer self-assembly: The contribution of hydrophobic interactions. In *The Fourth International Conference on Nanostructured Materials (NANO '98)*, 1999; Vol. 12, pp 789-796.
104. Chen, H.; Zhang, G.; Richardson, K.; Luo, J., Synthesis of nanostructured nanoclay-zirconia multilayers: a feasibility study. *J. Nanomater.* **2008**, 2008, 749508.
105. Mamedov, A. A.; Kotov, N. A., Free-standing layer-by-layer assembled films of magnetite nanoparticles. *Langmuir* **2000**, 16, 5530-5533.
106. Oliver, W. C.; Pharr, G. M., Measurement of hardness and elastic modulus by instrumented indentation: Advances in understanding and refinements to methodology. *J. Mater. Res.* **2004**, 19, (1), 3-20.
107. Oliver, W. C.; Pharr, G. M., An improved technique for determining hardness and elastic modulus using load and displacement sensing indentation experiments. *J. Mater. Res.* **1992**, 7, (6), 1564-1583.
108. Tuck, J. R.; Korsunsky, A. M.; Bhat, D. G.; Bull, S. J., Indentation hardness evaluation of cathodic arc deposited thin hard coatings. *Surf. Coat. Technol.* **2001**, 139, (1), 63-74.
109. Wei, Z.; Zhang, G.; Chen, H.; Luo, J.; Liu, R.; Guo, S., A simple method for evaluating elastic modulus of thin films by nanoindentation. *J. Mater. Res.* **2009**, 24, (3), 777-791.

110. Balluffi, R. W.; Allen, S. M.; Carter, W. C.; Kemper, R. A., *Kinetics of Materials*. John Wiley and Sons: 2005; p 645.
111. Gandia, L. M.; Toranzo, R.; Vicente, M. A.; Gil, A., Non-aggressive pillaring of claying with zirconium acetate. Comparison with alumina pillared clays. *Appl. Catal., A* **1999**, 183, 23-33.
112. Davis, C. E.; Salisbury, H. M.; Harvey, M. T., Surface Tension of Gelation Solutions. *Ind. Eng. Chem.* **1924**, 16, (2), 161-163.
113. Tettenhorst, R., Cation migration in montmorillonites. *Am. Mineral* **1962**, 47, 769-773.
114. Geiculescu, A. C.; Spencer, H. G., Thermal decomposition and crystallization of aqueous Sol-Gel derived zirconium acetate gels: effects of the additive anions. *J. Sol-Gel Sci. Technol.* **2000**, 17, 25-35.
115. Noonan, G. O.; Ledford, J. S., Structure and chemical sensing applications of zirconium acetate Sol-Gel films. *Chem. Mater.* **1995**, 7, 1117-1123.
116. Saha, S. K.; Pramanik, P., Aqueous sol-gel synthesis of powders in the ZrO<sub>2</sub>-SiO<sub>2</sub> system using zirconium formate and tetraethoxysilane. *J. Non-Cryst. Solids* **1993**, 159, 31-37.
117. Monte, F. d.; Larsen, W.; Mackenzie, J. D., Stabilization of tetragonal ZrO<sub>2</sub> in ZrO<sub>2</sub>-SiO<sub>2</sub> binary oxides. *J. Am. Ceram. Soc.* **2000**, 83, (3), 628-634.
118. Ault, N. N.; Ueltz, H. F. G., *J. Am. Ceram. Soc.* **1953**, 36, 199-203.
119. Smith, C. F.; Crandall, W. B., *J. Am. Ceram. Soc.* **1964**, 47, 624-27.
120. Eichler, J.; Eisele, U.; Rodel, J., Mechanical properties of monoclinic zirconia. *J. Am. Ceram. Soc.* **2004**, 87, (7), 1401-1403.
121. Chen, B. Q.; Evans, J. R. G., Elastic moduli of clay platelets. *Scripta Materialia* **2006**, 54, (9), 1581-1585.
122. Kotov, N. A.; Dekany, I.; Fendler, J. H., Layer-by-layer self-assembly of polyelectrolyte-semiconductor nanoparticle composite films. *J. Phys. Chem.* **1995**, 99, 13065-13069.
123. He, J.-A.; Valluzzi, R.; Yang, K.; Dolukhanyan, T.; Sung, C.; Kumar, J.; Tripathy, S. K., Electrostatic multilayer deposition of a gold-dendrimer nanocomposite. *Chem. Mater.* **1999**, 11, 3268-3274.

124. Kim, H. S.; Sohn, B. H.; Lee, W.; Lee, J. K.; Choi, S. J.; Kwon, S. J., Multifunctional layer-by-layer self-assembly of conducting polymers and magnetic nanoparticles. *Thin Solid Films* **2002**, 419, 173-177.
125. Kosmulski, M., The significance of the difference in the point of zero charge between rutile and anatase. *Adv. Colloid Interface Sci.* **2002**, 99, 255-264.
126. Faria, L. A. D.; Trasatti, S., The point of zero charge of CeO<sub>2</sub>. *J. Colloid Interface Sci.* **1994**, 167, 352-357.
127. Benrabah, B.; Bouaza, A.; Hamzaoui, S.; Dehbi, A., Sol-gel preparation and characterization of antimony doped tin oxide (ATO) powders and thin films. *Eur. Phys. J. Appl. Phys.* **2009**, 48, 30301.
128. Terrier, C.; Chatelon, J. P.; Roger, J. A., Electrical and optical properties of Sb:SnO<sub>2</sub> thin films obtained by the sol-gel method. *Thin Solid Films* **1997**, 295, 95-100.
129. Li, N.; Martin, C. R., A high-rate, high-capacity, nanostructured Sn-based anode prepared using Sol-Gel template synthesis. *J. Electrochem. Soc.* **2001**, 148, (2), A164-A170.
130. Maddalena, A.; Maschio, R. D.; Dire, S.; Raccanelli, A., Electrical conductivity of tin oxide films prepared by the sol-gel method. *J. Non-Cryst. Solids* **1990**, 121, 365-369.
131. Terrier, C.; Chatelon, J. P.; Berjoan, R.; Roger, J. A., Sb-doped SnO, transparent conducting oxide from the sol-gel dip-coating technique. *Thin Solid Films* **1995**, 263, 37-41.
132. Ota, R.; Seki, S.; Sawada, Y.; Ogawa, M.; Nishide, T.; Shida, A.; Ide, M., Indium-tin-oxide films prepared by dip coating using an ethanol solution of indium chloride and tin chloride. *Surf. Coat. Technol.* **2003**, 169-170, 521-524.
133. Bhat, J. S.; Maddani, K. I.; Karguppikar, A. M., Influence of Zn doping on electrical and optical properties of multilayered tin oxide thin films. *Bull. Mater. Sci.* **2006**, 29, (3), 331-337.
134. Zhang, D.; Deng, Z.; Zhang, J.; Chen, L., Microstructure and electrical properties of antimony-doped tin oxide thin film deposited by sol-gel process. *Mater. Chem. Phys.* **2006**, 98, 353-357.

135. Banerjee, A. N.; Kundoo, S.; Saha, P.; Chattopandhyay, K. K., Synthesis and Characterization of Nano-Crystalline Fluorine-Doped Tin Oxide Thin Films by Sol-Gel Method. *J. Sol-Gel Sci. Technol.* **2003**, 28, 105-110.
136. Orel, B.; Lavrencic-Stangar, U.; Crnjak-Orel, Z.; Bukovec, P.; Kosec, M., Structural and FTIR spectroscopic studies of gel-xerogel-oxide transitions of SnO<sub>2</sub> and SnO<sub>2</sub>:Sb powders and dip-coated films prepared via inorganic sol-gel route. *J. Non-Cryst. Solids* **1994**, 167, 272-288.
137. Tang, W.; Cameron, D. C., Aluminum-doped zinc oxide transparent conductors deposited by the sol-gel process. *Thin Solid Films* **1994**, 238, 83-87.
138. O'Brien, S.; Koh, L. H. K.; Crean, G. M., ZnO thin films prepared by a single step sol-gel process. *Thin Solid Films* **2008**, 516, 1391-1395.
139. Dutta, M.; Mridha, S.; Basak, D., Effect of sol concentration on the properties of ZnO thin films prepared by sol-gel technique. *Appl. Surf. Sci.* **2008**, 254, 2743-2747.
140. Zhu, M. W.; Xia, J. H.; Hong, R. J.; Abu-Samra, H.; Huang, H.; Staedler, T.; Gong, J.; Sun, C.; Jiang, X., Heat-activated structural evolution of sol-gel-derived ZnO thin films. *J. Cryst. Growth* **2008**, 310, 816-823.
141. Lee, J.-H.; Ko, K.-H.; Park, B.-O., Electrical and optical properties of ZnO transparent conducting films by the sol-gel method. *J. Cryst. Growth* **2003**, 247, 119-125.
142. Srinivasan, G.; Kumar, J., Effect of Mn doping on the microstructures and optical properties of sol-gel derived ZnO thin films. *J. Cryst. Growth* **2008**, 310, 1841-1846.
143. Ohyama, M.; Kozuka, H.; Yoko, T., Sol-gel preparation of ZnO films with extremely preferred orientation along (002) plane from zinc acetate solution. *Thin Solid Films* **1997**, 306, 78-85.
144. Znaidi, L.; Illia, G. J. A. A. S.; Benyahia, S.; Sanchez, C.; Kanaev, A. V., Oriented ZnO thin films synthesis by sol-gel process for laser application. *Thin Solid Films* **2003**, 428, 257-262.
145. Verma, A.; Bakhshi, A. K.; Agnihotry, S. A., Effect of citric acid on properties of CeO<sub>2</sub> films for electrochromic windows. *Sol. Energ. Mat. Sol. C.* **2006**, 90, 1640-1655.

146. Huang, W.; Shuk, P.; Greenblatt, M., Properties of sol-gel prepared  $\text{Ce}_{1-x}\text{Sm}_x\text{O}_{2-x/2}$  solid electrolytes. *Solid State Ionics* **1997**, 100, 23-27.
147. Rane, N.; Zou, H.; Buelna, G.; Lin, J. Y. S., Sol-gel synthesis and properties of unsupported and supported mesoporous ceria membranes. *J. Membrane Sci.* **2005**, 256, 89-97.
148. Guo, H.; Qiao, Y., Preparation, structural and photoluminescent properties of  $\text{CeO}_2:\text{Eu}^{3+}$  films derived by Pechini sol-gel process. *Appl. Surf. Sci.* **2008**, 254, 1961-1965.
149. Chen, S.; Wang, S. S.; Shi, K.; Liu, Q.; Han, Z., Biaxially textured  $\text{CeO}_2$  seed layers and thin films on Ni substrates by chemical solution deposition using inorganic cerium nitrate as a precursor. *Physica C* **2005**, 419, 7-12.
150. Epifani, M.; Arbiol, J.; Andreu, T.; Morante, J. R., Synthesis of soluble and size-controlled  $\text{SnO}_2$  and  $\text{CeO}_2$  nanocrystals: application of a general concept for the low-temperature, hydrolytic synthesis of organically capped oxide nanoparticles. *Eur. J. Inorg. Chem.* **2008**, 859-862.
151. Wu, G. S.; Xie, T.; Yuan, X. Y.; Cheng, B. C.; Zhang, L. D., An improved sol-gel template synthetic route to large-scale  $\text{CeO}_2$  nanowires. *Mater. Res. Bull.* **2004**, 39, 1023-1028.
152. Chen, Y.; Liu, W., Preparation and tribological properties of sol-gel zirconia thin films stabilized with ceria. *Mater. Lett.* **2002**, 55, 407-413.
153. Murali, K. R., Characteristics of sol-gel dip coated ceria films. *J. Mater. Sci.: Mater. Electron.* **2008**, 19, 369-371.
154. Seddon, K. R.; Stark, A.; Torres, M.-J., Influence of chloride, water, and organic solvents on the physical properties of ionic liquids. *Pure Appl. Chem.* **2000**, 72, (12), 2275-2287.
155. Rivera-Rubero, S.; Baldelli, S., Influence of water on the surface of hydrophilic and hydrophobic room-temperature ionic liquids. *J. Am. Chem. Soc.* **2004**, 126, 11788-11789.
156. Welton, T., Ionic liquids in catalysis. *Coord. Chem. Rev.* **2004**, 248, 2459-2477.
157. Letaief, S.; Elbokl, T. A.; Detellier, C., Reactivity of ionic liquids with kaolinite: Melt intersalation of ethyl pyridinium chloride in an urea-kaolinite pre-intercalate. *J. Colloid Interface Sci.* **2006**, 302, 254-258.



158. Lataief, S.; Detellier, C., Nanohybrid materials from the intercalation of imidazolium ionic liquids in kaolinite. *J. Mater. Chem.* **2007**, *17*, 1476-1484.
159. Cao, G.; Brinker, C. J., *Annual Review of Nano Research*. World Scientific: 2008; Vol. 2, p 653.
160. Herring, A. M., Inorganic–polymer composite membranes for proton exchange membrane fuel cells. *J. Macromol. Sci. Polymer Rev.* **2006**, *46*, 245-296.
161. Popov, V. N.; Doren, V. E. V., Elastic properties of single-walled carbon nanotubes. *Phys. Rev. B* **2000**, *61*, (4), 3078-3084.
162. Odom, T. W.; Huang, J.-L.; Kim, P.; Lieber, C. M., Atomic structure and electronic properties of single-walled carbon nanotubes. *Nature* **1998**, *39*, 62-64.
163. Mamedov, A. A.; Kotov, N. A.; Prato, M.; Guldi, D. M.; Wicksted, J. P.; Hirsch, A., Molecular design of strong single-wall carbon nanotube/polyelectrolyte multilayer composites. *Nat. Mater.* **2002**, *1*, 190-194.
164. Lu, G. Q.; Costa, J. C. D. d.; Duke, M.; Giessler, S.; Socolow, R.; Williams, R. H.; Kreutz, T., Inorganic membranes for hydrogen production and purification: A critical review and perspective. *J. Colloid Interface Sci.* **2007**, *314*, 589-603.
165. Wu, J. C.-S.; Cheng, L.-C., An improved synthesis of ultrafiltration zirconia membranes via the sol–gel route using alkoxide precursor. *J. Membr. Sci.* **2000**, *167*, 253-261.
166. Changrong, X.; Huaqiang, C.; Hong, W.; Pinghua, Y.; Guangyao, M.; Dingkun, P., Sol-gel synthesis of yttria stabilized zirconia membranes through controlled hydrolysis of zirconium alkoxide. *J. Membr. Sci.* **1999**, *162*, 181-188.
167. Tsuru, T.; Hino, T.; Yoshioka, T.; Asaeda, M., Permporometry characterization of microporous ceramic membranes. *J. Membr. Sci.* **2001**, *186*, 257-265.
168. Tsuru, T.; Takata, Y.; Kondo, H.; Hirano, F.; Yoshioka, T.; Asaeda, M., Characterization of sol /gel derived membranes and zeolite membranes by nanoporometry. *Sep. Purif. Technol.* **2003**, *32*, 23-27.
169. Spijksma, G. I.; Huisjes, C.; benes, N. E.; Kruidhof, H.; Blank, D. H. A.; Kessler, V. G.; Bouwmeester, H. J. M., Microporous zirconia–titania composite membranes derived from diethanolamine-modified precursors. *Adv. Mater.* **2006**, *18*, 2165-2168.

170. Nair, B. N.; Burwood, R. P.; Goh, V. J.; Nakagawa, K.; Yamaguchi, T., Lithium based ceramic materials and membranes for high temperature CO<sub>2</sub> separation. *Prog. Mater. Sci.* **2009**, 54, 511-541.
171. Sata, N.; Eberman, K.; Eberl, K.; Maier, J., Mesoscopic fast ion conduction in nanometre-scale planar heterostructures. *Nature* **2000**, 408, (6815), 946-949.
172. Jin-Phillipp, N. Y.; Sata, N.; Maier, J.; Scheu, C.; Hahn, K.; Kelsch, M.; Ruhle, M., Structures of BaF<sub>2</sub>-CaF<sub>2</sub> heterolayers and their influences on ionic conductivity. *J. Chem. Phys.* **2004**, 120, (5), 2375-2381.
173. Sayle, D. C.; Doig, J. A.; Parker, S. C.; Watson, G. W., Synthesis, structure and ionic conductivity in nanopolycrystalline BaF<sub>2</sub>/CaF<sub>2</sub> heterolayers. *Chem. Commun.* **2003**, (15), 1804-1806.
174. Azad, S.; Marina, O. A.; Wang, C. M.; Saraf, L.; Shutthanandan, V.; McCready, D. E.; El-Azab, A.; Jaffe, J. E.; Engelhard, M. H.; Peden, C. H. F.; Thevuthasan, S., Nanoscale effects on ion conductance of layer-by-layer structures of gadolinia-doped ceria and zirconia. *Appl. Phys. Lett.* **2005**, 86, (13).
175. Sayle, T. X. T.; Parker, S. C.; Sayle, D. C., Ionic conductivity in nano-scale CeO<sub>2</sub>/YSZ heterolayers. *J. Mater. Chem.* **2006**, 16, (11), 1067-1081.
176. Wang, C. M.; Azad, S.; Shutthanandan, V.; McCready, D. E.; Peden, C. H. F.; Saraf, L.; Thevuthasan, S., Microstructure of ZrO<sub>2</sub>-CeO<sub>2</sub> hetero-multi-layer films grown on YSZ substrate. *Acta Materialia* **2005**, 53, (7), 1921-1929.
177. Kosacki, I.; Rouleau, C. M.; Becher, P. F.; Bentley, J.; Lowndes, D. H., Surface interface-related conductivity in nanometer thick YSZ films. *Electrochem. Solid-State Lett.* **2004**, 7, (12), A459-A461.
178. Kosacki, I.; Rouleau, C. M.; Becher, P. F.; Bentley, J.; Lowndes, D. H., Nanoscale effects on the ionic conductivity in highly textured YSZ thin films. *Solid State Ionics* **2005**, 176, (13-14), 1319-1326.
179. Huang, H.; Gur, T. M.; Saito, Y.; Prinz, F., High ionic conductivity in ultrathin nanocrystalline gadolinia-doped ceria films. *Appl. Phys. Lett.* **2006**, 89, (14).
180. Ishihara, T.; Tabuchi, J.; Ishikawa, S.; Yan, J.; Enoki, M.; Matsumoto, H., Recent progress in LaGaO<sub>3</sub> based solid electrolyte for intermediate temperature SOFCs. *Solid State Ionics* **2006**, 177, (19-25), 1949-1953.

181. Ishihara, T.; Yan, J.; Matsumoto, H., Extraordinary fast oxide ion conductivity in  $\text{La}_{1.61}\text{GeO}_5$ -delta thin film consisting of nano-size grain. *Solid State Ionics* **2006**, 177, (19-25), 1733-1736.
182. Yan, J.; Matsumoto, H.; Ishihara, T., Nanosize effect on the oxide ionic conductivity of lanthanum germanite thin films (vol 8, pg A607, 2005). *Electrochem. Solid-State Lett.* **2006**, 9, (1), L1-L1.
183. Yan, J. W.; Matsumoto, H.; Ishihara, T., Nanosize effect on the oxide ionic conductivity of lanthanum germanite thin films. *Electrochem. Solid-State Lett.* **2005**, 8, (11), A607-A610.
184. Kulkarni, A.; Bourandas, A.; Dong, J. H.; Fuierer, P. A.; Xiao, H., Synthesis and characterization of nanocrystalline  $(\text{Zr}_{0.84}\text{Y}_{0.16})\text{O}_{1.92}(\text{Ce}_{0.85}\text{Sm}_{0.15})\text{O}_{1.925}$  heterophase thin films. *J. Mater. Res.* **2006**, 21, (2), 500-504.
185. Sata, N.; Jin-Phillipp, N. Y.; Eberl, K.; Maier, J., Enhanced ionic conductivity and mesoscopic size effects in heterostructures of  $\text{BaF}_2$  and  $\text{CaF}_2$ . *Solid State Ionics* **2002**, 154-155, 497-502.
186. Lotsch, B. V.; Ozin, G. A., Clay bragg stack optical sensors. *Adv. Mater.* **2008**, 20, 4079-4084.
187. Lotsch, B. V.; Ozin, G. A., Photonic clays: a new family of functional 1D photonic crystals. *ACS NANO* **2008**, 2, (10), 2065-2074.
188. Chang, K.-C.; Chen, S.-T.; Lin, H.-F.; Lin, C.-Y.; Huang, H.-H.; Yeh, J.-M.; Yu, Y.-H., Effect of clay on the corrosion protection efficiency of PMMA/Na-MMT clay nanocomposite coatings evaluated by electrochemical measurements. *Eur. Polym. J.* **2008**, 44, 13-23.
189. Yeh, J.-M.; Liou, S.-J.; Lin, C.-Y.; Cheng, C.-Y.; Chang, Y.-W.; Lee, K.-R., Anticorrosively enhanced PMMA-clay nanocomposite materials with quaternary alkylphosphonium salt as an intercalating agent. *Chem. Mater.* **2002**, 14, 154-161.
190. Li, Q.; Zhong, X.; Hu, J.; Kang, w., Preparation and corrosion resistance studies of zirconia coating on fluorinated AZ91D magnesium alloy. *Prog. Org. Coat.* **2008**, 63, 222-227.
191. Tolstoy, V. P.; Ehrlich, A. G., C--The synthesis of  $\text{CeO}_{2+n}\text{H}_2\text{O}$  nanolayers on silicon and fused-quartz surfaces by the successive ionic layer deposition technique. *Thin Solid Films* **1997**, 307, 60-64.

192. Kern, W.; Puotinen, D. A., Cleaning solutions based on hydrogen peroxide for use in silicon semiconductor technology. *RCA Rev.* **1970**, 31, 187-206.
193. Piner, R. D.; Xu, T. T.; Fisher, F. T.; Qiao, Y.; Ruoff, R. S., Atomic force microscopy study of clay nanoplatelets and their impurities. *Langmuir* **2003**, 19, (19), 7995-8001.
194. Wang, k.; Wang, L.; Wu, J.; Chen, L.; He, C., Preparation of highly exfoliated epoxy/clay nanocomposites by "slurry compounding": process and mechanisms. *Langmuir* **2005**, 21, (8), 3613-3618.
195. Kim, D. W.; Kumar, J.; Blumstein, A., Ordered assembly of conjugated ionic polyacetylenes within clay nanoplatelets: Layer-by-layer assembly and intercalative polymerization. *Appl. Clay Sci.* **2005**, 30, 134-140.
196. Duran, J. D. G.; Ramos-Tejada, M. M.; Arroyo, F. J.; Gonzalez-Caballero, F., Rheological and electrokinetic properties of sodium montmorillonite suspensions. *J. Colloid Interface Sci.* **2000**, 229, 107-117.